

Stabilisation of late transition metal and noble metal films in hexagonal and body centred tetragonal phases by epitaxial growth

Dissertation
zur Erlangung des Grades eines Doktors
der Naturwissenschaften

vorgelegt von

Dipl.-Phys. Erwin Hüger
aus Lugosch

genehmigt von der
Gemeinsamen Fakultät für Natur- und Materialwissenschaften
der Technischen Universität Clausthal

Tag der mündlichen Prüfung
26. August 2005

Diese Arbeit wurde am Institut für Physik und Physikalischen Technologien angefertigt.

Dekan der Fakultät für Natur-
und Materialwissenschaften der
Technischen Universität Clausthal und
Vorsitzender der Prüfungskommission:

Prof. Dr. W. Schade

Berichterstatter:

Prof. Dr. W. Daum

Mitberichterstatter:

Prof. Dr. V. Kempter

Mitberichterstatter:

Prof. Dr. em. L. Fritsche

Diese Arbeit wurde von der Deutschen Forschungsgemeinschaft (DFG) und durch das Land Niedersachsen finanziell unterstützt.

Contents

Abstract	v
Acronyms	ix
1 Introduction	1
2 Experimental setup	7
2.1 The apparatus	7
2.2 The techniques	9
2.2.1 Reflection High Energy Diffraction (RHEED)	9
2.2.2 Auger Electron Spectroscopy (AES)	12
2.2.3 Photo-electron spectroscopy (XPS, ARUPS)	14
2.2.4 Auger and photo-electron diffraction (AED and XPD)	18
2.3 The W(001) and Nb(001) substrates	20
3 Film thickness determination	23
3.1 Films of Au metal	23
3.2 Films of Cu metal	27
3.3 Films of Pd, Co and Ag metal	27
4 The growth of late transition and noble metals on (001)-oriented cubic substrates.	31
4.1 Diffraction of primary electrons (RHEED,LEED)	31
4.1.1 The pseudomorphic range	31
4.1.2 Beyond the pseudomorphic range. Growth between 2 and 3 monolayers.	31
4.1.3 Centered diffraction pattern	34
4.2 Diffraction of secondary electrons (XPD)	34
5 Analysis and interpretation of the observed patterns	39
5.1 RHEED transmission	39
5.2 Analysing TED data	43
5.3 LEED/RHEED reflection	45
5.3.1 Film orientation	45
5.3.2 Explanation of the centred diffraction patterns of smooth surfaces.	47
5.4 XPD	53
5.5 UPS	54
6 Films grown in the hcp, dhcp and bct phase modification by epitaxy on (001) substrates.	57
6.1 Lattice misfit	57
6.2 Effect of the lattice misfit: Examples	59
7 Stability of the hexagonal close-packed phase modification.	67
Epitaxy in the light of the crystal phase transformation.	67
7.1 The pseudomorphic bct (001)-phase in transition to hexagonal close-packed structures.	67
7.2 Experimental data on the stability of films grown in a (11 $\bar{2}$ 0) oriented hcp phase modification	69
7.3 Sliding a close-packed atomic layer across an adjacent layer to change the stacking sequence	73
7.4 Models of changing the stacking sequence.	76

7.4.1	Transition from hcp- to the dhcp-stacking	76
7.4.2	Transition from hcp- to fcc-stacking	76
7.4.3	Transition from dhcp to fcc stacking	79
7.5	Test of the predicted energy barriers.	80
7.6	Influence of the domain-topology on the phase-transition.	85
7.6.1	Material transport in the hcp to fcc phase transition	85
7.6.2	The hcp/dhcp phase transition	86
7.6.3	The hcp($11\bar{2}0$)/fcc(001) phase transition.	86
7.7	Explanation of the occurrence and the stability of the hexagonal phase modification in films grown on (001) oriented substrates.	90
7.7.1	The occurrence of the ($11\bar{2}0$) oriented lattice.	90
7.7.2	The stability of the ($11\bar{2}0$) oriented hexagonal phase.	91
7.8	The pseudomorphic-bct/fcc-transition	95
7.9	Influence of the substrate lattice structure	95
7.10	Effect of the electronic structure of the substrate surface	95
8	Doubling the pseudomorphic-range by imposing epitaxial constraints on both interfaces of substrate supported films	97
8.1	Deposition of an additional metal	97
8.2	Suppression of ($11\bar{2}0$)-growth	97
8.3	Conversion of already formed hcp-layers into pseudomorphic-layers	98
8.3.1	The Fe/Co/Fe(001)-system	98
8.3.2	The Cu/Co/Fe(001)-system	98
8.3.3	The Alumina/Co/Fe(001)-system	99
8.4	Phase stability diagrams	100
9	Conclusion	101
	References	105

Abstract

This work is concerned with the hetero-epitaxial growth of metallic films whose crystal structure differs from their bulk equilibrium structure. Apart from finding techniques of producing these films on metal substrates and uniquely identifying their structure, a large portion of the studies is focused on understanding the initiation, growth and stability of these non-equilibrium structures.

Pseudomorphic growth within the first few monolayers (MLs) of a deposited film represents a common phenomenon of metal on metal epitaxy. It can lead to the growth of ultrathin films that display body-centred (bct) or even face-centred tetragonal (fct) structure. However, after the initial pseudomorphic-growth the films turn typically to the formation of their natural phase. Surprisingly, there exist cases where the films develop beyond the pseudomorphic-growth a crystal phase different from their natural structure. The present work analyzes in detail this peculiar non-equilibrium growth, in addition to the general phenomenon of pseudomorphic-growth. In particular it will be shown that metals whose natural phase is face centred cubic (fcc) can grow in body centred tetragonal (bct) phase by pseudomorphy in the form of thin films on (001)-oriented surfaces of suitable cubic substrates. Beyond the thickness-range of pseudomorphic growth and for certain adsorbate/substrate combinations the films develop a hexagonal close-packed (hcp) structure rather than forming their natural fcc-lattice.

The appearance of centred patterns in LEED and RHEED after pseudomorphic-growth constitutes a common feature of many fcc metals deposited on (001)-surfaces of cubic substrates. This just reflects the presence of a hexagonal phase as we shall explain in detail.

The insight that pseudomorphy can provide a route to non-equilibrium structures is well established. If the film-substrate bonding is strong enough the film is forced to grow pseudomorphically beyond the first monolayer, provided that the array and spacings of atoms in the substrate surface differ sizably from the respective natural properties of the adjacent atomic plane of the adsorbate. Conversely, if the atomic arrays in the planes of contact are similar, as in the case of fcc-Au deposited on a W(110) surface, for example, where the (111)-plane of Au closely resembles the W(110)-surface plane, one observes a transition into the unperturbed fcc(111)- structure of Au already within the first monolayer. This contrasts with the situation when Au is deposited on a W(100)-surface where the atomic packing density is considerably less than that of an fcc(100)-plane of the Au adsorbate. In that case of pivotal pseudomorphic growth conditions the induced body centered tetragonal pseudomorphic Au-structure persists up to 10 monolayers.

An important result of our studies consists in the observation that the tetragonal ratio c/a of the pseudomorphic-film (a for the square base and c for the height of the two-atom bct cell) determines which phase of the film develops after the pseudomorphic-growth. For tetragonal-ratios $c/a < 1$ a (11 $\bar{2}$ 0) oriented hcp phase appears immediately after 2 pseudomorphic MLs, whereas for $c/a > 1$ the pseudomorphic phase persists in the film up to a thickness of 10 MLs, merging afterwards in the equilibrium (001) oriented fcc-structure.

This behaviour is, of course, governed by the energy balance in forming the respective lattices. For $c/a=1$ one is dealing with the undistorted bcc-lattice where the interatomic distance is larger than in the equilibrium fcc-lattice of the same lattice parameter. The total energy per atom is correspondingly larger than that of an atom in the fcc-lattice. As has been pointed out by Bain 80 years ago it is possible to smoothly transform a bcc-structure into an fcc-structure by a tetragonal distortion. When c/a increases beyond 1, one gains successively energy along this so-called Bain-path until an energy minimum is reached at $c/a=\sqrt{2}$ associated with the fcc-structure. When c/a decreases below 1 one also gains energy as follows from ab initio calculations. This lowering of the total energy per atom has to be expected because the atomic array in the bct(110)-planes resembles that of the close-packed planes in an hcp-lattice, i. e. they display closest packing in the pseudomorphic-lattice. Hence, they gain interaction energy at shortening their distance. If one allows below $c/a=0.82$, besides the tetrag-

onal distortion, for an additional degree of freedom that consists in a small displacement of every second close-packed atomic plane the energy gain further increases until one has reached the minimum at the hcp-structure. Thus, $c/a=1$ marks a maximum along possible transition paths, a kind of a “watershed”. If the (001)-substrate surface forces a tetragonal ratio $c/a>1$ on the first two adlayers (at constant specific volume of the adsorbate), it would therefore require an additional energy per atom to overcome this maximum in the direction of forming a hcp-structure. The total amount of this additional energy would increase layer by layer as the film thickens. For that reason the film chooses to transform along the path toward the fcc-minimum. But because of the large misfit of the fcc-lattice with respect to the (001)-substrate surface, connected with the much higher packing density in the fcc(001)-plane, the adlayers maintain their bct-structure whose higher energy is outweighed by the gain in adsorbate/substrate interaction energy. The latter constitutes a fixed quantity, as opposed to the adsorbate bct-distortion energy which increases layer by layer. At a certain thickness the two energies of opposite sign cancel. The film can now start growing in its natural fcc-structure. It should be noticed that the changeover to the fcc-structure along the Bain-path is purely displacive, that means it does not require atomic motion across interstitial positions and therefore conserves the initial domain topology of the film.

If the substrate imposes a ratio $c/a<1$ on the first two adlayers the energy balance favours the formation of hcp-growth. In analogy to the previous case a pseudomorphic-film associated with a tetragonal ratio of $c/a<1$ would need additional energy to overcome the bcc-maximum along the transformation path toward the fcc-structure. The pseudomorphic-growth develops a set of close-packed hexagonal planes which stay perpendicular to the surface. That means, the stacking axis lies in the (001)-surface of the substrate and is locked by it. This set of close-packed hexagonal planes starts forming immediately when the conditions for a rearrangement of already deposited atoms are given, viz. at the formation of the third ML. Its in-plane structure (parallel to the surface) is still controlled by pseudomorphy and therefore favours a relaxation through mutual shifts of close-packed planes into the positions of the close-packed structure, thereby conserving the density of the atomic planes parallel to the surface.

The pseudomorphic bct(001) phase orders its close-packed bc(110) planes in an ABAB... stacking mode which is identical to that of the hcp-phase. Hence, as the relaxation of the pseudomorphic-film into the $(11\bar{2}0)$ oriented hcp-structure proceeds, the stacking mode remains unaffected. As already mentioned above, the transition is achieved by merely shifting every second close-packed bct(110) plane over only $1/6$ of the interatomic distance in the $[1\bar{1}0]$ direction. In actual fact this sliding will not happen as a cooperative process involving all atoms of a plane simultaneously, but rather by largely uncorrelated small displacements of the individual atoms of that plane. Along the path of a displacive transition thus described the total energy decreases continuously. The non-occurrence of an energy barrier in shifting the close-packed planes is, of course, connected with the absence of a change in the stacking mode. Such a change is inevitably accompanied by a considerable intermediate atomic overlap, and would hence cause an energy barrier to occur.

For $c/a<1$ one has to overcome an energy maximum in performing a displacive phase transition from the pseudomorphic bct(001) phase to the fcc-structure. It can be traced back to a change of the stacking mode effecting such an energy barrier to show up in the transformation path. But there are actually two kinds of transition paths where intermediate atomic overlaps are either small or large. The path associated with a large atomic overlap displays correspondingly an enormous energy barrier, larger than the film desorption energy. Thus, this path can be excluded for physical reasons. The alternative path is connected with low atomic overlap, and hence the associated energy barrier is so low that it can be overcome at room-temperature. However, closer inspection reveals that the restructuring of the film along this path requires a shift of close-packed planes over large distances involving a reshuffling of atoms in the film-substrate interface, a process that is strongly inhibited. This remains to be true even for films that are stripped off their substrates. The non-occurrence of atomic motion over more the fractions of inter-atomic distances is shown to be a consequence of domain formation

on top of the substrate during the epitaxial growth of the metal adsorbate. It leads to a pattern of evenly shaped mutually orthogonal rectangular patches whose geometry is dictated by the four-fold symmetry of the substrate surface. Their occurrence is evidenced by various experiments. These domains define a particular topology that excludes certain possibilities of reordering atoms. Changes of the film structure can only take place along transition paths that conserve this orthogonal domain pattern. Consequently, the only physically admissible possibility to relax the pseudomorphic-film into a close-packed structure consists in ordering close-packed planes in a non-fcc stacking sequence (hcp or dhcp).

When at large film thicknesses (e.g. more than 100 MLs) the hcp-film finally merges in the fcc-structure, this transition is not initiated by a gradual changeover to fcc-stacking, which, as mentioned previously, destroys the domain topology of the film, but rather by inducing a tetragonal deformation of the lattice which conforms to requirement of topology conservation. In a first step the $(11\bar{2}0)$ oriented hcp-film undergoes a minute shift of every second close-packed plane ending up in the (001) oriented bct symmetry. This is followed then by a sizable tetragonal deformation of the (001) oriented bct structure that finally leads to the atomic array of a (001) oriented fcc film. Such a transition conserves the orthogonal pattern of rectangular domains that defines the primary topology of the film.

The displacive transition from hcp- to dhp-order presents another structural change where the domain topology stays unaffected. It is also associated with a low energy barrier that can be overcome by annealing the films at moderate temperatures or even only at room temperature. The double-hcp stacking is found in film metals with a high stacking fault energy like Rh and Pd. However, either stacking sequence can occur with the same metal depending on the strength of the bond to the substrate. For example, $(11\bar{2}0)$ oriented hcp Ni grows on Fe(001), whereas if the bond between Ni and substrate is weaker, e.g. for Ni on Au(001), one observes the $(11\bar{2}0)$ oriented dhcp-structure in Ni.

Apart from discussing the epitaxial growth behaviour of uncovered metal films and their phase stability, a large portion of the present work is devoted to the techniques of film preparation and characterization of their structure: electron diffraction and photoelectron spectroscopy. We compile and critically review the entire material concerning epitaxial films of $(11\bar{2}0)$ hexagonal or pseudomorphic (001) bct structure obtained from our studies and by other authors within our concept of non-equilibrium growth of metal films.

ACRONYMS

AED	Auger electron diffraction
AES	Auger electron spectroscopy
ARUPS	angle resolved ultraviolet photoelectron spectroscopy
bcc	body centred cubic
bct	body centred tetragonal
BZ	Brillouin zone
DOS	density of states
DFT	density functional theory
dhcp	double hexagonal close packed
EAM	embedded-atom method
e.g.	example given
ESCA	electron spectroscopy for chemical analysis
EXAFS	extended X-ray-absorption fine structure
FEM	field ion microscopy
fcc	face centred cubic
ftc	face centred tetragonal
GGA	generalized gradient correction
hcp	hexagonal close packed
HREM	high resolution electron microscopy
i.e.	in explanation
LAPW	linear augmented plane-wave method
LEED	low energy electron diffraction
LEED-IV	LEED-spot-intensity (I) versus LEED primary beam acceleration voltage (V)
LEEM	low energy electron microscopy
LSDA	local spin density approximation
MBE	molecular beam epitaxy
ML	monolayer
NMR	nuclear magnetic resonance
nn	nearest neighbor
PDMEEM	primary-beam diffraction modulated electron emission
PES	photo-electron spectroscopy
RHEED	reflection high energy electron diffraction
REM	reflection electron microscopy
STM	scanning tunneling microscopy
TED	transmission electron diffraction
TEM	transmission electron microscopy
UHV	ultra-high vacuum
QSE	quantum size effect
QWS	quantum well states
UPS	ultraviolet photoelectron spectroscopy
XANES	X-ray absorption near-edge structure
XPS	X-ray photoelectron spectroscopy
XPD	X-ray photoelectron diffraction
XRD	X-ray diffraction

1 Introduction

A common feature of epitaxial growth of metals on substrate metals is that in many cases pseudomorphic growth occurs during the first monolayers before the film converts into its generic crystal structure. In the case of strong adsorbate-substrate bonding, there are many film/substrate combinations for which epitaxial strain is large enough to induce growth into a non-equilibrium structure. This is due to the fact that the structural modifications of many metals differ only little in total energy so that the additional strain energy induced by the misfit can tilt the energy balance to a non-equilibrium structure. Examples are the bct and fct structures [1, 2, 3, 4, 5, 6, 7, 8] in various systems but a more dramatic one is the formation of a hcp layer after the initial pseudomorphic growth [9, 10, 11, 12, 13, 14, 15, 16, 17, 18, 19, 20, 21, 22].

The objective of this work is to investigate the conditions under which substrates fcc metals can be grown in hexagonal close packed (hcp or double-hcp (dhcp)) or body centred cubic (bcc) phase modifications. The bcc lattice (fig.1.1a,b,c) is four-fold symmetric with respect to three orthogonal axes, but it does not contain close-packed atomic planes. By contrast, the fcc-lattice (fig.1.1d,e,f) is conspicuous by the exceptional property of containing close-packed atomic planes and yet displaying four-fold symmetry around analogous axes. To illustrate the occasionally dramatic effect of a non-

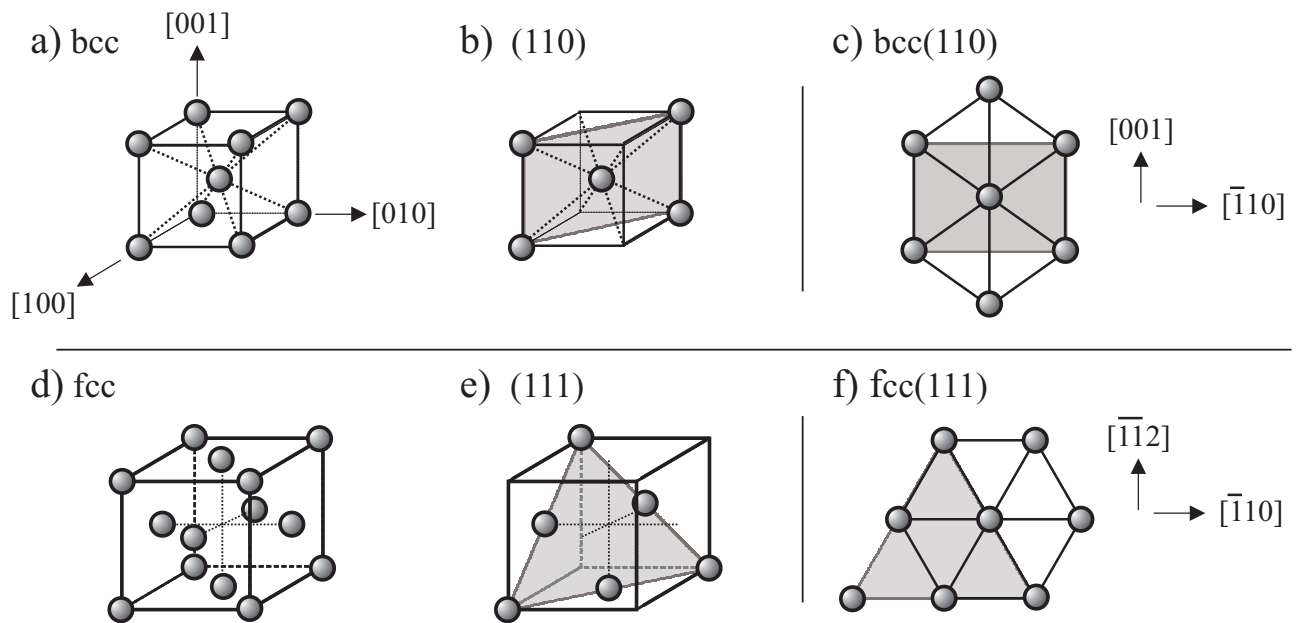


Figure 1.1: The cubic unit cell of the bcc-lattice (shown in panel (a)) contains two atoms as distinct from the fcc-lattice where the unit cell contains four atoms. At constant atomic density the cubic unit cell of the bcc-lattice is therefore by a factor of two smaller than that of the fcc-lattice. Of all the atomic planes of the bcc-lattice the rectangularcentered (110)-planes possess the largest packing density, different from the fcc-lattice where close-packing occurs in the (111)-planes (panel (e,f)) which are closely stacked along the $\langle 111 \rangle$ -direction in an ABCABC...fashion.

equilibrium crystal structure on the electronic properties of the material we briefly discuss the case of some transition metals.

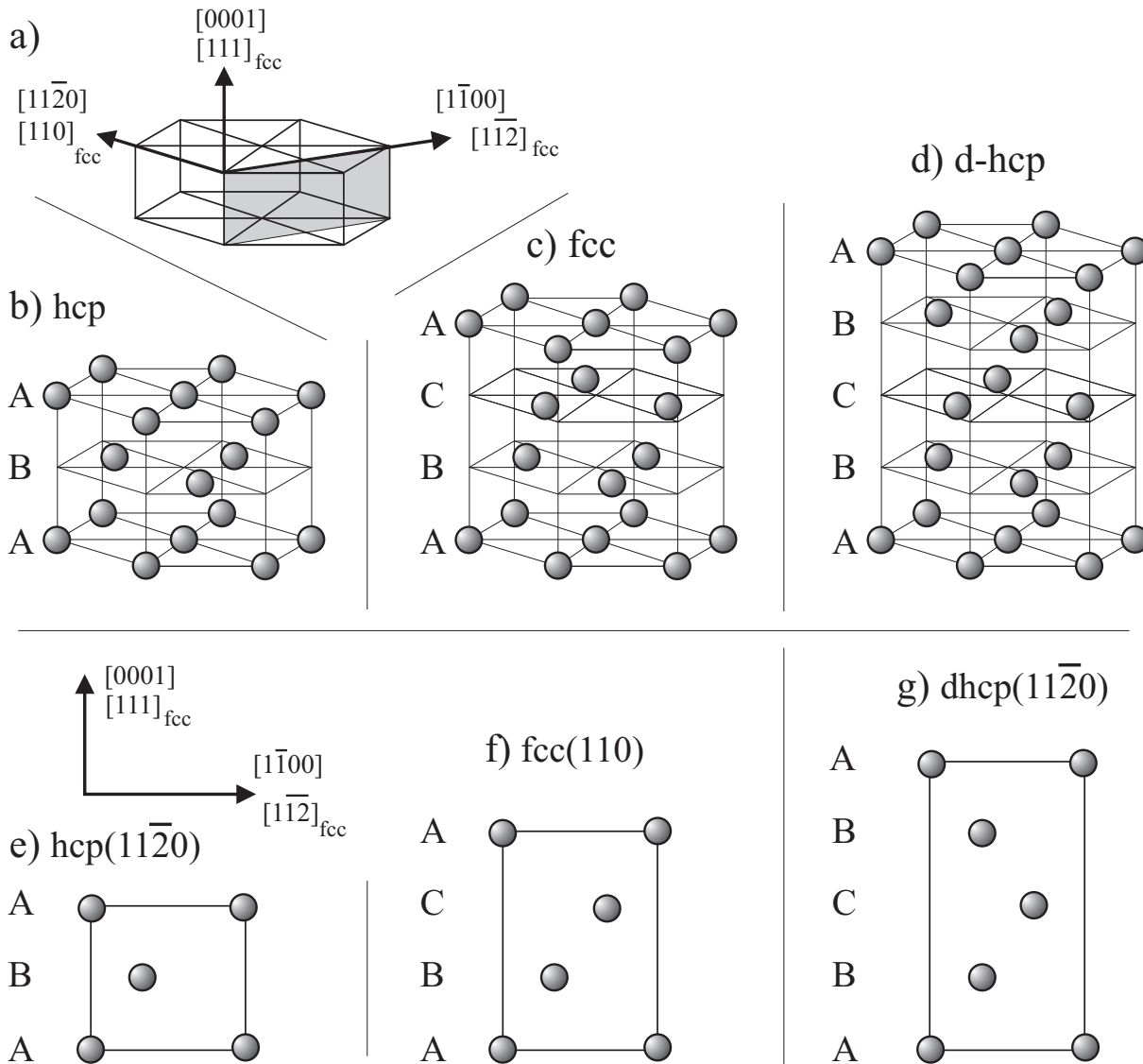


Figure 1.2: Close-packed metals consist of close-packed hexagonal atomic planes. They are stacked according to the following rules: the atoms of a plane lie on-top of centers of triangles formed by three equidistant atoms (on 'hollow' sites) of the two adjacent close-packed planes. If the stacking periodicity is two (panels (b,e)), three (c,f) or four (d,g) close-packed planes, then the hcp, fcc and double-hcp lattice, respectively, is formed. Only the stacking periodicity of three hexagons build up a lattice with four-fold-symmetry. A plane which contains the stacking axis is the $(11\bar{2}0)$ atomic plane (e,f,g).

a) Hexagonal lattice. The $[0001]$ ($[111]_{fcc}$), $[11\bar{1}00]$ ($[11\bar{2}]_{fcc}$) and $[11\bar{2}0]$ ($[110]_{fcc}$) directions are orthogonal to each other. The $[11\bar{1}00]$ ($[11\bar{2}]_{fcc}$) and $[11\bar{2}0]$ ($[110]_{fcc}$) directions lie within the close-packed hexagonal layers. The $(11\bar{2}0)$ ($(110)_{fcc}$) plane is marked in grey. b,c,d) The hcp- (ABAB...) (b), fcc- (ABCABC...) (c), and dhcp- (ABCBA...) (d) stacking of close-packed hexagonal planes. These are the only possible ways to stack the planes with a stacking periodicity of two (hcp), three (fcc) and four (dhcp) close-packed hexagonal planes. e,f,g) The $(11\bar{2}0)$ ($(110)_{fcc}$) planes for a hcp- (e), fcc- (f) and dhcp-stacking (g).

The physical properties of bulk transition metals are well explored and known. A particularly well studied property that reflects peculiarities of the electronic structure, consists in the ferromagnetic order of the elemental 3d metals Fe, Co and Ni. Cr metal is known to order antiferromagnetically [23, 24] and Mn metal displays a kind of non-collinear order of its spin moments [25, 26]. The other 3d metals display a spin symmetric electronic structure. The growth of metastable phases opens the possibility to induce various new physical properties of a metal which do not exist in its natural crystal phase. For example, Fe in the hexagonal close packed phase [27] and Ni in the body centered cubic phase [28] are not ferromagnetically ordered at their equilibrium lattice constants.

By contrast, late 4d transition metals which do not exhibit spin order in their natural fcc crystal structure, are ferromagnetically ordered in the bulk at the optimum lattice constant of a crystal phase different from the natural one, as predicted by self consistent ab-initio calculations [29]. Results are given below. Panel (a) of Fig.1.3 gives the total energy of Pd in the bcc, fcc, hcp and dhcp crystal

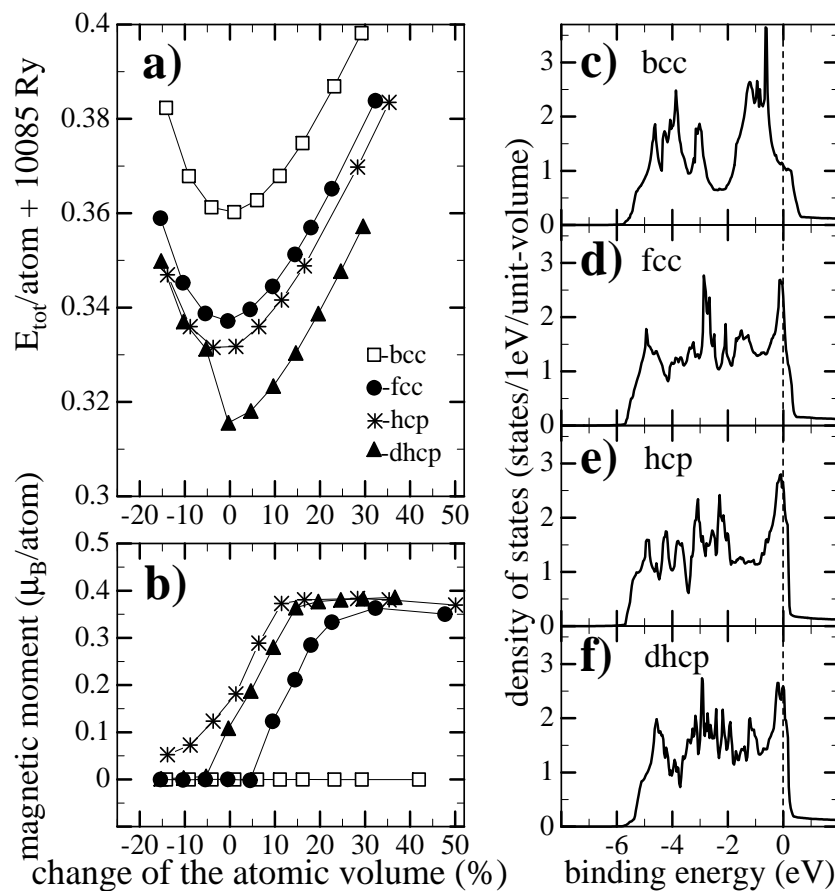


Figure 1.3: a,b) The total energy (a) and magnetic moment (b) of bulk Pd in the bcc (squares), fcc (circles), hcp (stars) and dhcp (triangles) structure as a function of atomic volume expansion (+) or contraction (-) obtained from DFT spin-polarised calculations with spin-orbit coupling included. c,d,e,f) d-projected DOS of bulk Pd in the bcc (c), fcc (d), hcp (e) and dhcp structure (f) at the equilibrium lattice constant obtained from DFT non-spin-polarised calculations with spin-orbit coupling included ([13]).

structures as a function of the lattice constant. The optimum atomic densities for which the total energies attain minima, are the same for all four crystal structures. The value for fcc Pd corresponds to a nearest neighbour distance of 2.727\AA which is by 1% smaller than the experimental one (2.75\AA). Because of their different symmetries and since the nearest and next-nearest neighbour distance are different in the bcc- and fcc-structures, the total energy of bcc Pd is much higher than that of its

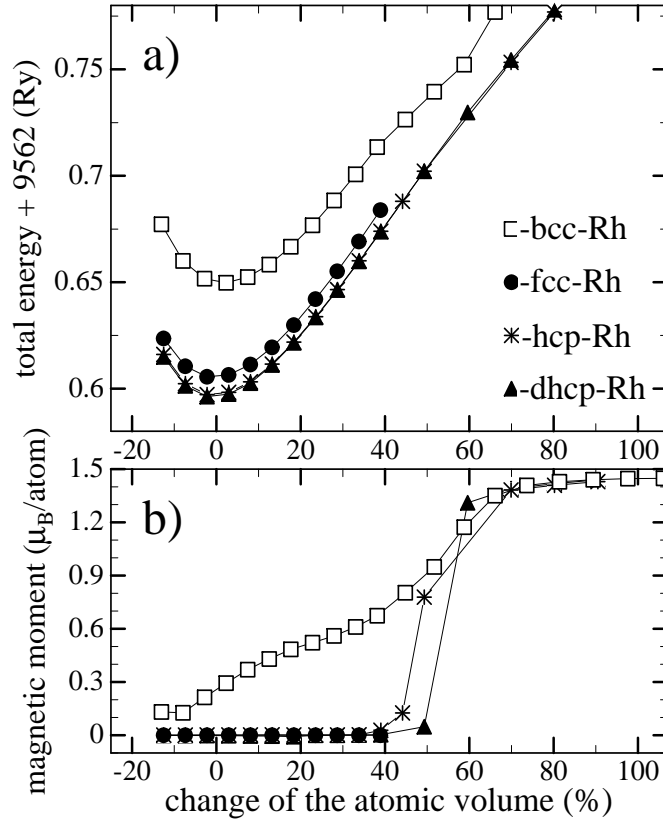


Figure 1.4: a,b) The total energy (a) and magnetic moment (b) of bulk Rh in the bcc (squares), fcc (circles), hcp (stars) and dhcp (triangles) structure as a function of atomic volume expansion (+) or contraction (-) obtained from DFT spin-polarised calculations with spin-orbit coupling included. Note, that the total energy of dhcp Rh does not drop like that of dhcp Pd (Fig.1.3a) at the equilibrium lattice constant, because dhcp Rh is not ferromagnetically ordered there ([21]).

natural fcc structure. On the other hand, the total energies of hcp and dhcp Pd are slightly smaller than that of fcc Pd. It should be stressed that this result is valid only at 0° K and does not mean that hcp and dhcp Pd are energetically more favourable than fcc Pd also at finite temperatures. Similarly, first principles non-spin-polarised calculations carried out for Ag show that, at 0° K, hcp Ag is also energetically more favourable than fcc Ag [33]. It should also be noticed that the hexagonal close-packed structures of Pd (hcp,dhcp) have the same atomic nearest and next-nearest neighbour distance as its fcc structure. Since these lattices differ only in the stacking sequence of the most densely-packed hexagonal atomic monolayers, they are energetically nearly equivalent. The total energy of dhcp Pd drops markedly at the onset of ferromagnetic order (Fig.1.3a), which occurs at the equilibrium lattice constant.

Fig.1.3b shows the calculated magnetic moments as a function of the lattice constant. In the fcc structure a magnetic moment occurs only at the lattice expansion of 10 %, saturating at 32% expansion where it attains the value of $0.36\mu_B$. The magnetic moment in hcp and dhcp Pd reaches the same saturation value, but at a smaller lattice expansion. Fig.1.3b shows that the dependence of the magnetic moment on the lattice constant of dhcp and hcp Pd is shifted toward smaller lattice expansion. As a result, a residual magnetic moment of $0.11\mu_B$ for dhcp Pd and of $0.16\mu_B$ for hcp Pd remains at the respective equilibrium lattice constant [34, 13].

The spin-order behavior of Pd can be understood in terms of the Stoner-criterion which requires for ferromagnetic order to occur the product of the density of states at the Fermi-level $N(E_F)$ and the

Stoner parameter I to be larger than unity:

$$I \cdot N(E_F) > 1 \quad . \quad (1.1)$$

The Stoner-parameter I describes the response of the exchange-correlation potentials of the two spin-subsystems to an infinitesimal, respectively increase and decrease of the associated spin densities. If one changes only the array of neighboring atoms around a Pd probe atom, I remains essentially unaffected. One is therefore justified in discussing the tendency of building up spin-order by solely comparing the various densities of state commonly abbreviated into DOS. As follows from inspection of the calculated DOS's in Fig.1.3 (c-f), the DOS of bcc-Pd is by far smaller than those of the other lattices of Pd that have been studied. Moreover, it cannot sizably be enlarged by extending the lattice which is reflected in the absence of magnetic order for negative changes of the atomic volume in Fig.1.3 b which also shows results of first-principles density functional calculations. Although the DOS of fcc-Pd at its equilibrium lattice constant is by a factor of two larger, that increase is not sufficient to fulfill the Stoner-criterion, again reflected in the absence of ferromagnetic order in Fig.1.3 b. However, in the case of hcp- and dhcp-Pd the DOS is obviously large enough so that spin-order occurs that gives rise to a magnetic moment of approximately 0.15 Bohr magnetons per atom at the associated equilibrium lattice constants.

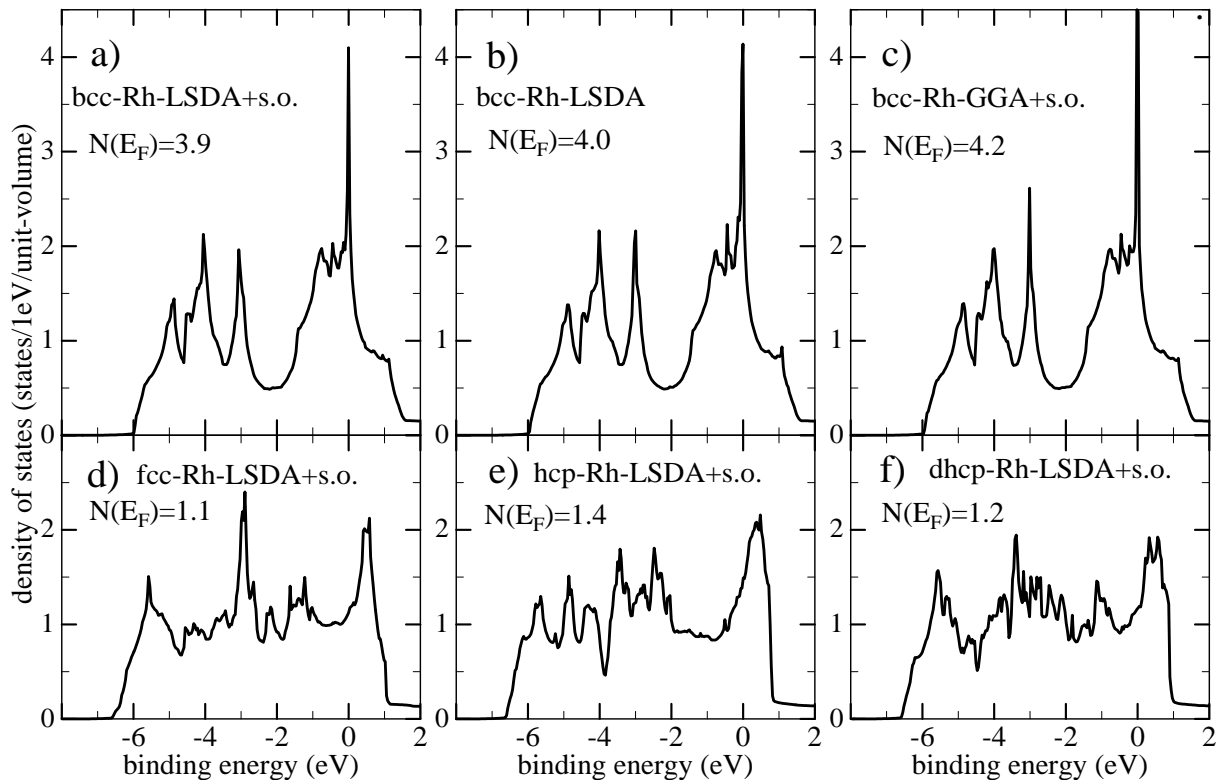


Figure 1.5: d-projected DOS of bulk Rh in the bcc (a,b,c), fcc (d), hcp (e) and dhcp structure (f) at the equilibrium lattice constant obtained from DFT non-spin-polarised calculations. The DOS presented in panels (a,b,d,e,f) were obtained in the LSDA approximation with (a,d,e,f) and without (b) spin-orbit coupling included. Panel (c) presents a GGA result ([21]).

The dependence of the total energy on the lattice constant for the crystal phases of Rh (Fig.1.4a) is similar to that of Pd (Fig.1.3a). However, the behaviour of the magnetic moment of Rh in these

crystal phases (Fig.1.4b) is completely reversed in comparison to that of Pd (Fig.1.3b): bcc Rh is ferromagnetically ordered at the equilibrium lattice constant whereas fcc, hcp and dhcp Rh is not ferromagnetic even at a lattice expansion of up to 40% [21]. The striking difference in the behavior of Rh metal is connected with the different position of its Fermi-energy ε_F in the density of states (DOS). Figure 1.5 shows that the change of symmetry from close-packed (i.e. fcc, hcp, dhcp) to body centred cubic places the Fermi-level of Rh within the strong peak of the bcc DOS. This peak appears due to a flat band which in the case of Rh lies around the Fermi-energy [21]. We could clearly attribute the flatness of this band to the symmetry of the bcc-phase [22]. As a consequence, ferromagnetism in bulk Rh is induced even in a compressed lattice [21, 22].

The present work shows, that metals whose natural phase is fcc, can be grown in bcc or hcp phases as thin films deposited on (001) surfaces of suitable cubic substrates. The thesis is organised as follows: In Section 2 the experimental methods and preparation techniques are described. Section 3 is devoted to the determination of film thicknesses. Section 4 presents details on the growth of late transition metals on (001) surfaces monitored with the aid of electron diffraction. Section 5 is concerned with analyzing the diffraction patterns. It is found that the centred patterns of many films deposited on (001) oriented substrates originate from the $(11\bar{2}0)$ oriented hexagonal phase. Section 6 reviews all epitaxial systems whose diffraction pattern can be explained by the the $(11\bar{2}0)$ oriented hexagonal or pseudomorphic (001) oriented bct phase. In Section 7 an attempt is made to explain and predict the growth of films in hcp, dhcp, and bcc phase modifications, employing elastic and a geometric misfit criteria. Using these considerations, the energy barriers in the competing phase transition paths will be predicted and compared with those calculated from DFT first-principle calculations. The experimental findings will be explained by the effect of the substrate and of the film domain topology on the energy barriers of the discussed phase transformation paths. Section 8 explains ways to enlarge the thickness range of the pseudomorphic phase. The insights gained by the present work are summarized in Section 9.

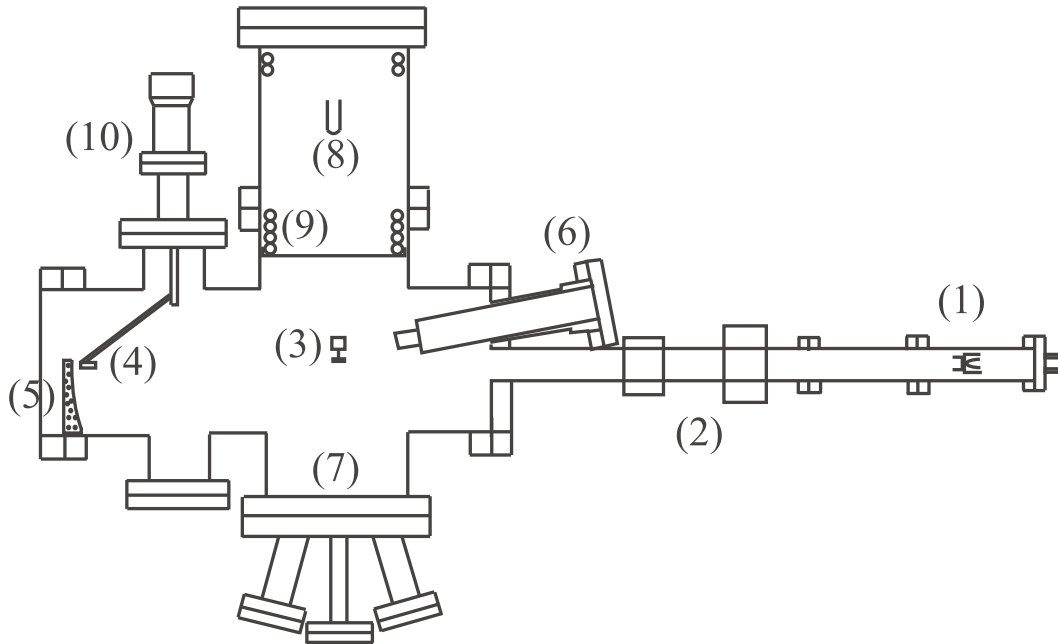


Figure 2.6: Vertical section through the RHEED-chamber. (1) RHEED gun. (2) magnetic deflection and focusing systems. (3) sample. (4) Faraday-cup. (5) RHEED-screen. (6) quadrupole mass spectrometer. (7) water cooled ovens for molecular beam epitaxy. (8) titan-sublimation pump. (9) LN₂ cooling systems (Cu-tubes). (10) adjustment system for the Faraday-cup.

2 Experimental setup

The films were grown by evaporating the constituent atoms from metallic ovens onto a substrate surface in ultra high vacuum. This procedure is known as 'molecular beam epitaxy' (MBE). Ultra high vacuum conditions are indispensable to ensure the absence of substrate contamination and contamination of the growing film. To fully characterise the films the following properties were analyzed: (i) crystal structure and surface orientation; (ii) morphology (shape) and (iii) electronic structure. As for (i) diffraction of primary and secondary electrons proved to be the most valuable tool, whereas in the case of (iii) photoelectron spectroscopy was the method of choice.

2.1 The apparatus

The experiments were performed in a VG-ESCA-LAB MKII spectrometer [35] (ESCA = Electron Spectroscopy for Chemical Analysis) which was connected to a chamber equipped with reflection high-energy electron diffraction (RHEED). A vertical section through the RHEED-chamber is shown in fig.2.6. RHEED was not only used to determine substrate and adlayer structure, orientation, and morphology but also to monitor the growth rate via specular beam intensity oscillations. RHEED patterns were obtained by a home-build ([36, 37]) magnetically focused high resolution RHEED gun (sketched in fig.2.6 at the position marked by (1)). The RHEED gun was equipped with several deflection systems (2) for beam alignment and polar angle of incidence control. The 20keV beam with an emission current of $9\mu\text{A}$ was used at grazing angles of incidence $\sim 0.3^\circ$ on the sample (marked with (3) in fig.2.6) which makes RHEED very sensitive to the surface morphology. A Faraday cup detector (marked by (4) in fig.2.6) was employed to measure the intensity of the specularly reflected electron beam. The Faraday cup could be moved to any desired position in the central part of the RHEED pattern which was simultaneously observed on the fluorescent screen (marked by (5)). A quadrupole mass spectrometer placed in position (6) (fig.2.6) served as an analyser of

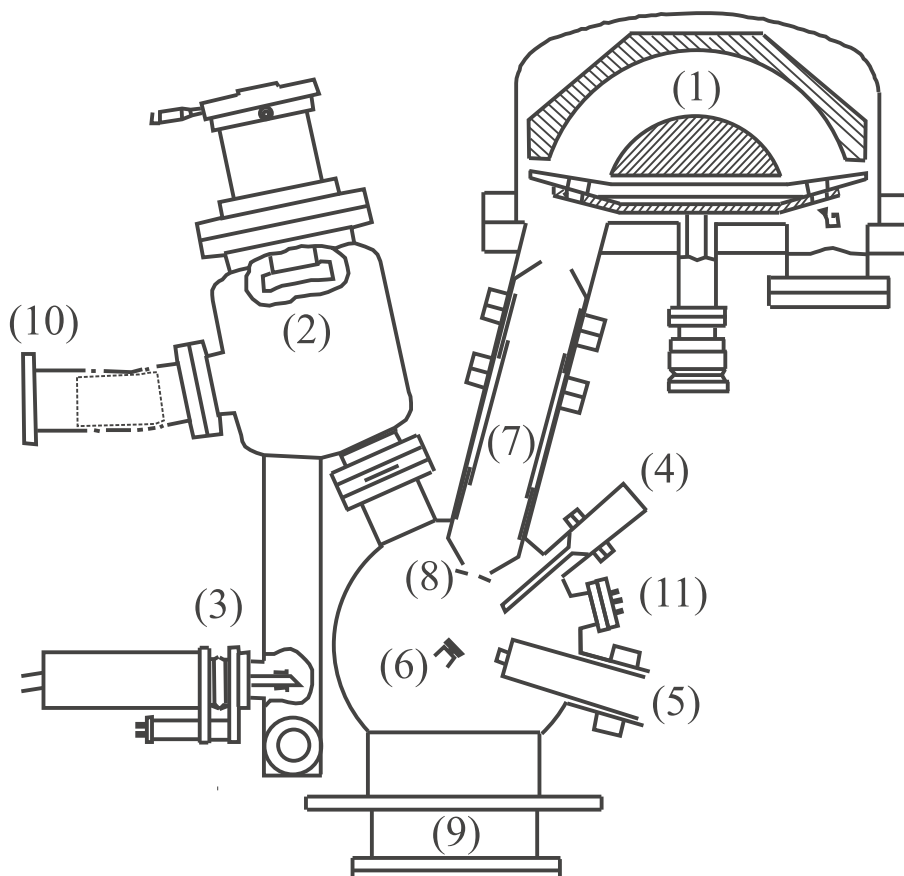


Figure 2.7: Vertical section through the ESCA-chamber. (1) hemispherical analyzer. (2) X-ray monochromator. (3) AlK_α X-ray source. (4) Leybold capillary noble-gas resonance discharge lamp. (5) VG-Microtech EX05 ion source. (6) sample. (7) electrostatic lens. (8) inlet slits (aperture). (9) Ti-sublimation pump. (10) ion-pump.

the gas composition and the stability of the evaporators (marked by (7) in fig.2.6). The home-build water-cooled metal evaporators allowed deposition rates of 0.03 – 10 monolayers (ML) per minute. The RHEED-chamber was pumped by a titanium sublimation pump (marked by (8) in fig.2.6) with a liquid nitrogen (LN_2) cooled wall (marked by (9)) and via the main (ESCA) system by a LN_2 -baffled diffusion pump which produces a base pressure of 3×10^{-11} mbar after bakeout at $\sim 500\text{K}$ for 24 hours. The pressure rose to 7×10^{-11} mbar during the metal deposition from the pre-outgassed evaporators situated in both chambers. The adsorbates were deposited by thermal desorption from high-purity metal pieces ($\geq 99.999\%$) accommodated in well shielded ovens. Metals of Co, Cu, Pd, Ag, and Au were evaporated from BeO crucibles, resistively heated by tungsten coils. By contrast, Rh metal was vaporized from a thin Rh-foil heated by electron bombardment.

The main (ESCA) chamber (fig.2.7) contained a hemispherical analyser (marked by (1) in fig.2.7) with 60meV resolution at a pass energy of 2eV, a monochromatised (marked (2)) AlK_α (1486.6eV) X-ray source (3), an electron gun (whose position is perpendicular to the vertical cut of fig.2.7) for Auger electron spectroscopy (AES). This electron gun operated at an emission current of 1 – $3\mu\text{A}$ and a beam energy of 1.8keV with a beam diameter of 0.2-1 mm at the sample. The Auger signal was differentiated by modulating the target potential with a 3 V peak-to-peak amplitude for the detection of impurities (like the oxygen O-KLL Auger transition (510eV)) and with a 1 V peak-to-peak amplitude for *in situ* monitoring of the film growth. For ultraviolet photo-electron spectroscopy (UPS) measurements a Leybold capillary noble-gas discharge lamp (marked by (4) in fig.2.7) with

an optional polariser has been used. The energy of the photon used was 21.22eV (HeI) and 16.85eV (NeI). For ARUPS measurements up to temperatures of 600K the sample was heated by thermal radiation from resistively heated W filaments below the sample holder. A chopper ensured periodic heating with a period of 60ms of which 20ms were off in order to eliminate magnetic fields during the measurement. The W-Re thermocouple spotwelded to the edge of the sample was used for temperature stabilization via filament current control. Thereby an accuracy of the temperature of about $\pm 20\text{K}$ could be achieved. UPS data were collected continuously during the overlayer (film) deposition at very low deposition rates of about 2 monolayer per hour. This allows one to determine the complete energy and coverage dependence of the photoemission features during deposition. For a higher coverage resolution of certain ARUPS features the intensities at several fixed energies were measured quasi-simultaneously during the overlayer deposition by switching the analyser energy typically every 2s between up to 5 different interesting energies. For AES and XPS (X-ray photoelectron spectroscopy) the angular acceptance of the analyzer was set to $\pm 12^\circ$, for XPD (X-ray photoelectron diffraction) and angle resolved UPS (ARUPS) to $\pm 1^\circ$. A VG-Microtech EX05 ion source (marked by (5) in fig.2.7) whose beam could be deflected, rastered and focused on the sample, served as a sputtering device. The ion optical column for focusing the beam onto the sample consists of two lenses, followed by two pairs of plates for beam scanning. The sample (marked with (6) in fig.2.7) was mounted on a home-build exchangeable specimen cartridge which was inserted into a manipulator with translation and rotational degrees of freedom. Heating by electron bombardment made it possible to reach temperatures as high as the melting point of the sample, cooling with liquid nitrogen temperatures as low as 150K were possible. The temperature was measured by a W-3%Re/W-25%Re thermocouple which was calibrated at high temperatures by a disappearing filament pyrometer. The sample could be transferred between the two subsystems within 8 minutes, what ensured a relatively save correlation between the deposition rates determined by RHEED and by electron spectroscopy, respectively.

2.2 The techniques

The surface quality and the growth mode was examined by RHEED, AES and ARUPS. The geometric structure was determined by RHEED and XPD, the electronic structure by AES, XPS and ARUPS. AES also proved to be the main tool in checking the chemical composition of the sample.

2.2.1 Reflection High Energy Diffraction (RHEED)

RHEED [39, 40, 41, 42] is, beside LEED [43, 44], the standard technique to study the structure of surfaces and thin films. This technique is based on the wave nature of the electron and its strong interaction with matter. RHEED makes use of electrons which have been accelerated to 10–100keV. The geometry of a RHEED experiment is shown in fig.2.8. The high energy electrons are directed onto the surface of a single crystal under grazing incidence. Due to the small angle of incidence (less than 1°), the penetration depth of the electrons is just a few Å. In contrast, for normal incidence, electrons with an energy of $\sim 25\text{keV}$ are expected to penetrate $\sim 200\text{Å}$ into the sample. Of course, the penetration depth is also material dependent. At grazing incidence the electron beam is diffracted at the surface, either directly on the top surface or close to the surface region of the crystal. At a fluorescent screen the kinetic energy of the electrons is partially transformed into light, and a diffraction pattern in form of light spots or streaks forming arcs (Laue-circles) is visible on the screen, if the surface are atomically flat (see figs.2.8b,2.9a). However, if the surface is covered with small three dimensional islands the electron beam will penetrate these protrusions and give rise to a spotty transmission diffraction pattern originating from the bulk of the islands and not from the surface. In contrast to LEED is RHEED in general not an exclusive surface process. Most surfaces are rough and the diffraction pattern is produced in transmission through the surface asperities, making RHEED

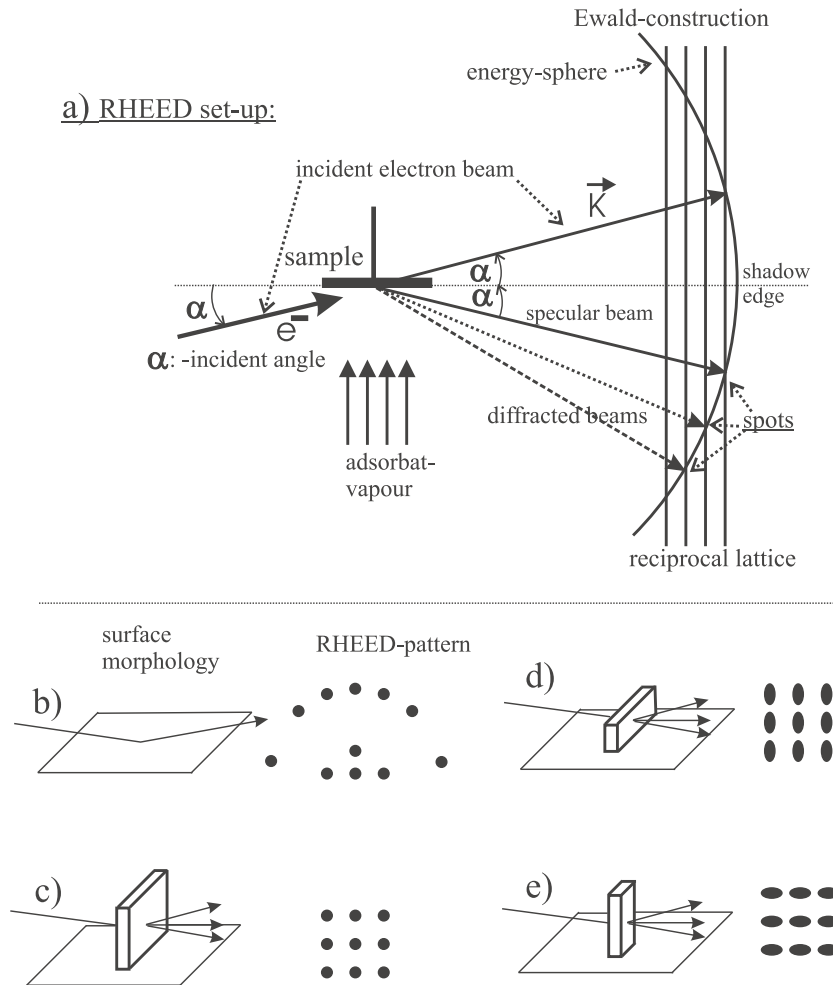


Figure 2.8: a) Experimental set-up for RHEED measurements. b,c,d,e) Surface morphology and expected RHEED-patterns. Panels c,d,e) shows the influence of the crystal shape on the form of the transmission pattern.

more useful than LEED in determining the crystal structure of rough surfaces where LEED fails to work.

An example of a 'true' reflection pattern is presented in fig.2.9a and sketched in fig.2.8b. A diffraction pattern obtained in transmission is presented in fig.2.9b and sketched in fig.2.8c,d,e. The latter show the influence of the crystal shape on the form of the transmission pattern. The light spots or streaks are called beams since they originate from the electron beams hitting the screen. A RHEED pattern consists, in analogy to LEED, of a map of the reciprocal surface lattice if the surface is smooth; in case of a rough surface the electrons probe essentially the bulk lattice. Probing the reciprocal lattice means that, e.g., a small interplanar distance in the crystal corresponds to a large separation of neighbouring beams in the diffraction pattern and vice-versa. The beam undergoing a mirror reflection (fig.2.8a) is called the specular beam. RHEED-electrons, especially those of the specular beam, provide a powerful tool in the study of various features of crystal growth. The grazing incidence of the primary electron beam makes RHEED very sensitive to lateral roughness. For example, measurements of the specular beam were used to study the surface morphology of the growing film and to calibrate the deposition rate of the adsorbate flux in molecular beam epitaxy [39]. We now turn to a phenomenological description of RHEED intensity oscillations and refer to fig.2.11. To keep the discussion as simple as possible, only pure electron reflection will be considered which means that one only concentrates on the intensity variation in the specular beam.

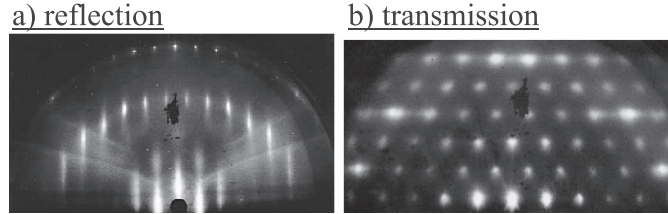


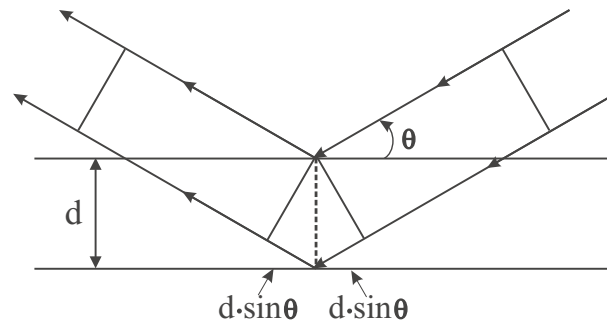
Figure 2.9: a) RHEED pattern observed from a flat surface. It refers to a $c(2 \times 2)$ true-RHEED reflection pattern obtained from a 9 ML thick Ag-film grown on a Nb(001) surface. b) RHEED-transmission pattern from an Ag film of 24 ML thickness deposited on a Nb(001) surface.

Table 2.1: Typical RHEED settings.

acceleration voltage	20kV
primary e-beam intensity	$\sim 3\mu\text{A}$
grazing angle	$\sim 0,3^\circ$
specular beam current ¹	$\sim 3\text{nA}$
transfer width parallel to the e-beam	$\sim 3500\text{\AA}$

In many molecular beam epitaxy studies the RHEED-intensity oscillates as a function of the deposition time. There are two simple models that are thought to explain this phenomena [42]. One model, favoured by the 'channeling school', is based on the idea that the electrons that impinge on a rough surfaces are scattered in many directions different from the specular beam thereby reducing the intensity of the specular beam. Steps provide a mechanism of diffuse scattering of the electron beam. As the step density increases the specular reflected intensity will decrease. If the surface morphology cycles from islanded to flat, the RHEED-intensity varies accordingly as depicted in fig.2.11. In this picture, the strength of the oscillations, i.e. the ratio of the peak maximum to minimum, should be independent of the angle of incidence of the primary electron beam, contrary to what was measured. Measurements have shown that the strength of RHEED-oscillation are very well dependent on the angle of incidence [36]. This finding strongly supports the view of the 'interference school' which explains the occurrence of the RHEED-oscillations by the interference of electron beams reflected from the top and bottom faces of the growing layer. Here the intensity is thought to decrease because the path length from the RHEED-source to the RHEED-screen (Faraday-cup) is different for electrons reflected from the top of the filled layer of atoms compared to those which are reflected from the tops of the growing layer. It could indeed be verified that in the case of constructive interference the RHEED-oscillations are suppressed, whereas in the destructive interference case the strength of the RHEED-oscillation are maximised [36, 42]. In the situation of destructive interference (see fig.2.10) RHEED-intensity oscillations appear due to the continuous change of the terrace occupation during deposition (see fig.2.11). As each growing layer proceeds from zero coverage through half filling and finally to a complete layer (see fig.2.11) the specular intensity cycles through one period. However, in both models (i.e. diffuse scattering or destructive interference) the period of a oscillation corresponds to the time needed to deposit a layer. Table 2.1 shows typical parameters used in RHEED experiments. The calibration of the evaporation rate was exclusively based on RHEED intensity oscillations recorded at very low grazing incidence (as low as $\theta = 0.3^\circ$). The latter condition guarantees that the reflected RHEED-beam penetrates less than 1 ML deep into the sample and hence picks up information only from the bottom and the top of the growing layer [42, 36].

¹For reflection at a smooth W(001) surface.



$$\text{path-difference:} \quad 2d \cdot \sin \theta$$

$$\text{phase-difference:} \quad k \cdot 2d \cdot \sin \theta$$

$$\text{constructive interference:} \quad k \cdot 2d \cdot \sin \theta = 2n\pi$$

$$\text{destructive interference:} \quad k \cdot 2d \cdot \sin \theta = (2n+1)\pi$$

Figure 2.10: Schematic representation of electron reflection at two levels of a layer (top and bottom faces). The quantity 'd' denotes the thickness of the layer, θ the angle of incidence and 'k' the wave vector of the RHEED-electrons. The latter is given by $k = (2\pi\sqrt{2meU})/h$, where m and e are the electronic mass and charge, respectively, 'U' stands for the acceleration voltage and 'h' for Planck's constant. At $\theta = \arcsin(2n\pi/(2kd))$ constructive interference occurs, $\theta = \arcsin((2n+1)\pi/(2kd))$ refers to destructive interference, and 'n' denotes an integer.

2.2.2 Auger Electron Spectroscopy (AES)

Auger electrons result from an atomic de-excitation process which is independent of the type of excitation and is caused either by photon absorption or by electron impact. (In exceptional cases Auger emission can also occur as a secondary process following the capture of an electron from the K-shell by the atomic nucleus.) In this work electrons of 1.8 keV primary energy are used throughout to create holes in the core-levels of surface atoms. Figure 2.12 shows two possibilities of re-occupying a core-state that has been depleted by a primary excitation. In both transitions the hole is filled by a first electron from an upper level (i.e. by a more weakly bound electron). The energy gain is either transferred to an X-ray photon (left side in fig.2.12), or used to excite a second electron which then escapes into the vacuum. This electron is called an 'Auger-electron'. The kinetic energy of the emitted Auger electron is determined by the binding energy difference of the above mentioned first and second electron, reduced by the work function of the sample surface. This binding energy difference is specific to the chemical nature of the respective atom. Therefore, AES constitutes the main technique in determining the chemical composition of the surface. Checking the cleanliness of the surfaces under study represents an important example. In the present work AES was used to examine the growth mode and the deposition rate. AES is also used as a standard method to characterise the composition and to measure the thickness of thin films. The latter application exploits the damping of the AES-signal by energy losses of the outgoing electron through electron-electron interaction as it traverses the respective material toward the detector [45]. The determination of film thickness in terms of monolayers (MLs) makes use of the fact that the AES-signal changes in a characteristic way during film growth. The Auger signal of a deposited film is expected to continuously increase whereas that of the substrate should continuously decrease during film growth as (i) it becomes less directly exposed to the primary electrons and (ii) –as mentioned above– the emitted Auger signal is damped as it traverses the respective film material toward the detector. In the case of a monolayer-by-monolayer growth these competitive effects result in an overall-dependence of the AES-signal on

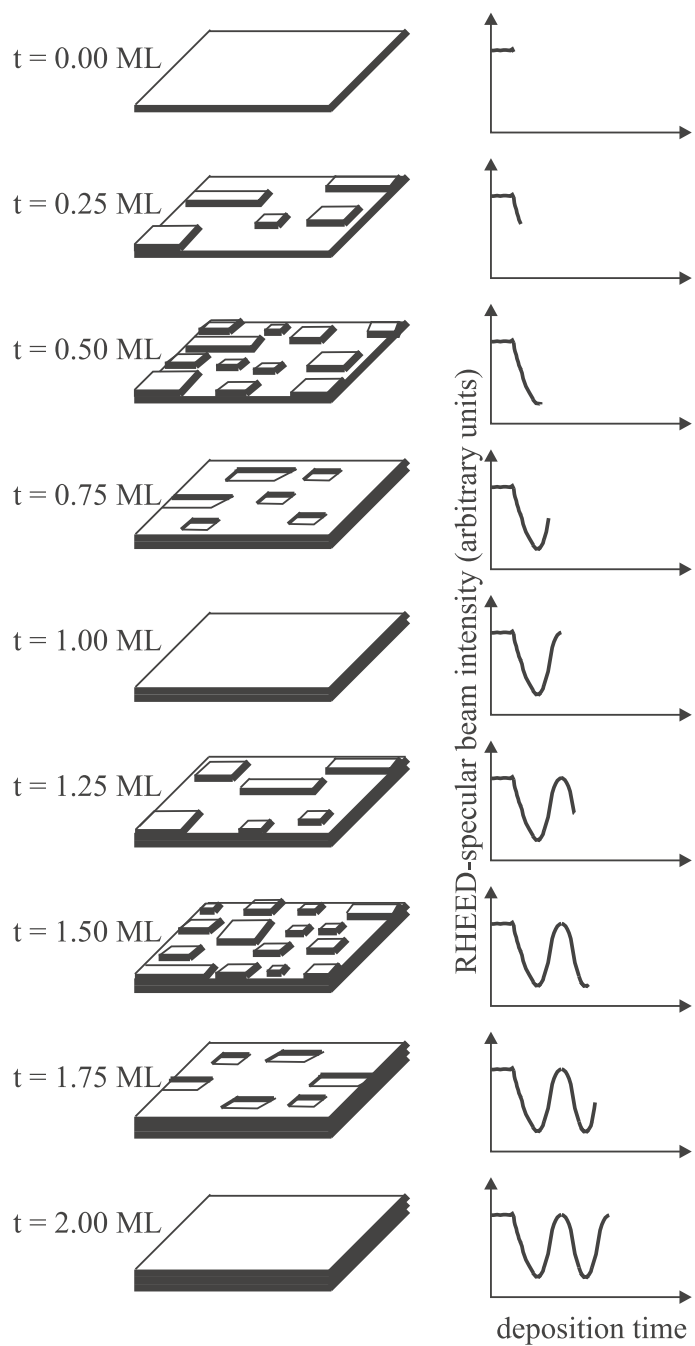


Figure 2.11: Dependence of the RHEED specular beam intensity on the surface coverage in the range of 1-2 ML coverage ([39]).

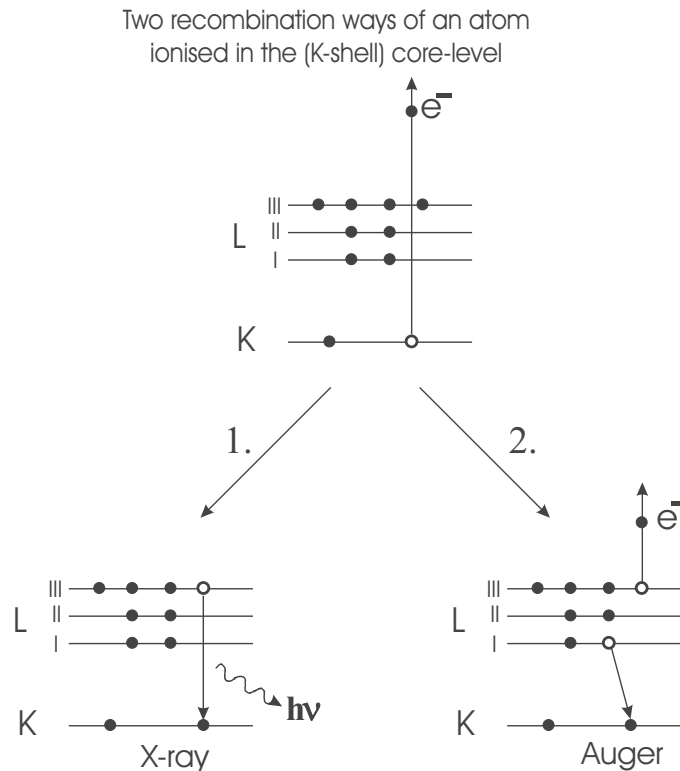


Figure 2.12: Transition possibilities of re-occupying an empty core-hole state in the K-shell: 1. Optical transition associated with the emission of an X-ray photon; 2. L-K transition of an electron transferring the energy gain to an outgoing (Auger-) electron.

the deposited material such that time-linear segments appear which are separated by distinct break-points upon the completion of full monolayers and display a slope that decreases from segment to segment. Table 2.3 summarizes the typical parameters used in AES. An AES intensity curve is sketched in fig.2.13 in the case of a layered growth mode.

Chemical shifts in the energy position of the Auger-signal (observed mostly as a change in the shape of the Auger signal) can be caused by a change of the bonds between the Auger emitting atom and neighbouring atoms. This change, however, is much better accessible by photoelectron spectroscopy (PES) which probes the energy spectrum of the valence electrons.

2.2.3 Photo-electron spectroscopy (XPS, ARUPS)

Photoelectron spectroscopy (PES) [46] has emerged as the standard method in the study of occupied electronic states of surfaces and thin films. In the photoelectron emission process the electronic system absorbs a photon and emits an electron, the so-called photoelectron. Clearly, the energy of the photon must be greater than the binding energy of the states to be ionized. Thus, core-levels are only accessible with X-ray photons. More information and a much better energy resolution [46] can be obtained by using ultraviolet photoelectron spectroscopy (UPS) which probes the energy bands of the valence and conduction electrons. In its angle resolved version (angle resolved photoelectron spectroscopy (ARUPS)) a maximum in an ARUPS-spectrum corresponds to a transition from an occupied to a non-occupied band, a process in which the energy and the crystal momentum (the ' \mathbf{k} -vector') is conserved. Figure 2.14 sketches a 'vertical' interband transition in photoelectron spectroscopy. The transition is called 'vertical' because the wave vector of the initial bound state is identical with the wave vector of the unoccupied state into which the transition takes place. The electron of the initial

Table 2.2: Typical settings used in AES.

electron-gun	kinetic energy of primary electrons sample current primary e-beam diameter on the sample	1.8 keV 1-3 μ A 0.2-1mm
sample	modulation voltage for E < 100eV E \geq 100eV	1-1.5 eV 3-5 eV
electron analyzer	angle resolution inlet-/exit slits (apertures)	$\pm 12^\circ$ 22mm(ϕ)
Lock-In-amplifier	sweep-rate integration-time	0.2-1eV/s 0.1-3s
data acquisition settings	energy step-wide time per energy step	0.2 eV 1-3s

state is promoted to an unoccupied band at a k-point for which:

$$h\nu = \varepsilon_f - \varepsilon_i \quad (2.2)$$

holds. Here $h\nu$ denotes the energy of the photon, ε_i the energy of the initially occupied state and ε_f refers to the final state that becomes occupied at the end of the transition. Actually, the conservation of the crystal momentum has the form

$$\mathbf{k}_f = \mathbf{k}_i + \mathbf{k}_\gamma$$

where \mathbf{k}_γ denotes the wavevector of the photon. For visible and ultraviolet light the absolute value of this vector ranges from $\sim 3 \cdot 10^{-3} \text{\AA}^{-1}$ to $10 \cdot 10^{-3} \text{\AA}^{-1}$ whereas the absolute values of the electronic \mathbf{k} -vectors within the associated Brillouin zone are typically by a factor of 100 larger. Hence, \mathbf{k}_γ may be neglected in the equation of momentum conservation.

In general Eq.(2.2) applies only very roughly. The so-called ‘one-particle energies’, $\varepsilon_f, \varepsilon_i$, are customarily obtained from self-consistent calculations based on density functional theory (DFT). The salient point in this approach to the many-electron problem consists in mapping the interacting N -electron system under study onto a non-interacting system whose electronic density is identical with the original density $\rho(\mathbf{r})$. To achieve this conservation of $\rho(\mathbf{r})$ one has to mimic the effect of electron-electron interaction by modifying the ‘external’ Coulombic potential (set up by the atomic nuclei). Surprisingly, this simulation of the electronic pair-interaction can rigorously be accomplished by simply adding a certain (local) one-particle potential which consists of a Poisson integral formed with $\rho(\mathbf{r})$ and the so-called exchange-correlation potential. The non-interacting substitute system can be described by a Slater determinant built from N Bloch-states if one is dealing with a perfect solid (crystal). The Schrödinger equation of the substitute system can be decomposed into N one-particle equations, the so-called ‘Kohn-Sham-equations’ of which the Bloch-states are solutions. They are associated with eigenvalues $\varepsilon_n(\mathbf{k})$ of which ε_f and ε_i are just two representatives.

As has been shown by Fritsche [47, 48] the DFT-scheme, that was originally devised only for the electronic ground-state, can be extended to excited states, for example, to those which are created by photon absorption. However, as has already been alluded to above, the excitation energy cannot simply be expressed as $\varepsilon_f - \varepsilon_i$. In actual fact the photon energy equals the difference between the initial electronic total energy E_i the respective energy E_f after completion of the transition:

$$h\nu = E_f - E_i \quad (2.3)$$

As has been shown by Fritsche [48] and by Fritsche and Gu [49] the right-hand side of Eq.(2.3) can be rewritten so that

$$h\nu = \varepsilon_f - \varepsilon_i + \Delta \quad (2.4)$$

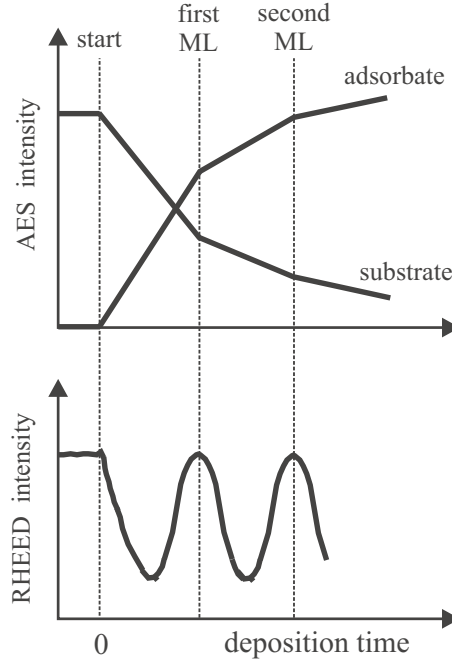


Figure 2.13: Schematic graph of the intensities associated with Auger electrons from a film and its substrate (top panel) and of the RHEED intensity (bottom panel) as a function of the film coverage for a layer-by-layer growth mode.

where Δ is kind of a relaxation energy connected to the rearrangement of the electrons as the system undergoes the transition. Clearly, this relaxation energy per atom is conceivably minute and will in general be of the order of 10^{-23} eV if the fundamental volume V of the solid contains $\approx 10^{23}$ atoms. In PES, however, one measures the total energy difference $E_f - E_i$ to which all 10^{23} atoms contribute. So, Δ may well be of the order of 1 eV.

The various contributions to $E_f - E_i$ are illustrated in fig.2.14. The quantity Δ is commonly termed ‘many-body correction to the one-particle energy difference’. If the unoccupied state lies above the vacuum-level where an electron can escape into the vacuum, the photo-electron can be detected and analyzed with the aid of an energy analyzer. The kinetic energy of the emitted photo-electron is given by:

$$E_{kin} = h\nu - (\epsilon_{Fermi} - \epsilon_i) - \Phi_{sample} - \Delta_i \quad (2.5)$$

where Φ_{sample} is the work function of the sample. When the analyzer is brought into electric contact with the sample the measured kinetic energy can be broken down to the following contributions:

$$E_{kin}^{A1} = h\nu - (\epsilon_{Fermi} - \epsilon_i) - \Phi_{analyzer} - \Delta_i \quad (2.6)$$

where $\Phi_{analyzer}$ is the work function of the analyzer. The interconnection of these quantities is illustrated on the left-hand side of fig.2.15. The binding energy $E_B = \epsilon_{Fermi} - \epsilon_i$ of the initial band state can be determined if one knows $\Phi_{analyzer}$ and Δ_i . In the practical application of PES (for example ARUPS) the kinetic energy of the electrons is measured relative to the Fermi-level of the sample. It is hence common practice to identify the origin of the energy axis in a recorded spectrum (where the kinetic energy is given by equation (2.6)) with the Fermi-edge beyond which the PES-signal drops to zero. The kinetic energy of the electrons emitted from the Fermi-level is according to eq.(2.6):

$$E_{kin,Fermi}^{A1} = h\nu - (\epsilon_{Fermi} - \epsilon_{Fermi}) - \Phi_{analyzer} - \Delta_{Fermi} = h\nu - \Phi_{analyzer} - \Delta_{Fermi} \quad (2.7)$$

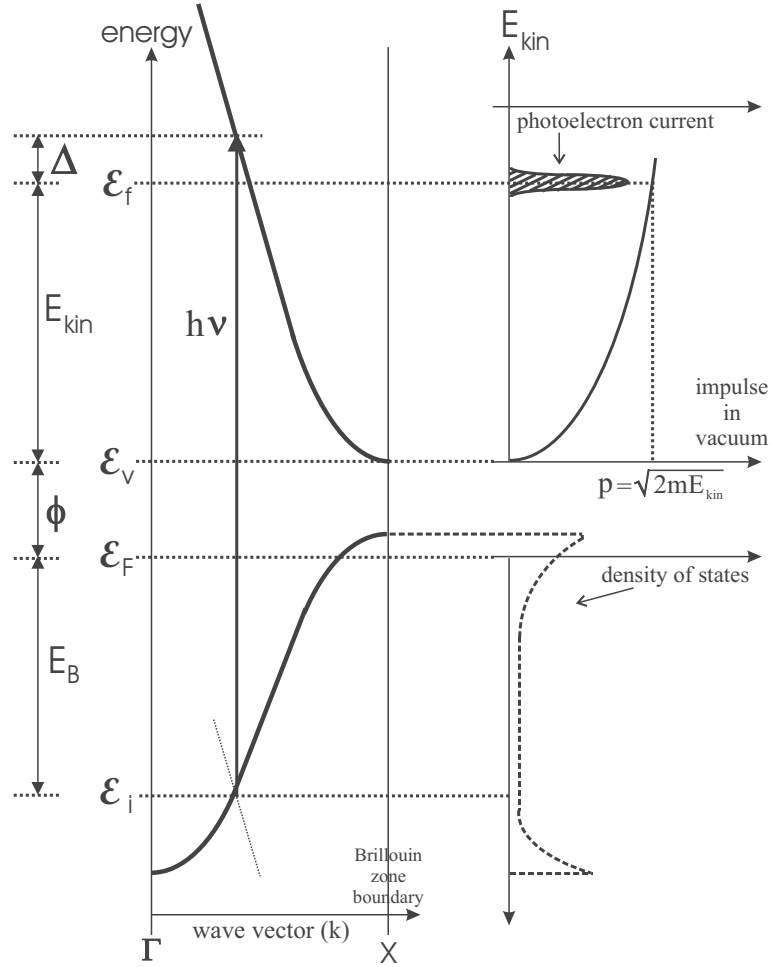


Figure 2.14: Left side: Vertical inter-band transition in photo-electron spectroscopy. Right side: Relation between the combined density of states and a peak in UPS.

where Δ_{Fermi} is the respective many-body correction. If we choose $E_{kin,Fermi}^{A1}$ as the origin of the energy scale (i.e. as energy zero), the measured kinetic energy can be decomposed then into:

$$E_i^{spectrum} = E_B - (\Delta_i - \Delta_{Fermi}) \quad (2.8)$$

Thus, the energy measured in PES differs from the binding energy of the depleted state by the difference of the many-body corrections referring to the depleted state and that at the Fermi-level. For Gd the energy $E_i^{spectrum}$ was shown to differ by 3.5 eV from E_B [50]. In the case of transition metals and noble metals the correction Δ_i is smaller than 1 eV . The difference $\Delta_i - \Delta_{Fermi}$ is therefore of the order of a tenth's of a Volt. The energy difference $\Delta_i - \Delta_{Fermi}$ is zero by definition if one measures photoelectrons that originate from the Fermi-level.

The procedure of shifting the energy scale of the analyzer such that the kinetic energy of electrons from the Fermi-level refers to zero energy can simply be achieved. One only has to shift the analyzer potential by an amount U so that

$$e \cdot U = \Phi_{analyzer} + \Delta_{Fermi} \quad (2.9)$$

The measured kinetic energy is then given by:

$$E_{kin}^{A2} = h\nu - E_B - (\Delta_i - \Delta_{Fermi}) \quad (2.10)$$

Hence, the binding energy of the initial band state can be expressed as:

$$E_B = h\nu - E_{kin}^{A2} - (\Delta_i - \Delta_{Fermi}) \quad (2.11)$$

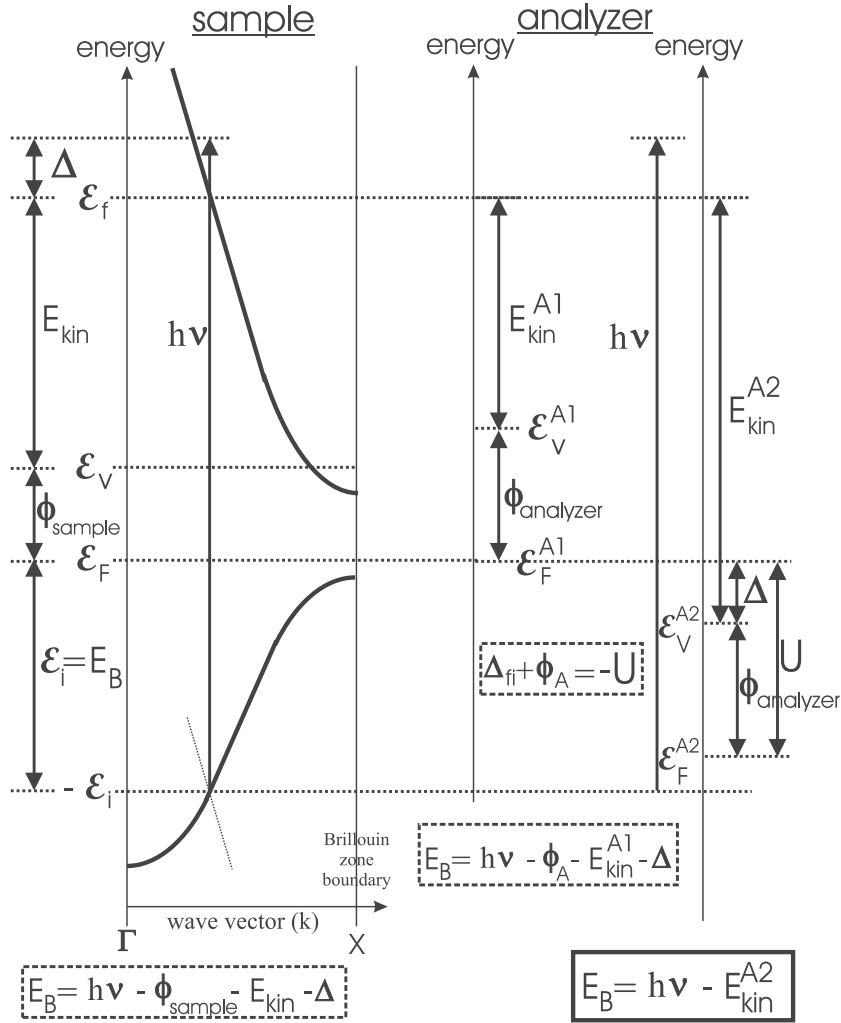


Figure 2.15: Left: interconnection of the quantities relevant to the analysis of ARUPS. Right: Correlating the energy scales of the interband-photoelectron emitter and the analyzer.

Eq.(2.10) reveals a fact which remains rather unclear in the entire literature on photoelectron spectroscopy. Obviously, the energy E_{kin}^{A2} measured by a photoelectron spectrometer can only be related to the electronic binding energy E_B if $\Delta - \Delta_{Fermi} = 0$. Only for states close to the Fermi-level $\Delta - \Delta_{Fermi}$ may be expected to remain negligibly small.

Another problem of ARUPS is the refraction of photoelectrons at the insufficiently known surface barrier as a result of which the \mathbf{k}_{\perp} -component is only known within a considerable margin [46]. However, the in-plane component \mathbf{k}_{\parallel} of the photo-electron is conserved in the photoemission process [46] (see fig.2.16), making ARUPS a good technique to determine the $E(\mathbf{k}_{\parallel})$ dispersion of the emitted photoelectrons. The k_{\parallel} -values of the initial states can be calculated from $k_{\parallel} = \frac{1}{\hbar} \sqrt{2m_e E_{kin}} \cdot \sin \theta = \frac{1}{\hbar} \sqrt{2m_e (h\nu - \Phi - |E_B|)} \cdot \sin \theta$ where θ is the emission angle.

Table 2.3 and 2.4 summarise the parameters used in UPS and XPS, respectively.

2.2.4 Auger and photo-electron diffraction (AED and XPD)

In Auger (AED) and (X-ray) photo-electron diffraction [46, 53, 54, 55] the electrons are detected in the forward direction of their propagation as they leave the atomic source. This contrasts with LEED where the current to the detector is essentially in the opposite direction of the primary beam. More-

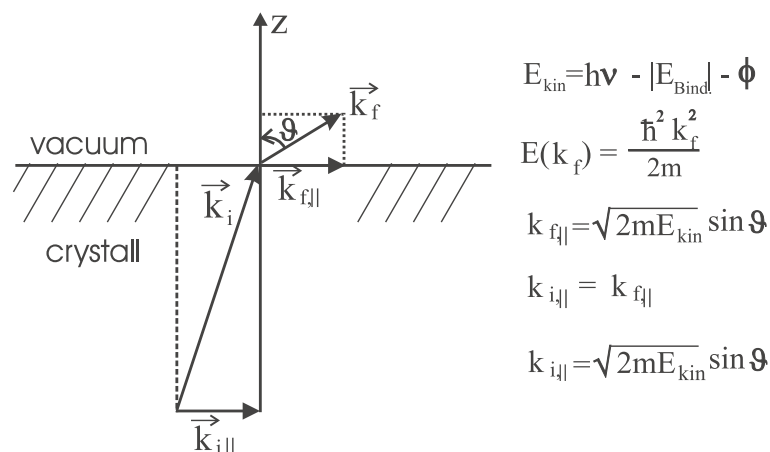


Figure 2.16: Conservation of the in-plane component of the photoelectronic k_{\parallel} -vector at penetration into the vacuum.

Table 2.3: Typical settings for ARUPS

excitation	photons	<i>HeI</i> α <i>NeI</i> α	21.2175eV 16.8476eV
electron analyzer	angle resolution		$\pm 1^\circ$
	constant pass-energy (CAE)	with/without polarizer	2.0/5.0eV
	inlet-/exit slits		6x15mm(ϕ)
data acquisition settings	energy-resolution	whit/whitout polarizer	60/150meV
	width of the energy step	whit/whitout polarizer	40/60meV
	time per energy step	whit/whitout polarizer	2 – 3/10s

over, in contrast to LEED, Auger or photo-electron diffraction provides more directly information on the crystal structure in real space. Typical settings for X-ray photoelectron diffraction are given in Table 2.5. The main features of the scattering mechanism are illustrated schematically in fig.2.17. Electrons, escaping from the near surface region after either an Auger emission or an atomic photoemission process, are strongly scattered (diffracted) in the forward direction by the potentials of the atoms along their path if the kinetic energy of the electrons exceed some hundred eV. If these atoms form a regular array, as in a crystalline solid, this strong forward scattering focuses the outgoing electrons into beams along directions of high crystalline symmetry. Thus, if one measures Auger or photo-emitted electrons for example as a function of angle across a crystal surface, one observes a very non-uniform distribution, strongly peaked along lines of densely packed atoms. Furthermore, since Auger-electrons or photo-electrons emitted from core-levels are element specific one can collect only those which are emitted from the atoms deposited on the substrate and determine the array

Table 2.4: Typical XPS settings.

X-ray source	<i>AlK</i> α	1486eV
electron analyzer	angle resolution	$\pm 12^\circ$
	constant pass-energy	10 eV
	inlet-/exit slits	6x15mm(ϕ)
data acquisition settings	energy resolution	1eV
	energy step width	0.2 – 0.5eV
	time per energy step	1 – 10s

Table 2.5: Typical XPD settings.

X-ray source	$AlK\alpha$	1486.6eV
electron analyzer	angle resolution	$\pm 1^\circ$
	constant pass-energy	40eV
	inlet-/exit- slits	6x15mm(\emptyset)
	energy resolution	5eV
data acquisition settings	angle step	1°
	time per angle-step	60 – 120s

of these atoms. As fig.2.17 shows, a perfect 1 ML coverage should give a featureless uniform angular distribution, in a perfect (001)fcc film of 2 ML the outgoing current will be peaked around 45° when the current is scanned along the $\langle 100 \rangle$ azimuth. Finally, as one has completed a 3 ML coverage, there will be an additional central [001] peak from electrons emitted along the surface normal.

2.3 The W(001) and Nb(001) substrates

Because the key requirement for growing films with a hexagonal phase modification consist in a strong bonding to the substrate, I have paid great attention to the preparation of suitable substrates. The tungsten samples used in the present experiments were discs of a single crystal with a diameter of 10 mm and a thickness of 0.5 mm which were polished to mirror quality and oriented to within 0.05° of the (001) orientation. The orientation was checked with X-ray Laue photographs. The sample was gently held by thin and small tantalum sheets on the W support disc of the crystal holder. The W-support was subject to prolonged heating up to a temperature of 2500K before the W(001)-sample was mounted on it. The tungsten crystals were cleaned in a usual manner [56] by prolonged heating in oxygen followed by flashing to 2500 K until any AES-signal from impurities had faded. (The AES-signal ratio W:O and W:C was then about 300:1.) The open W(001) surface seemed to be more reactive to oxygen than the dense W(011) surface: the removal of the last traces of oxygen contamination from the W(001) surface proved to be quite difficult. The (001) surface of tungsten displays a four-fold symmetry and is called an 'open surface' because of its low atomic density that results from a lattice constant of 3.16\AA . As we shall discuss in the main sections, this large lattice constant is of crucial importance for growing films in an unusual hexagonal stacking mode of materials like Cu and Pd. However, in order to grow also films of Ag and Au in such a stacking mode, one needs an even larger lattice constant of a substrate with a four-fold symmetry.

The (001) surface of Nb has that desired periodicity, but, unfortunately, the preparation of a flat Nb surface without any traces of contamination, turned out to be a very difficult task. In contrast to W(001), Nb(001) could not be cleaned by flashing. This is just a consequence of the lower melting temperature of Nb and, moreover, it is more reactive than tungsten. The removal of oxygen from Nb and also Ta surfaces without seriously damaging the surface perfection has been a major problem in nearly all the studies of these surfaces in the past [57]. The difficulty of removing oxygen from those surfaces originates in the high solubility and diffusivity of oxygen in these metals and, in addition, in the low vapour pressure of its suboxides. For example in Nb, the solubility has a maximum of 6 atomic percent at about 2050 K and decreases in the absence of an oxygen-containing environment only above this temperature due to desorption in the form of NbO and NbO₂. Even in UHV clean Nb absorbs oxygen at partial pressures [58] above 10^{-11} mbar. Thus, there is always an equilibrium concentration of oxygen in the Nb-bulk which acts as a source of surface oxygen upon re-cooling the heated Nb sample.

It took a considerable experimental effort to find a method of fabricating well ordered, flat, contamination-free Nb(001)-like surfaces with the required lateral periodicity (3.30\AA) of the bulk

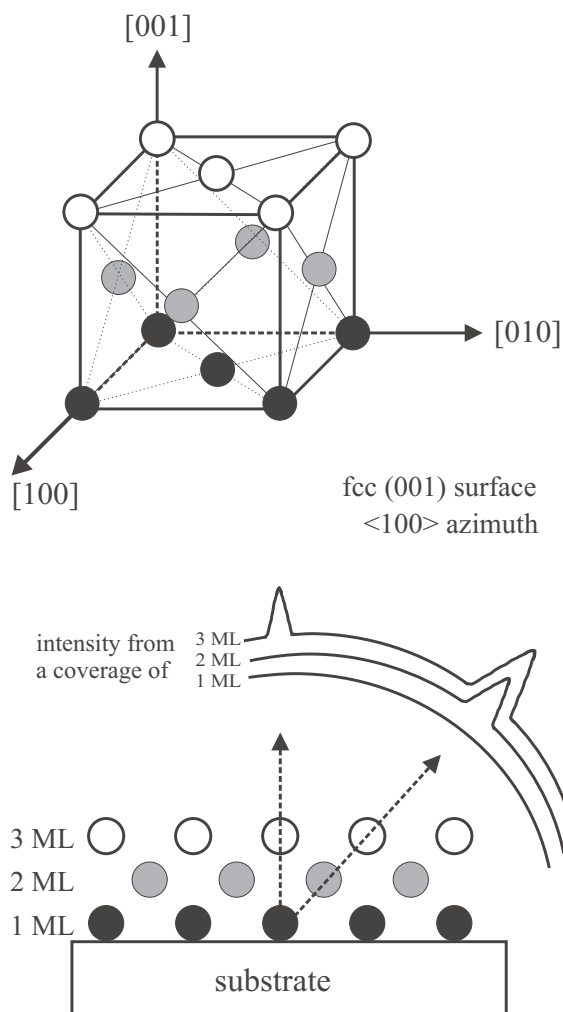


Figure 2.17: Schematic view of the electron forward scattering process and the relative positions of atoms in the first, second and third monolayer for (001) oriented growth in a (100) cross section of an fcc-crystal. Auger- or photoelectrons are focused along interatomic axes, giving rise to characteristic peaks in the outgoing current density that indicate occupation of sites in the second and third monolayer.

material [18]. As already emphasized above, a square lattice of this mesh size is necessary to grow films of Ag and Au in the envisaged hexagonal non-equilibrium modification.

The method that finally complied with that requirement is based on altering the chemical environment of the near surface region to such an extent that the contaminants (mainly oxygen) were depleted from the surface (deep into the Nb-bulk), while the lateral periodicity of the Nb(001)-surface was maintained. The depletion of oxygen from the substrate surface was achieved by depositing thick films, i. e. more than 10 MLs of Au or Pd on the surface, followed by annealing up to 1400 K. This process led to flat surfaces covered with a pseudomorphic monolayer of Au or Pd which was free of contamination. (The C:Nb and O:Nb AES-signal ratio proved to be as low as 1:500). That monolayer displayed the desired lateral periodicity of an (001) oriented Nb crystal.

3 Film thickness determination

The properties of thin films such as the electronic structure and film stability are strongly influenced by film thickness [59]. Hence, its measurement is of vital importance to a correct interpretation of the experimental results. A standard method used in the determination of the thickness of thin films is Auger electron spectroscopy (AES) [45]. As mentioned in Section 2, the measurement consists here in monitoring the change of the slope of the AES-signal as a function of deposition time. In the case of a monolayer-by-monolayer growth, the AES-signal increases linearly with time until a breakpoint has been reached beyond which the increase continues at a smaller slope. A breakpoint reflects the completion of a layer. However, in some cases the difference in the slopes of two consecutive segments of an AES-curve is so small that it becomes exceedingly difficult to identify the slope discontinuity. For that reason AES may be limited in its use if one wants to determine the absolute thickness of films. By contrast, in UPS the photoelectron current runs through well defined maxima and minima as the film forms layer by layer. These maxima and minima can easily be discerned and analysed. They are connected with the drastic changes of the electronic structure as the film grows. Photoelectron currents from HeI-ARUPS are particularly suited because their small escape depth puts a strong weight on the contribution of the film layers. Since UPS is used anyway as a standard method in the study of the electronic structure of surfaces, it may be convenient to exploit this pronounced side effect for a determination of the film thickness. But for this particular task RHEED has proved to be superior in every practical respect. The detection of thickness-dependent RHEED-oscillations is much simpler, it does not require an energy analyzer and is easier to interpret. It is this practical advantage which has made RHEED the essential tool in calibrating the flux from MBE sources [39, 42].

The ensuing sections are concerned with the application of the above three methods to films of Au, Ag, Pd, Cu and Co metal which were of particular interest to the objective of the present work.

As already emphasized, the layer-by-layer growth constitutes a precondition for the application of the three methods. All five transition metals bind strongly to the substrates W(001) and Nb(001) which ensures a complete wetting of the substrate surfaces by at least one pseudomorphic adlayer of the deposited metal. In fact, low-energy electron microscope (LEEM-) studies reveal that Co and Pd wet W(001) at least by two pseudomorphic MLs [60]. Our RHEED investigations indicate that the latter seems to be a general feature of metallic heteroepitaxy on W(001) and Nb(001) substrates. This is actually not surprising since the atoms of the first two adlayers have direct bonds to the substrate.

Once the deposition time for the completion of one or two pseudomorphic-MLs of a film has been measured, the deposition rate may be considered calibrated. (It had been verified by quadrupole mass spectrometer measurements that the respective metallic evaporator ensured a constant flux of atoms.) Since the first two adlayers grow with a density different from that of the respective bulk metal, one has to determine the ratio of these two densities if one wants to calculate the film thickness beyond those two adlayers from the deposition time and the evaporation rate. Moreover, if one wants to measure the growth rate in terms of layers, one needs to know the orientation of the film in addition. This information has been obtained in my experiments by using RHEED and XPD.

3.1 Films of Au metal

As stated above, the deposition of the various metals on W(001) was monitored by AES, UPS and RHEED. The RHEED chamber, as well as the main (spectroscopical) chamber, were equipped with evaporators. For a comparison and an illustration of the different behaviour of (011) and (001) surfaces, I have also included data on changes of the work function $\Delta\phi$ which refer to a cylindrical crystal [61]. The results are shown in fig.3.18.

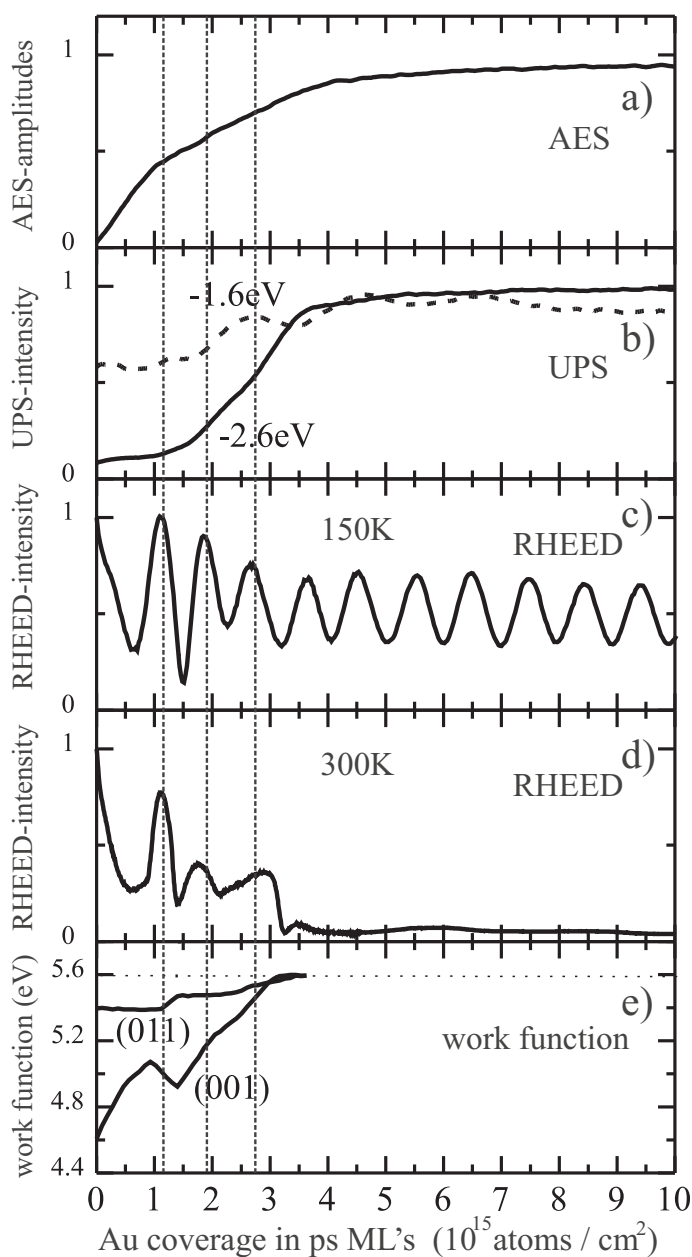


Figure 3.18: Changes during deposition of Au on W(001): a) of the Au AES peak-to-peak height, b) of the UPS intensity at -1.6 and -2.6 eV binding energy, c,d) of the RHEED specular beam in W [110] direction, and e) of the work function of (011) and (001) surface of a cylindrical crystal. The AES, UPS and RHEED intensities are normalized to their highest values. The vertical dashed lines interconnect correlated features. The correlation was established in the following way. The deposition in the RHEED chamber was stopped immediately after the maximum of the first, second and third oscillation period, respectively, had been reached. Then the sample was transferred quickly to the spectroscopic chamber where Auger-electron and photo-electron spectra were taken. This means that the AES and UPS spectra were obtained from samples in which the amount of absorbed Au or Ag corresponded to a little more than one, two and three RHEED oscillation periods, respectively. This is shown in fig.3.18 (and fig.3.22) with vertical dashed lines. The cases a), b) and c) refer to a substrate temperature of 150K, in the case of d) and e) the substrate temperature was 300K ([5]).

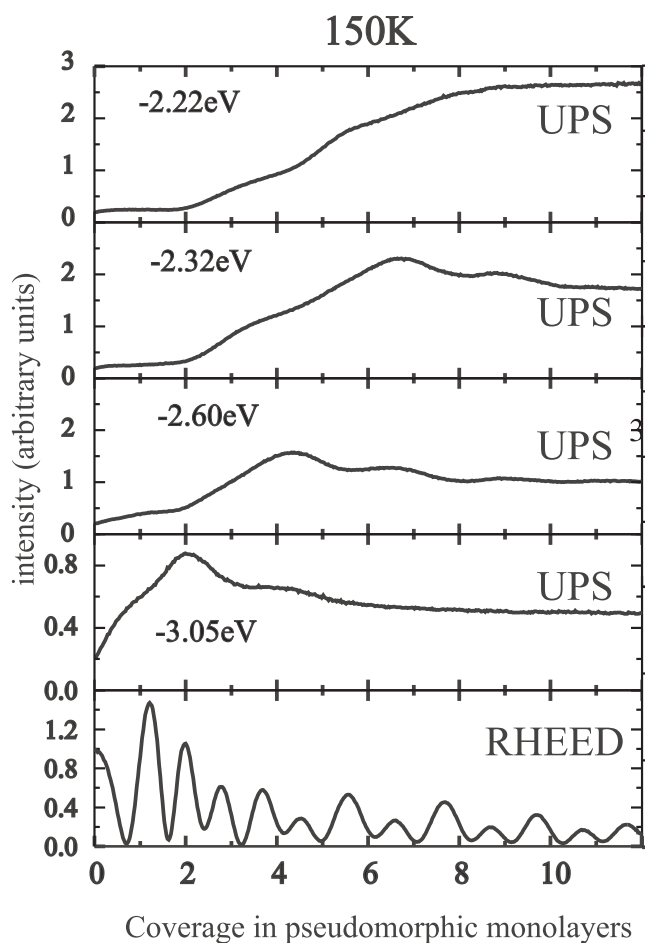


Figure 3.19: Photoelectron intensity vs. coverage recorded at selected energies from the growth of Cu on W(001) at 150K. The bottom panel shows the intensity of the specular RHEED beam parallel to the W [011] azimuth. The maximum of the second RHEED-oscillation coincides with the UPS-maxima which occurs at the -3.1 eV binding energy curve ([112]).

Although RHEED oscillations provide the most reliable criterion for layer-by-layer growth and for the number of deposited layers, cross-checking these RHEED-results by AES and UPS is indispensable. To organise an effective cross-checking the following strategy was pursued. Once the data acquisition on the dependence of the AES-, UPS- and RHEED-intensity vs. deposition time had been completed, the generated plots were searched for certain structures that appear in one of the plots and have counterparts in the other plots. Figure 3.18c shows the intensity oscillation of RHEED specular beam during the growth of Au on W(001) at 150K. Up to 25 oscillations can be observed, indicating a layer-by-layer growth mode [39, 42]. The experimental setup allowed the sample to be moved under UHV-conditions from one chamber to the other within 8 minutes. Because of this technical feature the three methods could be applied to the same sample at almost the same time which constitutes a vital prerequisite for the sought-for correlation of structures in the generated plots. In detail the procedure was executed along the following lines.

The deposition in the RHEED chamber was immediately stopped every time after the maximum of the first, second and third oscillation, respectively. The sample was then quickly transferred to the spectroscopic chamber where Auger-electron and photo-electron spectra were recorded. The situation at the three intermissions is indicated in fig.3.18 (and fig.3.22) by vertical dashed lines. To check the absolute position of the dashed lines on the axis of abscissae the AES-plot was carefully inspected. As is evidenced by fig.3.18, two breaks can be recognized in the AES amplitudes during

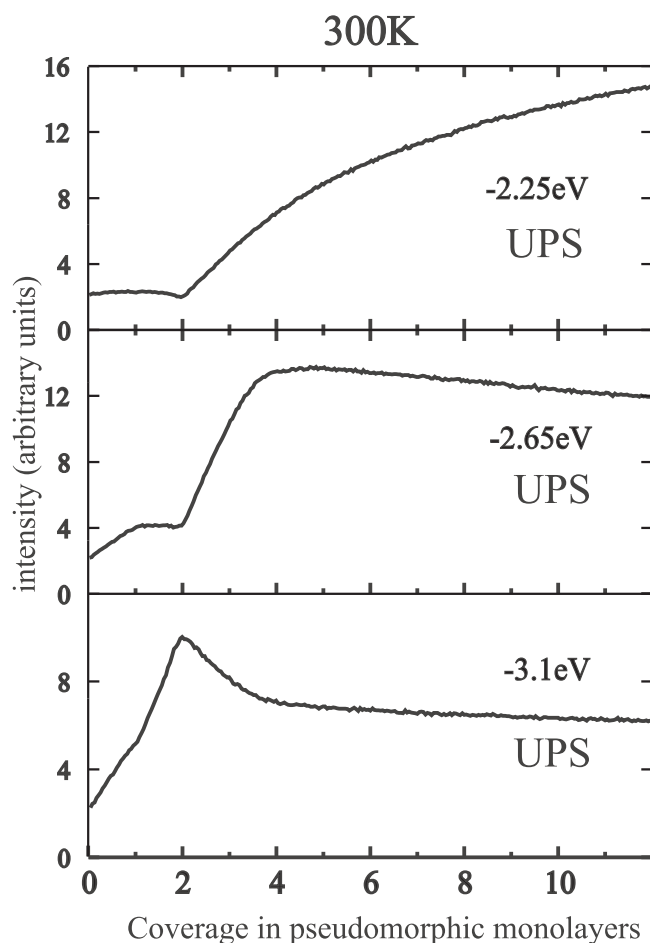


Figure 3.20: Photo electron intensity from Cu on W(001) recorded at selected energies at 300K ([112]).

the Au deposition. This is confirmed by Bauer et al [63] who studied the same system Au/W(001). Results obtained from a simultaneous measurement with a quartz microbalance support the interpretation that the first break corresponds to the completion of a pseudomorphic Au monolayer (10^{15} atoms per cm^2), and the second break to 4 absorbed Au monolayers. To make the check even more trustworthy, the first break in the AES curve (fig.3.18a) was additionally compared to the first break in the AES-curve recorded during Au deposition on a $[1\bar{1}0]$ oriented cylindrical single crystal of W metal. The surface of such a crystal comprises both the (011) and (001)-face. If one rotates the crystal with a constant angular velocity, a uniform layer of Au can be deposited on both surfaces at the same rate. During deposition the change of the work function ($\Delta\phi$) is monitored continuously. As for the W(011) face, the dependences of $\Delta\phi$ and the AES- signal on the Au coverage are well studied [64, 65, 66]. The first break in the AES-curve has been attributed to the completion of 1 ML. This amounts to a deposition of $14 \cdot 10^{14}$ atoms/ cm^2 . In the case of the Au/W(001)-system the work function attains a maximum at 0.9 pseudomorphic ML which corresponds to $10 \cdot 10^{14}$ atoms/ cm^2 and may be attributed to the completion of the first ML. The work function runs through a minimum at about the same abscissa where the second break in the coverage dependence of $\Delta\phi$ of the Au/W(011) system occurs. This abscissa is associated with $14 \cdot 10^{14}$ atoms/ cm^2 and corresponds to ~ 1.4 ML. Just at this abscissa the specular RHEED-intensity runs through its second and deepest minimum indicating that a large change occurs at this coverage. Different from this situation the first maximum in the RHEED-oscillations can be linked to a clear structural property: the completion of the first ML.

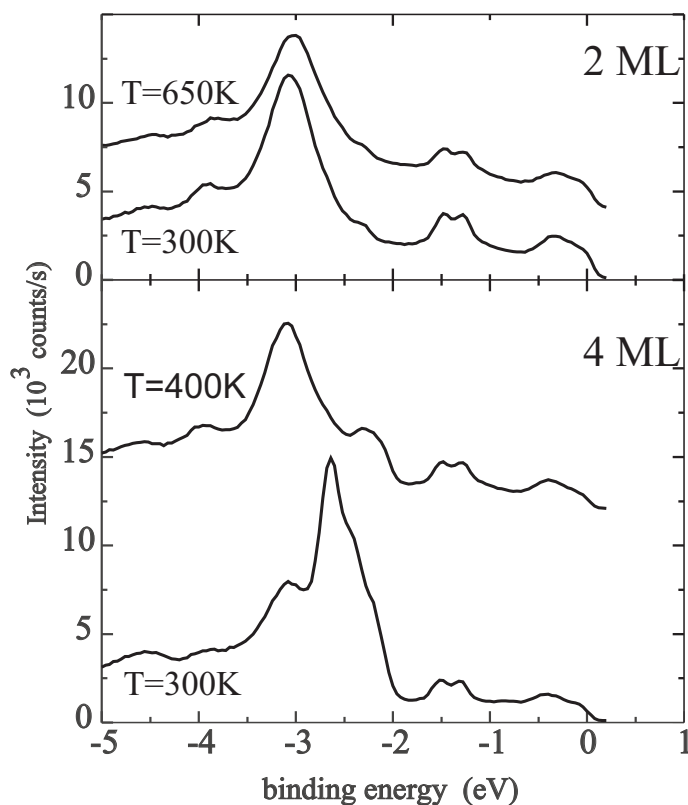


Figure 3.21: Ultra violet photoelectron spectra of Cu films deposited on W(001) at room temperature and for different annealing conditions: a) 2 ML film exposed to annealing for 90 s at 650K and b) 4 ML film exposed to annealing for 300 s at 400K. The UPS maxima at -3.0 eV binding energy represents the main structure in the spectrum of a thermally stable Cu overlayer ([112]).

3.2 Films of Cu metal

Figure 3.19 and 3.20 show plots of the RHEED- and UPS- intensity vs. Cu-coverage on W(001). Obviously the maximum of the second RHEED-oscillation coincides with the maximum of UPS intensity that corresponds to an electronic binding energy of -3.05 eV. As can be seen from Fig.3.21 that maximum represents the main structure in the spectrum of a thermally stable Cu overlayer.

Using a quartz microbalance for the determination of the film thickness, Bauer et al [64] could demonstrate in their study of the Cu/W(001)-system that a pseudomorphic double ML of Cu is thermally stable. This corroborates our conclusion that the second maximum in the RHEED-oscillations has to be attributed to the absolute coverage of two pseudomorphic ML of Cu.

3.3 Films of Pd, Co and Ag metal

In growing Pd films on W(001) we have proceeded along the lines of the preceding subsections. Again, we search for corresponding features in the dependence of the RHEED/UPS-signal on the Pd coverage which Fig.3.22 refers to. Here the second maximum in the RHEED-oscillations coincides with the maximum of the UPS-intensity associated with an electronic binding energy of -1.32 eV. Figure 3.23 shows that around this binding energy (-1.4eV) the main UPS-peak of the thermally stable Pd layer develops. Previous investigations of Pd on W(001) [67] had led to the conclusion that a pseudomorphic double layer of Pd is stable on W(001). The maximum of the second RHEED-oscillation may therefore be associated with the completion of the second pseudomorphic ML of Pd on W(001). In the case of Pd films this can be corroborated by following up the growth

to considerably larger thicknesses. At a deposition temperature of 150K more than 40 RHEED oscillations can be observed. The oscillation period attains a stable value approximately beyond the fourth maximum. As will be discussed in the ensuing section, the Pd film grows in a direction that is different from a stacking axis so that the deposited monolayers do not consist of close-packed Pd atoms. Hence, if one wants to correlate the deposition rate with the number of ML's per second, one has to know the orientation of the film with respect to the substrate. How this has been done will also be the subject of the next section. But once the orientation is known, one can use the rate ML/s obtained from the stable oscillation regime to scrutinize the result on the first two ML's. This has been done and yielded very good agreement.

In the case of Ag and Co films the deposition rate was determined much the same way.

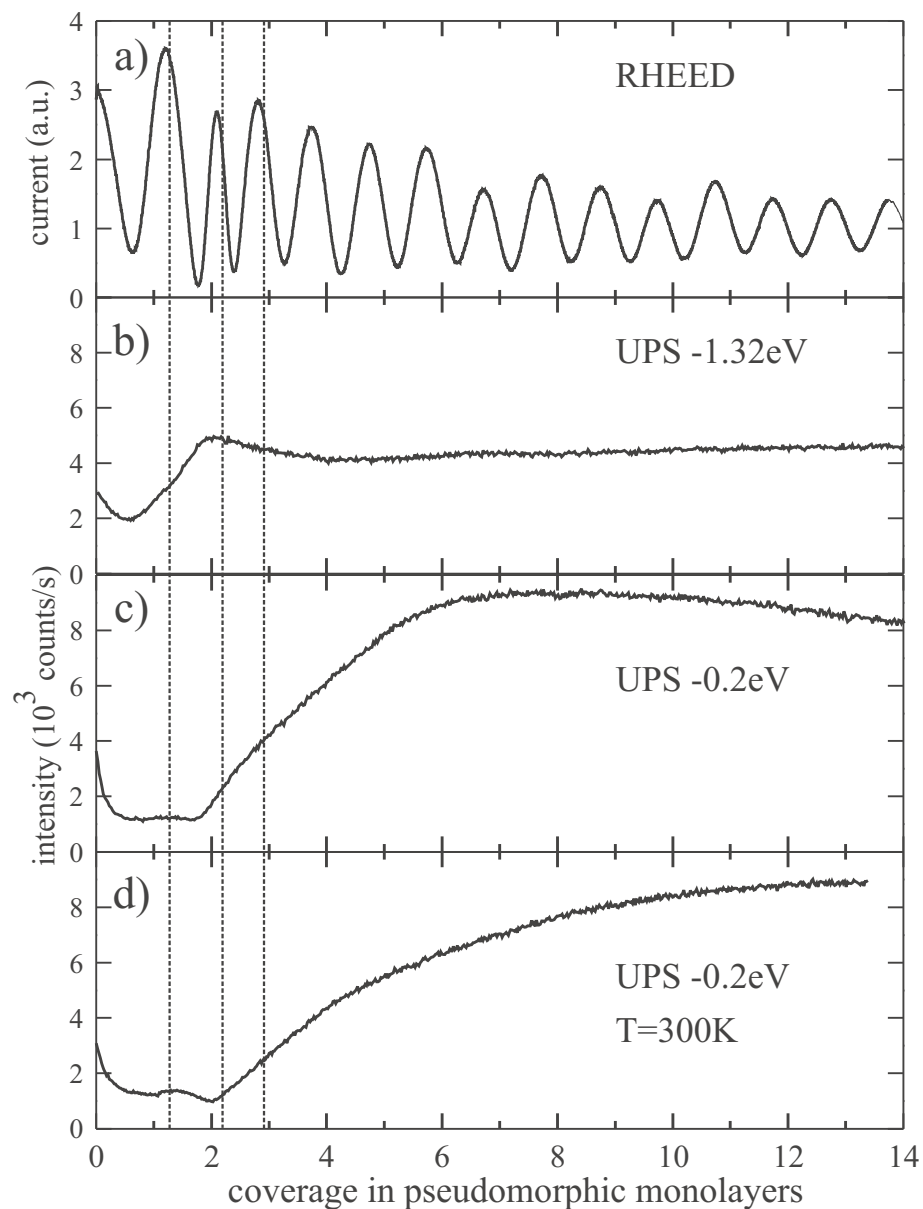


Figure 3.22: Dependence of the RHEED/UPS-signal on the coverage of Pd metal on W(001): a) RHEED-oscillations with the incident beam along the tungsten [011] azimuth. Substrate temperature: 150K. b) and c) UPS-intensity in normal emission upon Pd-deposition at 150K at the binding energies indicated. d) Same as c) but at 300K substrate temperature. Monolayer scale in units of the substrate atomic density. The vertical dashed lines are a guide for the eyes to locate correlated features ([11]).

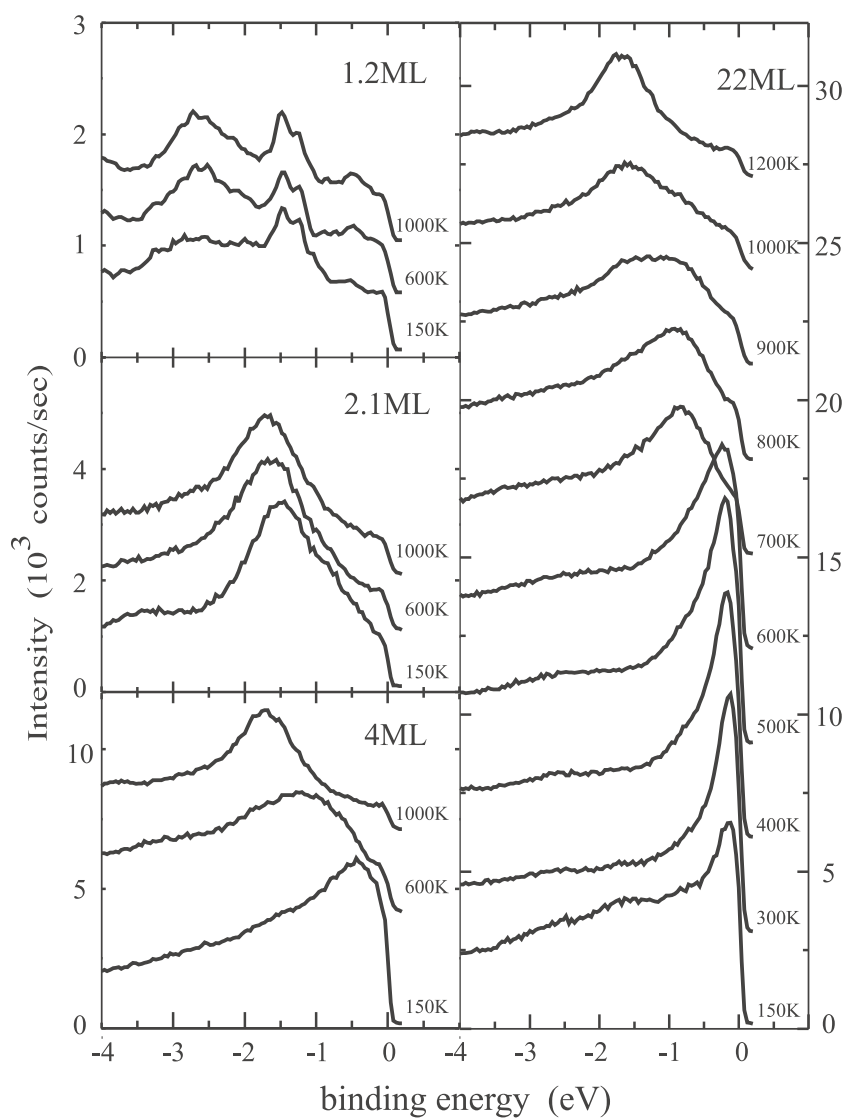


Figure 3.23: Ultraviolet photoelectron spectra for normal emission from Pd on W(001) for thicknesses of 1, 2, 4 and 22 ML. All depositions were made at 150K. The films were subsequently annealed for 90 s at the indicated temperatures ([11]).



Figure 4.24: a) The RHEED transmission pattern obtained from a lightly sputtered Nb(001)-surface. b) RHEED-transmission pattern originating from a Pd film of 20 ML thickness deposited on Nb(001). This diffraction pattern occurs typically with the epitaxy of late transition metals and noble metals on open (001)-surfaces of cubic substrates. In the two cases (a,b) the incident beam was parallel to the [011]-direction of the Nb(001)-surface.

4 The growth of late transition and noble metals on (001)-oriented cubic substrates.

4.1 Diffraction of primary electrons (RHEED,LEED)

The hetero-epitaxial growth of Co, Cu, Pd on W(001) is similar to that of Cu, Rh, Pd, Ag and Au on Nb(001). At the deposition temperature of 300K a Stranski-Krastanov growth mode occurs. The substrates are wetted by two pseudomorphic ML's, followed by the growth of 3-dimensional islands, which produce the centred RHEED-transmission pattern presented in Fig.4.24b. An exception to this is the growth of Au on Nb(001), where the ML-by-ML growth mode extends over more than two ML's, but with a poor long range order providing less structural information in RHEED. By contrast, a bright RHEED diffraction pattern from smooth Cu, Pd, and Ag films can be obtained when the films are deposited at low temperatures and subsequently annealed up to 500K. As the present work is strongly focused on the analysis and interpretation of these diffraction patterns, a detailed discussion of their appearance seems to be in order.

4.1.1 The pseudomorphic range

As mentioned above, if one deposits late transition or noble metals on W(001) or on Nb(001) the first two ML's form a pseudomorphic (1x1)-array (the black squares in fig.4.25). This becomes obvious from inspection of the RHEED-patterns. The adatoms occupy lateral hollow-site positions of the (001) substrate surface. These first pseudomorphic ML's are strongly dilated in the surface plane compared to the mesh size of their natural fcc (001)-face. For example, the pseudomorphic Pd ML's on Nb(001) are expanded by 44% which results in a next-nearest-neighbour distance of ($a_{\text{Nb}} = 3.30\text{\AA}$), quite different from its value in bulk Pd. This reflects the strength of the adsorbate/substrate bonding.

4.1.2 Beyond the pseudomorphic range. Growth between 2 and 3 monolayers.

The pseudomorphic range is characterized by the occurrence of a RHEED pattern that consists of (1x1) true reflections [68]. They are caused by (1x1) ordered domains that possess a pronounced long-range order. If the linear extension of this range decreases in one dimension, the pattern elements begin to elongate considerably in that direction [39]. Exactly this happens after the deposition of the first two pseudomorphic ML's addressed above. As the deposition continues beyond completion of those two ML's, the RHEED background increases and the (1x1) patterns gradually turn into straight lines (streaks) perpendicular to the surface (perpendicular to the RHEED-horizon [39, 40])

when the primary beam is oriented along the $[110]$ -direction of the substrate-surface. If the primary beam is oriented along the $[100]$ -direction of the substrate-surface, then ellipses (parabolic arches) appear connecting the Laue-reflexes from different zones. RHEED-patterns of this kind were observed and explained by Hopkins et al. [69], Stalder et al. [41], Mahan et al. [40] and Dulot et al. [70]. The straight lines and the parabolic arches are images of a set of parallel sheets in the 3d-continuation of the 2d-reciprocal lattice whose 3rd dimension extends perpendicular to the surface. These sheets develop from the (1×1) rods of the 3d-continuation of reciprocal lattice of the surface by gradually turning into planes whose intersection lines with the 2d-reciprocal lattice are in the $\langle 110 \rangle$ -direction of the substrate. These lines are shown in Figure 4.25. Their distance is given by $2\sqrt{2}\pi/(2a_{\text{bcc}})$ where a_{bcc} denotes the side length of the primitive mesh of the (001) surface and of the adjacent pseudomorphic ML's. This distance is by a factor of 2 smaller than the length of the diagonal of the primitive unit cell. Because of the four-fold symmetry of the latter the $[110]$ - and $[1\bar{1}0]$ -directions of the pseudomorphic ML's are equivalent, as a consequence of which two sets of equidistant planes (and associated lines) occur (s. fig.4.25a,b). Au films on Nb(001) were grown up to 25 ML's and subsequently annealed up to 500K. The lines one observes here may be viewed as if they had developed from a hypothetical pseudomorphic array of Au atoms where only every next nearest hollow site of the substrate is occupied. The distance of the corresponding lines (planes) that develop in going beyond 2 ML's must hence be shorter than the length of the diagonal of the primitive unit cell by a factor of 4. Fig.4.25d refers to the associated pattern of lines.

The RHEED patterns can be visualized by employing the so-called Ewald-construction [69, 39, 40, 70]. This requires to draw the Ewald-sphere in the 3d-continuation of the 2d-reciprocal lattice of the substrate surface and to find the intersections of that sphere with the above mentioned rods or planes. The radius of that sphere is given by the absolute value of the wavevector \mathbf{k}_p of the incident (primary) electrons. The sphere center is defined by the end point of the vector $-\mathbf{k}_p$ which is drawn from the origin of the 3d-continuation of the 2d-reciprocal lattice of the substrate surface. Because of the grazing incidence of the electrons the center of the sphere is slightly above the k_x/k_y -plane of the 3d-reciprocal lattice (if \mathbf{k}_z is perpendicular to the substrate surface). Consequently, the intersections of the rods with the sphere lead to dots forming circles. As soon as the planes have developed, the intersections display different shapes. If \mathbf{k}_p is in the $\langle 001 \rangle$ direction there are now intersecting lines at the sphere that have the form of parabolic arches which may be viewed as joining the zeroth and first Laue zones [69, 40, 39, 41, 70]. Changing the view angle from the $\langle 100 \rangle$ direction to the $\langle 110 \rangle$ direction the lines of intersection now turn into segments of a circle which appear as straight lines in the projection onto a screen that is approximately perpendicular to \mathbf{k}_p .

The described changes in the RHEED pattern are, in fact, observed and give strong support to our interpretation that the growth of the films beyond 2 ML's is characterized by a departure from the square mesh structure of the pseudomorphic layers and by the formation of layers where the interatomic distances are getting closer to the natural equilibrium distances as the build-up of additional layers proceeds. But a distinct periodicity perpendicular to the directions $\langle 110 \rangle$ or $\langle 1\bar{1}0 \rangle$ of the substrate survives for the following reason: if one compares the interatomic distances of the natural fcc-lattice in the $\langle 211 \rangle$ -direction of that (fcc) film material with the interatomic distances in the $\langle 110 \rangle$ or $\langle 1\bar{1}0 \rangle$ directions of the (bcc) substrate surface, one notices that the misfit perpendicular to these directions is considerably smaller. This applies as well to the (actually identical) interatomic distances in the $\langle 1\bar{1}00 \rangle$ -direction of a conceivable hcp-lattice of the same film material if one retains the interatomic distances of its fcc-lattice. The 3rd ML responds to the competing effect of a large misfit along the alternative directions $\langle 110 \rangle$ and $\langle 1\bar{1}0 \rangle$ and a small misfit perpendicular to these directions by forming a set of parallel atomic rows with a well defined periodicity in the respective directions of a small misfit and by dispensing with a regular distance of these rows. This is because adjacent atoms of neighbouring rows try to compromise on getting close to their natural atomic distance orthogonal to the atomic chains and simultaneously optimizing the energy gain by bonding to the atoms of the 2nd layer underneath. The alternative of forming sets of parallel rows

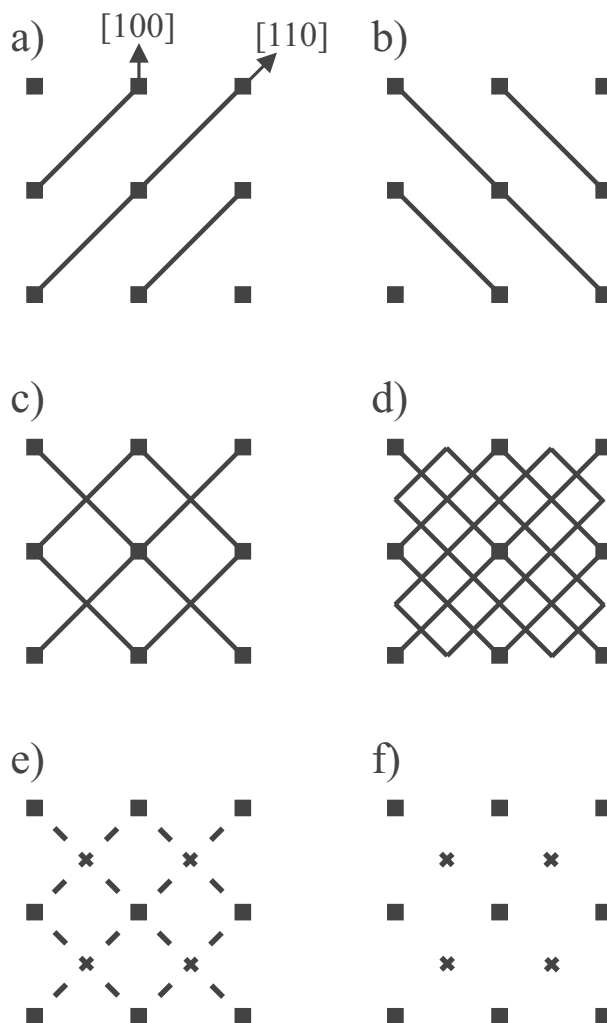


Figure 4.25: Surface reciprocal lattice observed in RHEED reflection from flat surfaces: Black squares correspond to the (1×1) reciprocal lattice of a pseudomorphic layer of adatoms. These streaks may be associated with rods in the 3d-continuation of the surface reciprocal lattice. They are perpendicular to the surface, and their lines reflect the absence of periodicity in that direction. The cases a,b,c) refer to the situation when the rods are elongated in the $\langle 110 \rangle$ direction, that is, when a periodicity in this direction has ceased to exist. In a 3d-continuation of that structure in the reciprocal 2d-lattice they correspond to walls (sheets) which contain the $\langle 110 \rangle$ direction. They may be associated with one-dimensional disorder along this direction. Because of the four-fold symmetry of the (001) surface, there are two sets of walls (a,b). One set is connected with the $[110]$ -direction (a), the other one with the $[1\bar{1}0]$ direction (b). Panel (c) is just a superposition of (a) and (b). The lines one observes with annealed Au films are shown in panel (d). The streaks and extra dots that are schematically indicated in panel (e) and (f) come about by gradually discretizing the walls of panel (a,b,c) so that one ends up with walls of a finite length along the $\langle 110 \rangle$ -direction. The associated structures in the reciprocal surface lattice are a centred $p(2\sqrt{2} \times \sqrt{2})R45^\circ \oplus p(\sqrt{2} \times 2\sqrt{2})R45^\circ$ structure (e) and a $c(2 \times 2)$ ($p(\sqrt{2} \times \sqrt{2})R45^\circ$) structure (f) which one observes with thin films of Pd (e) and with thin Cu and Ag films (f), respectively.

perpendicular to $\langle 110 \rangle$ or $\langle 1\bar{1}0 \rangle$ gives rise to the occurrence of two corresponding types of domains in real space.

All this is confirmed to the fullest by scanning tunneling microscopy (STM) on samples that are associated with RHEED-patterns of this kind (e.g. see the Fig.9,10,11 in Stalder et al. [41] and the figures in Dulot et al. [70]).

4.1.3 Centered diffraction pattern

As may be expected from the picture we have painted above, beyond the 3rd layer the energy optimization drives the atoms of the film into taking their natural lattice sites, as a consequence of which periodicity builds up in these directions orthogonal to the chains where one formerly had disorder for 3 ML. This process transforms into a break-up of the continuous lines into streaks as shown in fig.4.25. For Pd films on W(001) thicker than 6 ML and for Pd films on Nb(001) thicker than 8 ML, the streaks are associated with a surface structure $p(2\sqrt{2} \times 2)R45^\circ \oplus p(2 \times 2\sqrt{2})R45^\circ$ (s. Fig.4.25e). For Ag and Cu films on Nb(001) and for Pd films on Nb(001) with a film thickness in between 3 ML and 8 MLs, the break up of the RHEED-lines produces a centred $c(2 \times 2)$ surface pattern, in the Wulf-notation: $p(2 \times 2)R45^\circ$ (s. fig.4.25f). All these films were deposited at 150 K. The $c(2 \times 2)$ and the $p(2\sqrt{2} \times 2)R45^\circ \oplus p(2 \times 2\sqrt{2})R45^\circ$ pattern becomes sharper when the samples of Cu or Ag are gently annealed up to 400K or up to 500K in the case of Pd-films. One is hence led to conclude that annealing improves the perfection of these surface structures and enlarges their lateral extension. It also enhances the long range order, in the case of Au on Nb(001) in films of thicknesses up to 25 ML's. This is reflected in an even more structured RHEED pattern like that shown in fig.4.25d. If one continues the deposition (generally at 150 K) the films turn rough. With films of Cu or Ag this happens at 10 ML's. For Pd it takes 12 ML's, and in the case of Au 25 ML's. Accordingly, the RHEED patterns gradually attain the typical 3d-type centred structure, s. e. g. Fig.4.24b. On annealing thick Pd films on W(001) the associated RHEED patterns develop a 4-fold periodicity involving every second row of the transmission patterns (see Fig.10 of reference [11]). The reciprocal structures connected with centred RHEED patterns of this kind were also observed in LEED studies dealing with Ni-films on Fe(001) [71], Pd on W(001) [67] and in RHEED studies of Ni- and Cu-films on Fe(001) and on Au(001) [72]. However, the corresponding real-space lattice structure could as yet not be identified. Wang et al. [71] base their explanation on a strained (001)-oriented, body centred tetragonal structure, as opposed to Prigge et al. [67] who discuss a distorted (111) orientation of the fcc structure [67]. Nevertheless, none of these authors could explain the actually observed centred diffraction patterns. Another attempt focuses on the possible existence of a strain structure, stabilised by the substrate (s. [71, 72]). To clarify the implications of a strain structure in terms of centred RHEED patterns, one needs additional information about the local atomic environment in the respective film. X-ray photo-electron diffraction (XPD) provides the appropriate tool for an analysis of this kind. This will be the subject of the ensuing section.

4.2 Diffraction of secondary electrons (XPD)

As already discussed in Section 2.2.4 the technique of X-ray photo-electron diffraction or Auger-electron diffraction [53, 54, 55] exploits the forward-focusing of fast photo- or Auger-electrons along atomic rows on their way toward the surface. The kinetic energy of the outgoing electrons is typically above 300 eV. The forward focusing effect causes a pronounced angle-dependence of the photo- or Auger-electron current density which highlights the angle positions of the closely packed atomic chains with respect to the atomic source. It turns out that, the faster the electrons and the denser the atomic rows, the stronger the corresponding current density modulation.

Fig.4.26a refers to the XPS photo-electron current from Pd-films and shows its dependence on the polar-angle θ . The photo-electrons are associated with a 3d-core level excitation of Pd. The plane

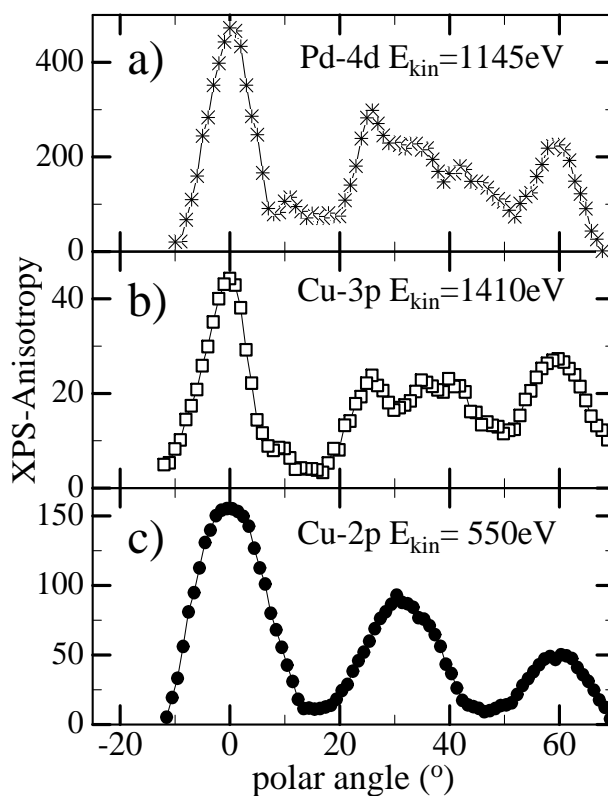


Figure 4.26: Angle-dependence of the X-ray photo-electron current (background corrected). The photo-electrons originate from a core-level excitation through X-ray absorption from an Al $K\alpha$ source which amounts to a photon energy of 1486.6 eV. The curves shown refer to: a) emission from a Pd film of 16 ML thickness deposited on Nb(001); b) and c) from a 16 ML Cu-film on Nb(001). The latter two curves relate to photo-electron currents that result from, respectively, Cu-3p and Cu-2p core level excitation whereas curve a) is associated with Pd-3d core level excitation which results in a kinetic energy of the photo-electrons of ≈ 1145 eV. The kinetic energy of the photo-electrons leaving the Cu-films is, respectively, 1410 eV and 550 eV.

in which the current is monitored contains the high symmetry direction $[110]_{\text{Nb}}$. This is also the direction of the incident beam which the centered transmission RHEED-pattern of Fig.4.21b refers to. An analogous θ -dependence of the photo-electron current was also determined for thin Cu films deposited on Nb(001). Here the photo-electrons are connected with a 3p- and 2p- core level excitation of Cu, respectively (Fig.4.26b,c). These Cu films show the same centered RHEED-pattern as Pd on Nb(001) (Fig.4.21b).

So far we have merely used the qualitative forward scattering argument to interpret the experimental XPD-curves. One gains access to a more quantitative information by doing a multi-scattering calculation on the spherical wave that is emitted from a particular atom after the absorption of an X-ray photon and the concomitant depletion of a 3d (or 2p- or 3p-) core state. A fully dynamical calculation has been carried out by Lo et al. [73] who also performed measurements of XPD-curves on a clean Nb(001) sample. The calculations confirmed the qualitative interpretation to a certain degree, but they provide additional information on multi-scattering effects which cause the occurrence of further peaks or modifications of single-scattering forward focusing peaks.

This becomes obvious from a comparison of two XPD-curves obtained from the same Cu-film. They differ only in the kinetic energy of the outgoing photo-electrons. The first curve shown in Fig.4.26b refers to photo-electrons of 1100 eV kinetic energy associated with a Cu 3p-core level excitation, the second curve, Fig.4.26c, relates to photo-electrons of 600 eV which originate from a Cu 2p-core level

excitation. One observes that the positions of the peaks between $\theta = 20^\circ$ and $\theta = 43^\circ$ are changed as the kinetic energy of the electrons increases. This is indicative of contributions from second order interferences synonymous with multi-scattering effects. By contrast, the peaks at $\theta = 0^\circ$ and $\theta \sim 60^\circ$ are strongly dominated by forward focusing along closely packed atomic chains.

All in all the XPD-results are consistent with the assumption that there is an atomic (Pd- or Cu-) plane of sixfold symmetry in the detector plane spanned by the surface normal and the $[110]_{\text{Nb}}$ -direction. One may conclude then that these atomic planes are close-packed and hence represent building blocks of the natural fcc-lattice of these metals with a stacking axis in the $[1\bar{1}0]_{\text{Nb}}$ -direction. This seems to be confirmed by XPD-plots on (110)-oriented single crystals of Cu where the detector plane was spanned by the surface normal and the $\langle 211 \rangle$ -direction. The result (curve $\varphi = 55^\circ$ in Fig.5 of Ref. [74]) is, in fact, very similar to that shown in Fig.4.26. But the latter also agrees quite satisfactorily with the XPD-results obtained from (110)-oriented hcp-crystals like Co [75]. That means: by using the XPD-technique one is obviously not able to distinguish between an fcc-, hcp- or dhcp stacking of the grown close-packed atomic planes. All this is summarized in Fig.1.2 and in Fig.4.27 which illustrates the respective relations between lattice orientation and the stacking axes for fcc-stacking of a film with fcc(110) orientation (panels (a,c,f) of Fig.1.2 and panels (a,b,c,d) of Fig.4.27) and of films with an hcp- (panels (a,b,e) of Fig.1.2 and panels (a,b,e,f) of Fig.4.27) or dhcp-stacking (panels (a,d,g) of Fig.1.2 and panels (a,b,g,h) of Fig.4.27).

Only the RHEED transmission and reflection technique will prove to yield the information that is necessary to uniquely decide whether the stacking sequence of the films is face-centered cubic or hexagonal (hcp or dhcp). In the latter case one would have demonstrated, and this is the very objective of the present study, that films of a natural fcc-structure are forced into the $(11\bar{2}0)$ oriented hexagonal phase modification if they are grown on a suitable (001) oriented cubic substrate.

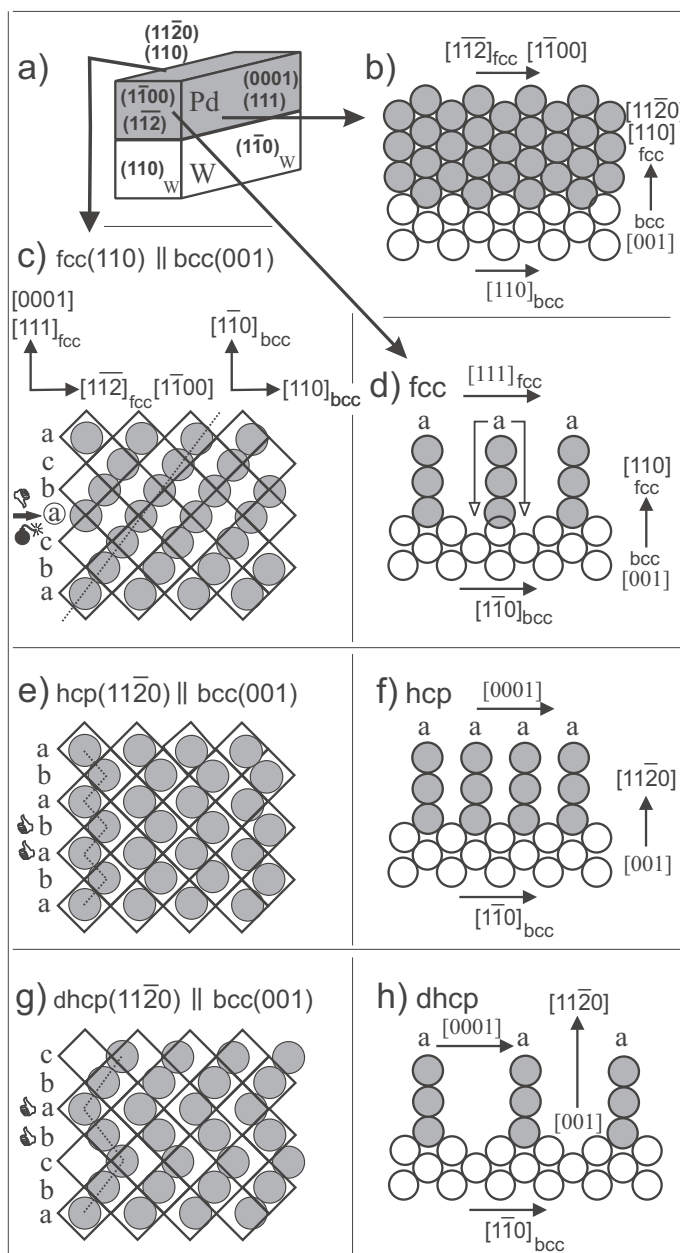


Figure 4.27: a) Possible stackings of atomic planes for (110) oriented Pd on W(001). Epitaxial relations for fcc-stacking (a,b,c,d) are $\text{Pd}(110) \langle 211 \rangle \parallel \text{W}(001) \langle 110 \rangle$. The same for hcp (a,b,e,f) and dhcp (a,b,g,h) stacking: $\text{Pd}(11\bar{2}0) \langle 1\bar{1}00 \rangle \parallel \text{W}(001) \langle 110 \rangle$. Panels (c,e,g) illustrate the fit of the Pd (110) plane for fcc (c), hcp (e) and dhcp (g) stacking to the (001) surface of the substrate. Pd atoms are marked by grey circles. W atoms occupy the corners of the quadratic (001)-lattice indicated schematically. Panels (b,d,f,h) show planar cuts perpendicular to the surface and along the $\langle 110 \rangle_W$ direction of the substrate. The substrate atoms are drawn with open circles. d),f),h) are along the stacking axis, showing the fit of the periodicity of the stacking with respect to W.

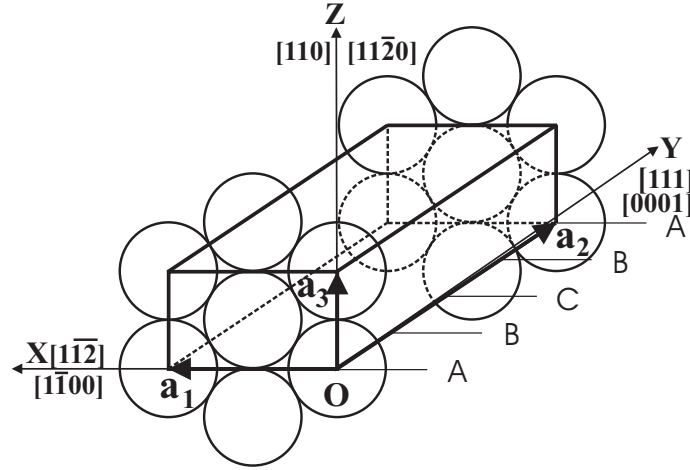


Figure 5.28: The orthorhombic unit cell with a (110) basis is spanned by the vectors \mathbf{a}_1 , \mathbf{a}_2 , \mathbf{a}_3 which coincide with the unit vectors of a Cartesian coordinate system whose coordinate axes run through the centers of atomic rows along the directions $[110]$ ($[11\bar{2}0]$), $[111]$ ($[0001]$) and $\langle 211 \rangle$ ($[1\bar{1}00]$), respectively. These vectors connect neighbouring atoms in the associated rows. The letters A,B,C denote the position of the close-packed planes. The figure shows a dhcp stacking.

5 Analysis and interpretation of the observed patterns

5.1 RHEED transmission

For a comparison of the expected RHEED patterns it is convenient to introduce orthogonal non-conventional unit cells with top and bottom faces that are portions of the (110) planes. Figure 5.28 shows the (110)-based orthorhombic unit cell delimited by two close-packed planes. The first of these planes coinciding with the OXZ-plane. The distance a_2 is given by the stacking sequence periodicity of the close-packed phases.

The (110)-based unit cell is spanned by the vectors: $\mathbf{a}_1 = a\sqrt{3}\mathbf{e}_1$, $\mathbf{a}_2 = c\mathbf{e}_2$ and $\mathbf{a}_3 = a\mathbf{e}_3$, where $\mathbf{e}_1, \mathbf{e}_2, \mathbf{e}_3$ are the unit vectors of the Cartesian coordinate system, a is the atomic nearest-neighbour distance in the fcc film. c is aligned parallel to the stacking direction which is the $[111]$ -direction for an fcc-structure and the $[0001]$ -direction for hcp- or dhcp-structures. Its value is equal to the distance between close-packed planes possessing equivalent stacking positions. For the hcp-, fcc- and dhcp-stacking sequence we have $c = 2 \cdot (a \cdot \sqrt{2/3})$, $c = 3 \cdot (a \cdot \sqrt{2/3})$ and $c = 4 \cdot (a \cdot \sqrt{2/3})$, respectively, where $(a \cdot \sqrt{2/3})$ is the interlayer distance between consecutive close-packed planes. For a random stacking we have $c \rightarrow \infty$.

Figs.5.29,5.30,5.31, 5.32 display the reciprocal lattices constructed from these unit cells. The figures refer to the stacking mode with a periodicity of two, three and four close-packed planes, and to the case of a random stacking mode. The reciprocal orthorhombic unit cells are spanned by the vectors $\mathbf{b}_1, \mathbf{b}_2, \mathbf{b}_3$, with $\mathbf{b}_1 = (2\pi/(a\sqrt{3}))\mathbf{k}_x$, $\mathbf{b}_2 = (2\pi/c)\mathbf{k}_y$ and $\mathbf{b}_3 = (2\pi/a)\mathbf{k}_z$, where $\mathbf{k}_x, \mathbf{k}_y, \mathbf{k}_z$ are the unit vectors of the Cartesian coordinate system with $\mathbf{k}_x \parallel \mathbf{e}_1$, $\mathbf{k}_y \parallel \mathbf{e}_2$ and $\mathbf{k}_z \parallel \mathbf{e}_3$. These reciprocal lattices are independent of the atomic array inside the unit cell. The position of these atoms leads to a systematic extinction of diffraction spots and are marked by open circles.

Because of the large extent of the Ewald sphere it can be approximated by a plane within the opening angle of the monitored diffracted beams. Hence, a RHEED transmission pattern corresponds to a planar cut through the reciprocal lattice with the plane being perpendicular to the primary beam. Of course, ideally points of the reciprocal lattice can only accidentally coincide with the Ewald

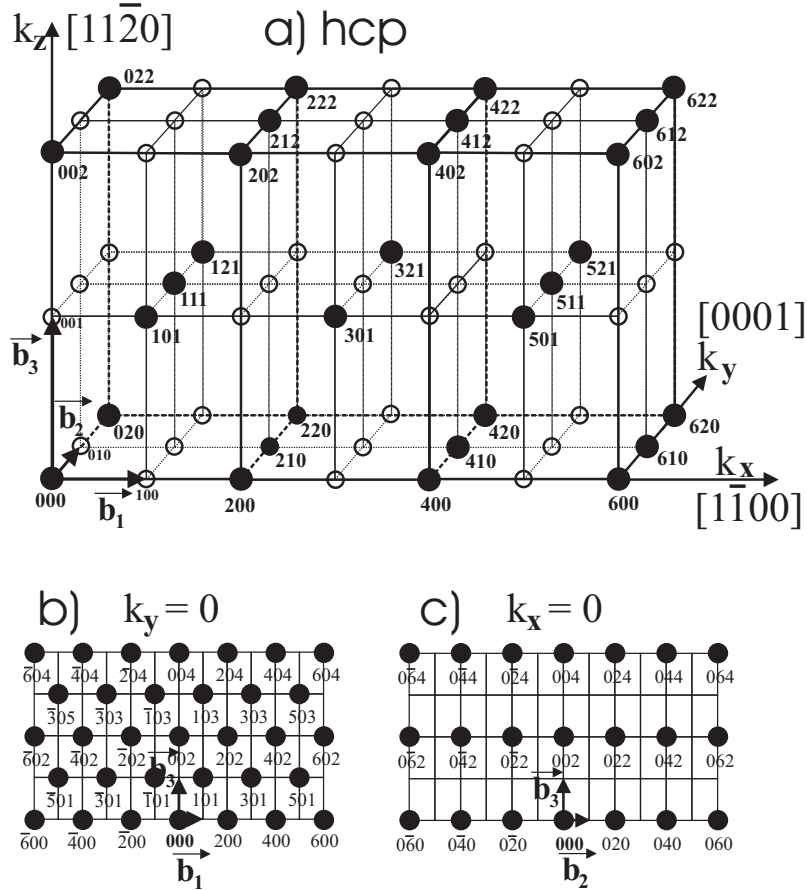


Figure 5.29: a) The reciprocal lattice for the case of hcp stacking constructed from the orthorhombic (110) -based unit cell given in Fig.5.28. The structure factor which controls the relative intensities of the diffraction beams and depends on the array of the atoms inside the unit cell, leads to a systematic extinction of certain spots that correspond to lattice points marked by open circles. Lattice points that appear through constructive interference as diffraction spots are marked by full circles. b,c) refer to portions of the planes (0001) (b) and $(1\bar{1}00)$ (c) which correspond to the $(k_y = 0)$ plane and to the $(k_x = 0)$ -plane, respectively. Only lattice points that lead to diffraction spots are drawn. The scale in (b,c) is reduced by a factor of 4 compared to that in (a). The lines in the direction of the reciprocal vectors $\mathbf{b}_1, \mathbf{b}_2, \mathbf{b}_3$ are only guides for the eye.

sphere (plane). But because of the limited long range order within the microcrystals sampled by the incoming RHEED beam and because of its inevitable slight non-collinearity the reciprocal lattice points blow virtually up to form blurred spheres and the Ewald sphere itself becomes slightly smeared out. As a result, all points of the reciprocal lattice which are originally only close to the ideal Ewald sphere and lie within the monitored range of the detection plane become visible.

As opposed to the (001) -substrate surface which displays a four-fold symmetry with respect to the surface normal, the symmetry of the $(110)_{film}$ and $(1\bar{1}20)_{film}$ surfaces is only two-fold.

The $[110]$ -direction of the (001) -surface of a bcc-substrate and the orthogonal $[1\bar{1}0]$ -direction are equivalent. This applies similarly to the mutually orthogonal $[010]$ - and $[100]$ -directions of the (001) -surface of an fcc-substrate. By contrast, the orthogonal directions $[0001]_{film}$ and $[1\bar{1}00]_{film}$ or $[111]_{film}$ and $[1\bar{1}2]_{film}$ are not equivalent. Therefore, the film grows on the (001) -surface of a cubic substrate by forming two sets of domains with a mutually orthogonal striped pattern. In the case of a non-fcc stacking one domain has its $[0001]_{film}$ -direction parallel to the $[110]$ -direction of the bcc-substrate and the $[1\bar{1}00]_{film}$ -direction parallel to the $[1\bar{1}0]$ -direction of the substrate. The other

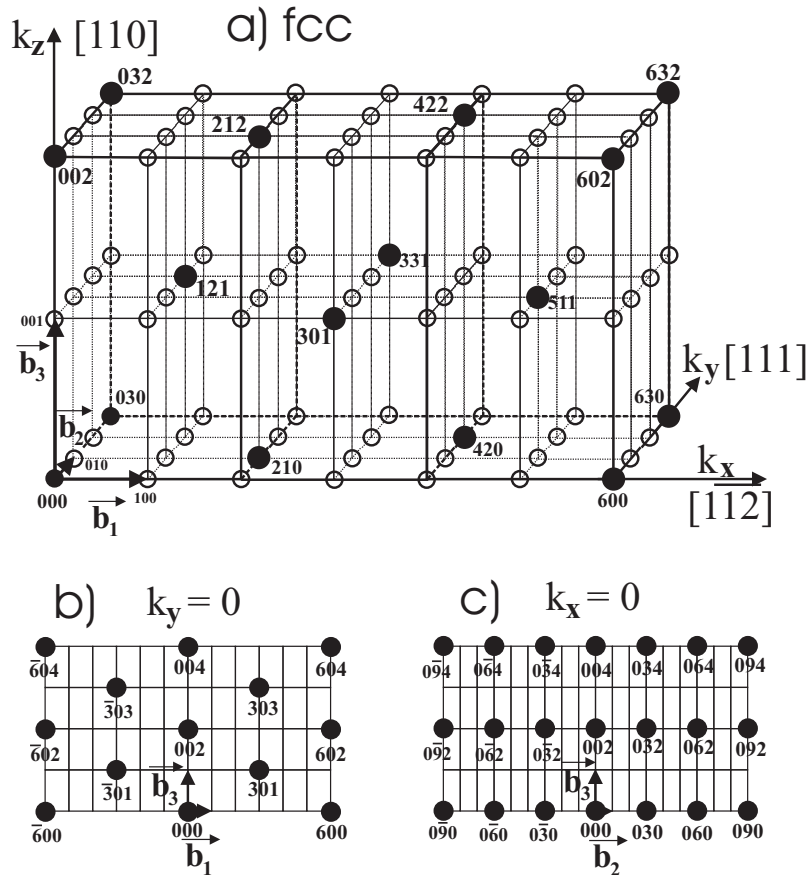


Figure 5.30: The same as in Fig.5.29, but now for fcc stacking (ABCABC). Note that all lattice points for which the structure factor does not vanish (all full circles) form a bcc lattice which represents the reciprocal lattice of an fcc crystal.

domain is oriented such that the $[0001]_{film}$ -direction is parallel to the $[1\bar{1}0]$ -direction of the substrate and the $[1\bar{1}00]_{film}$ -direction parallel to the $[110]$ -direction of the substrate.

If fcc-stacking occurs (s. Fig.4.27) the above statements apply similarly, but the $[211]_{film}$ -direction stands now in place of the $[1\bar{1}00]_{film}$ and $[0001]_{film}$ has to be replaced with $[111]_{film}$.

How is this reflected in the structure of the RHEED transmission pattern?

It is suggestive to use three different directions of the incident beam: 1) parallel to the $[110]$ -direction, 2) parallel to the $[1\bar{1}00]$ -direction and 3) parallel to the $[0001]$ -direction.

In the first case the beam grazes along $[1\bar{1}00]$ -direction and, because of the presence of two sets of orthogonal domains, along the $[0001]$ -direction as well. Consequently, the associated two RHEED-patterns appear superimposed.

In the second case the RHEED-pattern appears as a map of the (0001) -plane (the k_{yz} -plane) of the reciprocal lattice associated with the hcp- or dhcp-lattice. This plane is perpendicular to the incident beam.

In the third case the direction of the incident beam is perpendicular to the $(1\bar{1}00)$ -plane (the k_{xz} -plane) of the reciprocal hcp- or dhcp-lattice. The observed RHEED-pattern is hence a superposition of the planes $k_x = 0$ and $k_y = 0$ in these reciprocal lattices (s. Fig.5.33 (a,b) and (a,c)). In the case of an fcc-stacking the RHEED-pattern would be a map of the (111) - and $(1\bar{1}\bar{2})$ -plane of the corresponding reciprocal lattice (s. Fig.5.33 (a,d)). As follows from inspection of Fig.5.33 (e,f,g) and comparison with the actually observed RHEED-pattern, the latter conforms obviously only to the hcp-structure

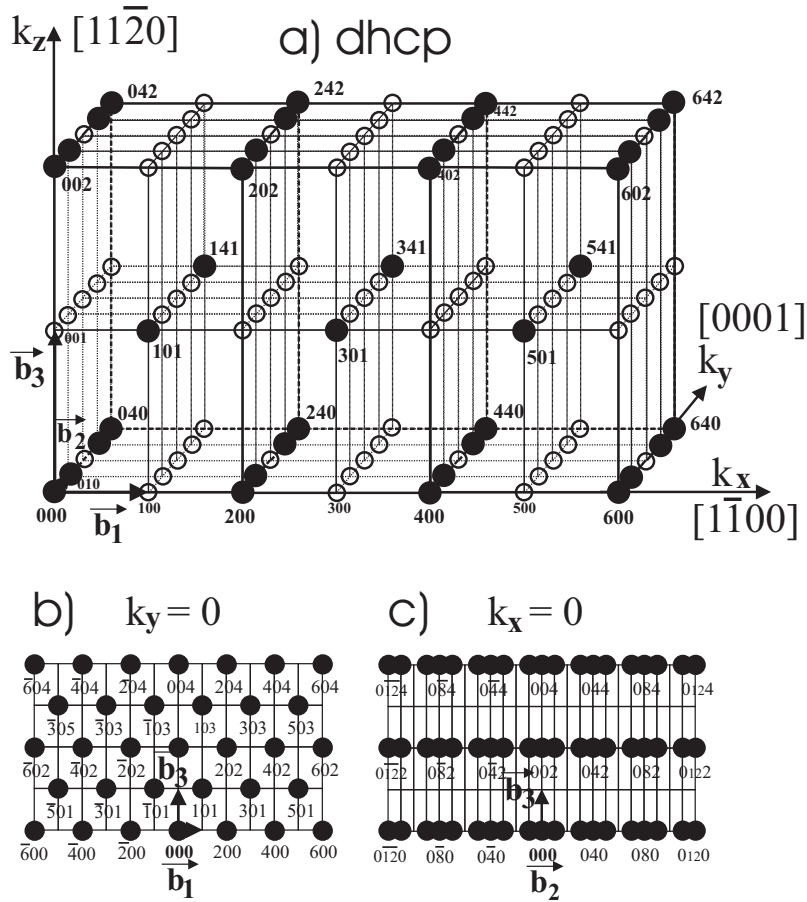


Figure 5.31: The same as in Fig.5.29, but now for dhcp stacking (ABCBA). Note how the lattice points become more numerous along b_2 i. e. in the stacking direction.

of the films.

The reciprocal lattice associated with random stacking deserves particular interest. In this case the (0001) plane (Fig.5.32b) is identical with that of the hcp-structure (Fig.5.29b). This leads to a possible explanation of the observed RHEED transmission pattern (Fig.4.24b) in terms of a close-packed structure that displays one-dimensional glass-type order along the stacking direction. Random stacking would give rise to a similar diffraction pattern as the one that is actually observed (Fig.4.24b) if only the contribution of the ($k_x = 0$) plane (($1\bar{1}00$)-plane) (Fig.5.32c) would not appear. A closer look at the transmission pattern reveals, however, that there is no missing contribution. The distance between the spots is constant within a row and also in every second row, but different when going from one row to the next one. As already mentioned, this is connected with the fact that the RHEED pattern results from a superposition of the $k_x = 0$ and $k_y = 0$ planes which have different horizontal distances between the reciprocal lattice points. The quotient of these two distances should be equal to $(2b_2)/(2b_1) = \sqrt{3}a/(\sqrt{8/3}a) = \sqrt{3}a/c = 1.0607$. Our measurements yield $\sqrt{3}a/c = 1.0372$ for Cu, Rh, Pd, Ag and Au, where from one obtains a c/a value of 1.67. This is slightly larger than the ideal value ($c/a \simeq 1.63$). On summarizing the RHEED information on ad-metal films that are grown on a Nb(001) substrate one is led to conclude that the ad-metal film-lattice constant is by $\sim 1\%$ smaller than that of bulk ad-metal. This ties in nicely with the enlarged c/a value (~ 1.67 instead of 1.63) as a result of which the atomic density of ad-metal is conserved i.e. it keeps its bulk (fcc)-value. Obviously, a larger c/a value yields a unit cell in the ($11\bar{2}0$) plane of the hcp-lattice which is closer to a square and hence fits better onto the square mesh of the (001) surface of the substrate. This brings up the

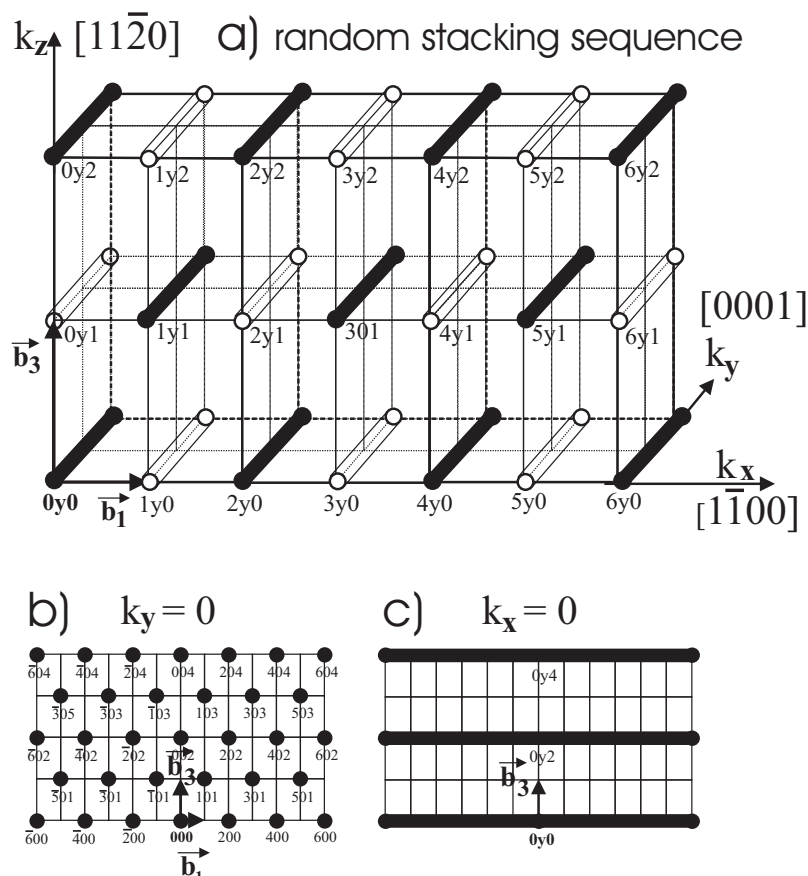


Figure 5.32: The same as in Fig.5.29, but now for random stacking. In this case the reciprocal lattice consists of rods along the stacking direction where a distinct periodicity is missing. Open rods indicate zero structure factor and hence do not appear in the diffraction pattern.

question whether the square unit cell of the substrate induces a larger c/a value of the adsorbate, or whether this larger value is a bulk property of the hcp phase of metals whose natural crystal structure is fcc. First principles calculations on the total energy of hcp Au and Ag have been performed for a set of c/a -values under the constraint that the atomic density be conserved [33]. The total energy attains a minimum at $c/a=1.67$, and in a similar calculation for Pd [76] one obtains $c/a=1.68$, both values being slightly larger than the ideal value $\simeq 1.63$. This supports the interpretation that the observed larger c/a -values reflect, in fact, a bulk property and are not caused exclusively by epitaxial stress in the hcp-films. Nevertheless, the growth of the films in a hcp non-equilibrium structure is governed by minimizing the misfit energy with respect to the first pseudomorphic layers on the (001) substrate. It certainly helps stabilizing these films that the bulk controlled c/a -enhancement leads simultaneously to a better fit to the square mesh of the (001) surface.

5.2 Analysing TED data

On inspection of the reciprocal lattices associated with the various stacking modes (figs.5.29, 5.30, 5.31, 5.32), one notices that not only the $k_x = 0$ - and $k_y = 0$ -planes (needed to explain the RHEED-transmission patterns) but also the $k_z = 0$ plane can be important if one wants to distinguish between the various stacking modes. The $k_z = 0$ plane can provide the sought-for information by way of the transmission pattern if the electron beam is normal to the surface. This is exactly the beam geometry in transmission electron diffraction (TED) by means of which Bruce and Jaeger [77, 78, 79] studied

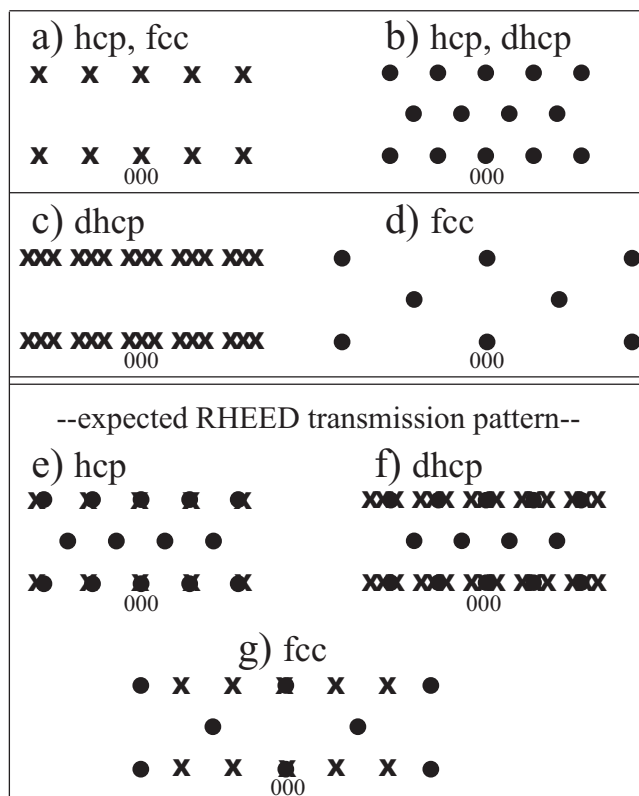


Figure 5.33: a) The $(1\bar{1}00)$ -plane cut through the reciprocal structure of the hcp lattice which is identical with the $(1\bar{1}\bar{2})$ -plane cut through the reciprocal structure of the fcc-lattice. b) The (0001) -plane cut through the reciprocal structure of the hcp- and dhcp-lattice. c) The $(1\bar{1}00)$ -plane cut through the reciprocal structure of the dhcp-lattice. d) The (111) -plane cut through the reciprocal structure of the fcc-lattice. e) The expected RHEED-transmission pattern from an hcp-stacking sequence is a superposition of panels (a) and (b). f) The expected RHEED pattern for a dhcp stacking sequence is a superposition of panels (c) and (b). g) The expected RHEED-pattern for a fcc stacking sequence is a superposition of panels (a) and (d).

the structure of relatively thick films grown on W(001) and Mo(001). (These authors also investigated Ni and Cu on Ag(001).)

Figure 5.34 shows the $k_z = 0$ plane in the case of fcc-stacking (panels (a,b,c,d,g)), of hcp-stacking (panels (e,h)) and dhcp-stacking (panels f,i)). Because of the 4-fold symmetry of the (001) substrate surface, there are four possibilities to align the stacking axis along the $\langle 110 \rangle$ surface direction of the bcc(001) substrate. This is shown in Fig.5.34a,b,c,d for fcc-stacking. The expected TED patterns are a superposition of the resulting four arrays. The transmission patterns for fcc-, hcp- and dhcp-stacking are given in figs.5.34g, h, i, respectively. We can compare them with the transmission patterns obtained by Bruce and Jaeger for Ni, Cu, Rh, Pd, Ag, Ir, Pt, and Au on W(001) and on Mo(001) (also Ni and Cu on Ag(001)). We observe that for thick films of Ni, Cu, Rh, Pd, Ir, Pt on W(001) and Mo(001) the film structure is $(11\bar{2}0)$ -oriented hcp if the substrate is kept at an elevated temperature during the film deposition. At low deposition temperatures the adsorbate stacks in the fcc-mode, which is surprising. One would rather expect that a deposition at low temperature favors the stabilization of metastable phases [80]. We surmised that this unexpected behavior in the experiments by Bruce and Jaeger was caused by carbon impurities on the W and Mo substrate surfaces. They kept their substrate temperature $\leq 700K$ during the film growth. We have performed a detailed study on the various experimental conditions that influence the film growth. It turned out that, independent of the deposition temperature, the hcp phase always appear if the metallic substrates are free from

impurities (like S, C and O). If, however, the (001) adsorption sites of the substrate are occupied or destroyed by impurities like sulfur [12], oxygen or carbon [18, 19], films with hcp-structure cannot grow. An important point of the present work consists in the observation that W as a substrate material has to be heated substantially under oxygen partial pressure to remove C from the bulk. Only in this way one can exclude the possibility of a carbon migration to the surface in the process of cooling the samples down to the envisaged experimental conditions. (Heating the samples is often necessary, for example, if one wants to completely remove the adsorbate for another growth study). Bruce and Jaeger did not go through that inevitable preparatory procedure and, in addition, their setup was not equipped with AES as an indispensable and exceedingly surface sensitive tool that allows one to check the cleanness of the substrate surface in detail. Hence, it may safely be concluded that Bruce and Jaeger did not obtain the hcp modifications at low temperature deposition because their W and Mo substrates were contaminated by carbon. At high temperature deposition they obviously succeeded in growing hcp films which has a simple explanation: it is well known that, at high temperatures (700K), C dissolves again in the bulk of W or Mo, or agglomerates at certain places of the surface thereby causing large portions of the W(001) surface to be free from C-contamination [57]. A remarkable byproduct of the experiments by Bruce and Jaeger may be seen in the observation that the deposited films of Ni, Cu, Rh, Pd, Ir and Pt retained their hexagonal crystal structure even when they were stripped off the substrates.

5.3 LEED/RHEED reflection

5.3.1 Film orientation

In Fig.4.27 (which was presented in the previous section) we try to summarize the insights we have already gained from the analysis of the previous sections. We have chosen the example of a Pd film that grows on a W(001)-surface. The figure elucidates the reason why the adsorbate films grow in the hexagonal stacking mode. For all stacking modes (including fcc-stacking) the close-packed atomic planes lie perpendicular to the surface and are stacked along the 'diagonal' $\langle 110 \rangle$ direction of the (001) surface of the bcc-substrate (Fig.4.27b) or along the diagonal $\langle 100 \rangle$ direction of the (001) surface if the substrate were an fcc material. If the film would choose an fcc-stacking, the atoms of the close-packed planes that are near to the substrate would be placed into energetically unfavorable adsorption sites (away from hollow sites) (Fig.4.27c) than in the case of a hexagonal stacking mode (Fig.4.27e,g). This is illustrated in panels (d,f,h) where the stacking axis lies in the paper plane and is parallel to the [110] direction of the substrate. One recognizes in panel d) of Fig.4.27 that with fcc-stacking the near-substrate atoms of every second plane (of the ones that are shown) are placed into the most unfavorable 'on-top' position. It is energetically obvious that, in the process of further growth, the atoms of the film will move to the favorable hollow-sites marked by down-arrows in Fig.4.27d. Thereby an array of atoms develops that corresponds to an hcp- or dhcp-stacking (Fig.4.27 f) and h), respectively). The energy difference between 'on-top' and hollow-site positions is particularly sizable if the bonds between substrate and adatoms are metallic. In other words, the most favorable adsorption sites, that display a square geometry force the film into a hexagonal stacking mode. Once the hcp-stacking is initialized by the substrate, the hcp- or dhcp-growth simply continues, because other adsorption places are not available. This mechanism was also observed in epitaxial studies on Co where the (001) surface of W and Au induced a (11 $\bar{2}$ 0) hcp orientation in the growth of a Co-film: (S. [11, 81] and [82, 83].)

If, however, the film is deposited on the (110)-surface of an fcc-substrate where favorable adsorption sites for an fcc stacking occur, the Co-film grows in an fcc-stacking mode. (S. [84, 85] where an fcc Cu-substrate was used.)

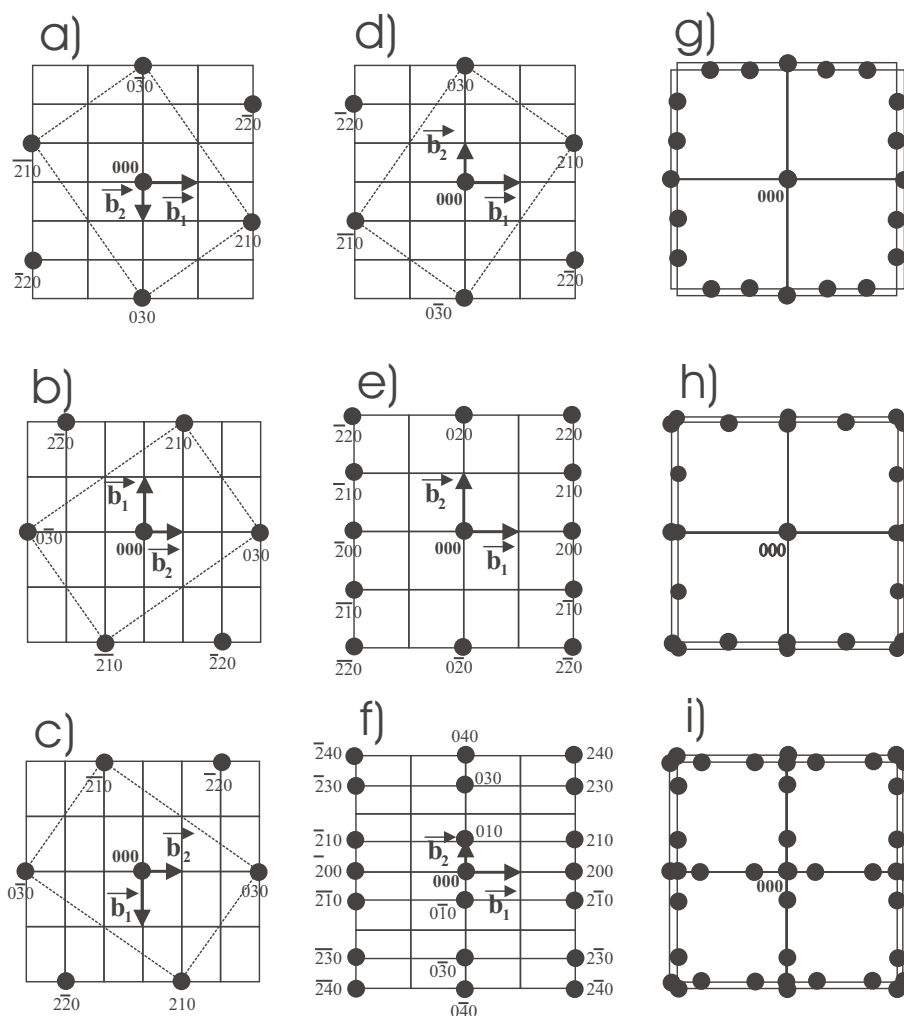


Figure 5.34: The $k_z = 0$ -plane for the fcc-(panels (a,b,c,d,g)), the hcp- (e,h) and the dhcp- (f,i) stacking mode. The 4-fold symmetry of the (001)substrate surface leads to the growth of equivalent adsorbate domains which differ only in that their stacking axes (parallel to \vec{b}_2) is rotated by 90° with respect to each other. Their $k_z = 0$ -planes are also rotated by 90 degrees relative to each other. For fcc-stacking this is depicted in panels (a,b,c,d). The expected TED pattern will therefore appear as a superposition of four patterns that are associated with the $k_z = 0$ -plane. Each of these patterns belongs to one domain out of the four. This is illustrated in panel (g) for the fcc-, in panel (h) for hcp- and in panel (i) for dhcp-stacking. In panels (a,b,c,d,e,f) we have labeled some points of the bulk reciprocal lattice. The thin lines characterize the unit cell in the $k_z = 0$ -plane of the 3-dimensional reciprocal lattice. The lines in panels (g,h,i) are only a guide for the eyes.

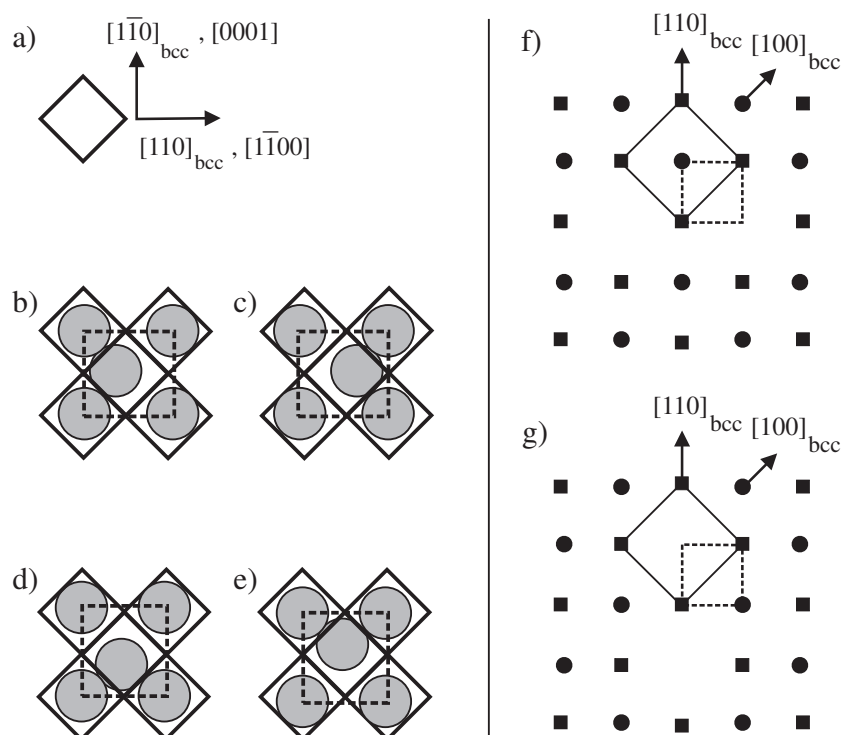


Figure 5.35: a) Primitive unit cell of a (001) substrate e. g. W(001). The substrate atoms occupy the corners of the quadratic unit cell shown.

b),c),d),e) unit cells of a $(11\bar{2}0)$ hcp-surface. It is apparent that there are four options for ordering the film atoms such that they yield an optimal fit to the atomic square array of the substrate. The atomic arrays of the cases b) and c) give rise to the 2-dimensional reciprocal lattice f), those of the cases d) and e) correlate with the reciprocal lattice g). The reciprocal hcp-unit cell within the plane of this lattice is indicated by dashed lines, the unit cell of the substrate by solid lines. Filled squares mark points that are shared with the associated planar cut of the hcp-reciprocal lattice. Missing points indicate that the associated structure factor in the LEED intensity is zero.

5.3.2 Explanation of the centred diffraction patterns of smooth surfaces.

Since Pd and Cu possess fcc-equilibrium structure, one would expect that they transform from an initially pseudomorphic structure into the respective equilibrium (fcc) lattice when they are deposited on Nb(001) and W(001). The same can be said as to the case of Ni growing on Fe(001) [71]. But the the observed centred $c(2 \times 2)$ and $(2\sqrt{2} \times \sqrt{2})R45^\circ \oplus (\sqrt{2} \times 2\sqrt{2})R45^\circ$ patterns clearly invalidate a simple explanation of this kind. Only if one allows for a hexagonal stacking with the stacking axis perpendicular to the surface-normal these centred diffraction patterns (see panels (e,f) of Fig.4.25) can consistently be explained.

In the Figures 5.37,5.38,5.39 we demonstrate that a conceivable fcc(110) orientation of the films fails to explain the observed centred diffraction pattern even when the stacking axis is aligned along a particular direction which appears in each domain out of four equivalent orthogonal domains that occur equivalently because of the 4-fold symmetry of the (001)- substrate surface. By contrast, the hexagonal close-packed film structures (see the Figures 5.35,5.35 and 5.39) explain the diffraction data with remarkable consistency. In summarizing one can say that the strain centred (reflection and transmission) diffraction patterns that are observed in many late transition metal films, grown on open (001)-substrates, are connected with a hexagonal close-packed structure of the adsorbate films. These films display a $(11\bar{2}0)$ orientation.

As we have abundantly demonstrated, the observed centred diffraction pattern cannot be interpreted

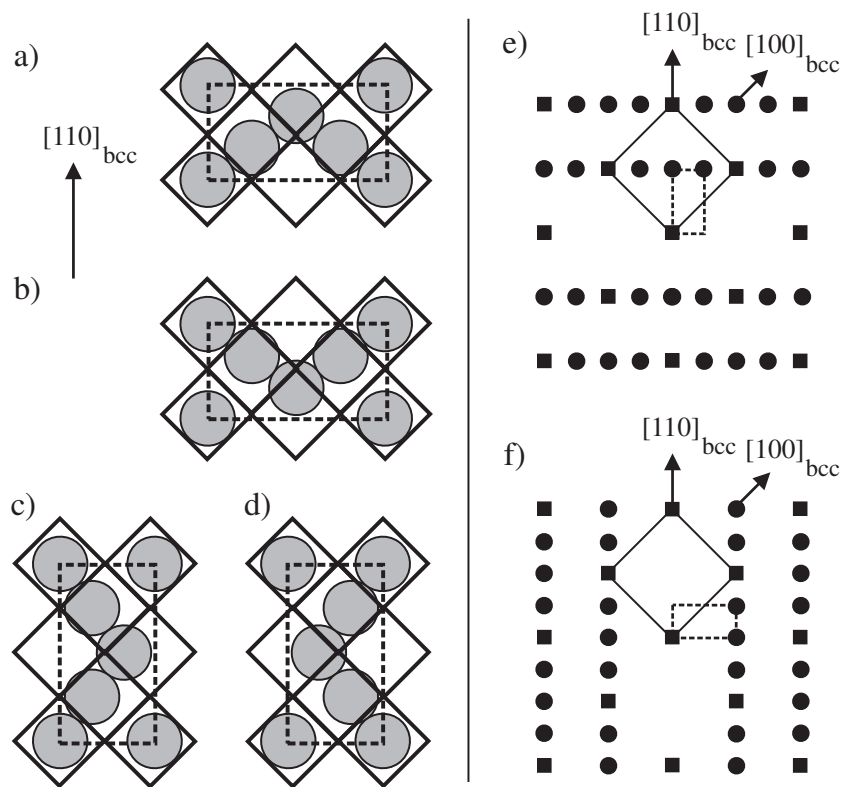


Figure 5.36: The dhcp-analogue of Fig.5.35: a),b),c),d) unit cells of a $(11\bar{2}0)$ dhcp-surface. Obviously, there are again four options for an optimal fit of the film atoms to the square lattice of the substrate.
 e) Reciprocal lattice corresponding to the arrays a) and b). f) reciprocal lattice corresponding to the arrays c) and d). The meaning of the lines and the missing points is as in Fig.5.35.

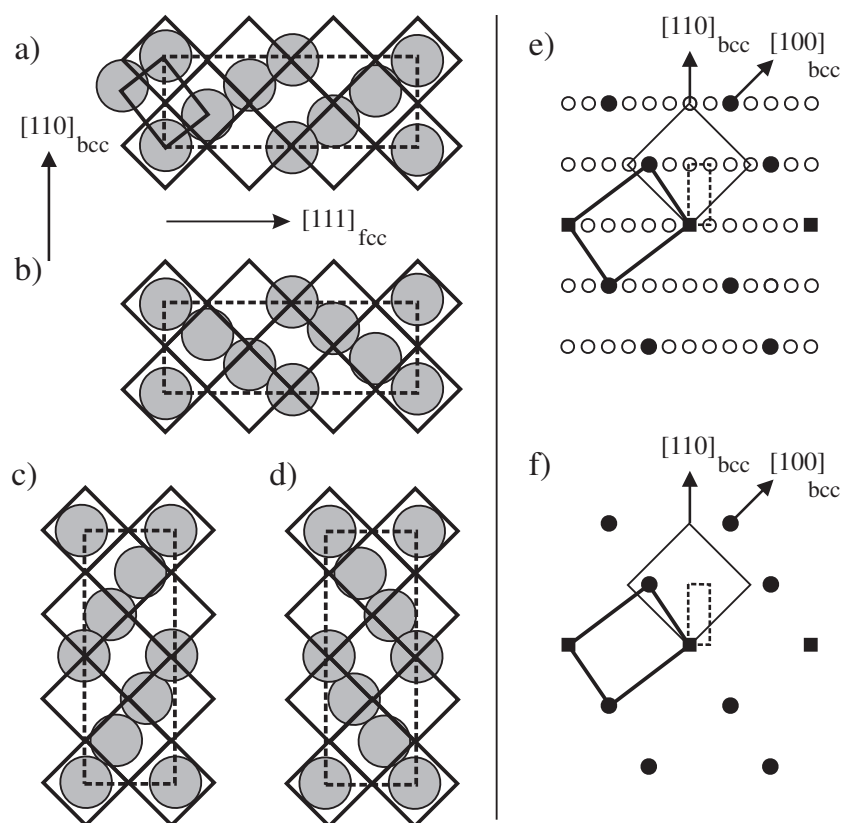


Figure 5.37: The fcc-analogue of Fig.5.35: a),b),c),d) unit cells of a (110) fcc-surface. The primitive cells are characterized by solid lines, non-primitive cells, that is lattice cells with a basis, are marked by dashed lines. Their equivalents in the reciprocal lattice are characterized correspondingly. As becomes apparent from the drawings, there are again four possible arrays of the film atoms with optimal fit to the (001)-surface of the bcc-substrate. The reciprocal lattice e) is associated with the array a). Open circles mark points of the reciprocal lattice for which the structure factor of the LEED intensity becomes zero. All points shown are associated with the non-primitive fcc-unit cell of the real space lattice. If one leaves out the open circles one obtains chart f) which constitutes for the (110)-surface of the fcc lattice just the 2-dimensional reciprocal lattice.

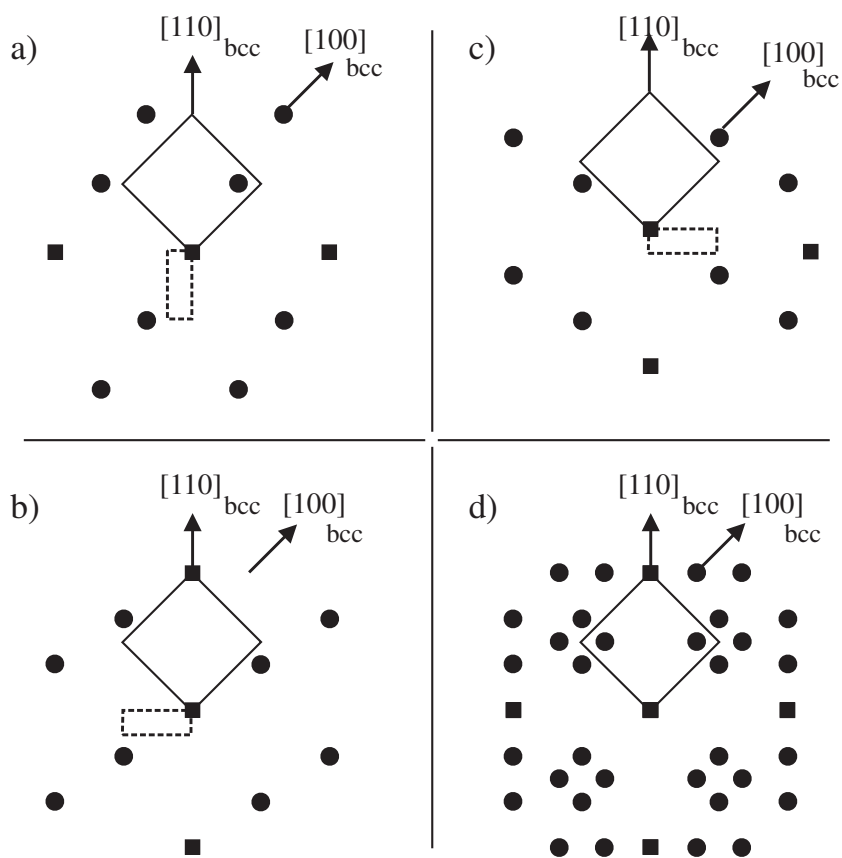


Figure 5.38: 2-dimensional reciprocal lattices a), b) and c) of the atomic arrays shown in the charts b), c) and d), respectively, of Fig.5.37. Chart d) refers to a superposition of these three reciprocal lattices with the reciprocal lattice f) shown in Fig.5.37.

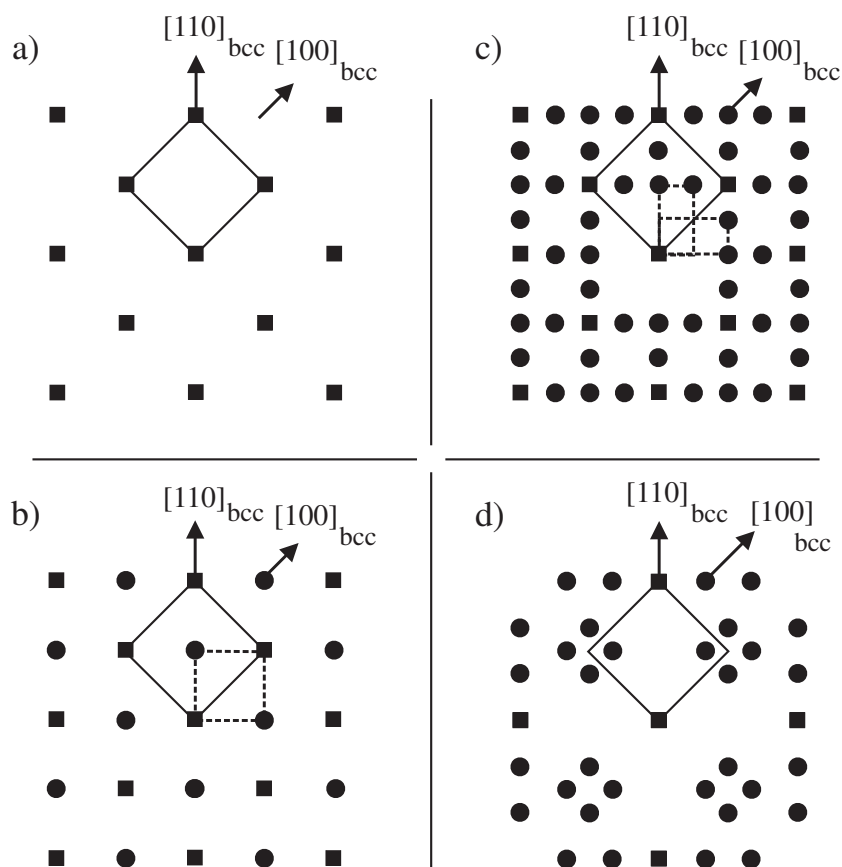


Figure 5.39: Distinguishing structures of grown films by their LEED pattern.

a) LEED pattern of the (001) surface of a bcc substrate. That pattern attains the form b) if the deposited film grows by stacking atomic planes in a hcp-mode perpendicular to the substrate normal. The pattern constitutes a superposition of the charts f) and g) in Fig.5.35 and may be classified as a $c(2 \times 2)$ array of points with respect to the pattern of the clean substrate. In the case of a dhcp-stacking the LEED pattern takes the form shown in chart c) which is a superposition of the charts e) and f) in Fig.5.36. Chart d) refers to the case of an fcc-stacking. The pattern is identical with the chart d) of Fig.5.38.

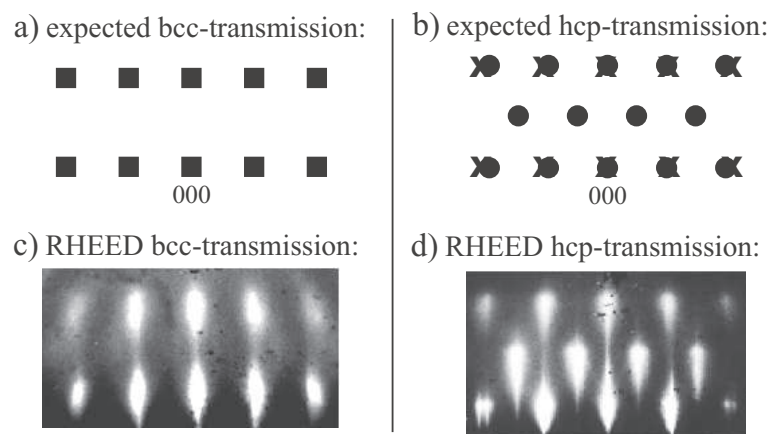


Figure 5.40: Expected (a,b) and measured (c,d) RHEED-transmission patterns with the electron beam coming in parallel to the $\langle 110 \rangle$ -direction of the bcc(001)-surface. The patterns refer to the following cases: a,c) bcc (001)-oriented lattice; b,d) hcp ($11\bar{2}0$)-oriented lattice grown epitaxially on a bcc (001)- substrate as shown in Fig.4.27. Panel (a) shows a cut along the (110)-plane through the reciprocal fcc-lattice of the bcc- (real space) lattice. Panel (b) refers to a superposition of cuts through the reciprocal lattice of a hcp- (real space) lattice. The pattern consists of a cut along the ($1\bar{1}00$)-plane (marked by crosses) and along the (0001)-plane (marked by circles). (See also Fig.5.34c.) To alleviate a comparison, Panel (c) - which is identical with Fig.4.24 - shows again the RHEED-transmission pattern associated with a Nb (001)-substrate. Panel (d) presents the RHEED-transmission pattern obtained from a hcp ($11\bar{2}0$)-Co film of 7 ML thickness grown on W(001) with the same epitaxial relation as in Fig.4.27. This pattern is akin to that presented in Fig.4.24b which has been discussed in the preceding section.

as referring to an fcc-structure of the film. Yet, so far, we have not scrutinized the possibility of a bcc-structure which - upon reconstruction of the surface - can also give rise to a $c(2 \times 2)$ LEED pattern. This has, in fact, been observed with clean W(001) surfaces which reconstruct at low temperatures ($< 300K$) [86, 87]. If we choose the concrete case of a Co-film, the structures of the hcp ($11\bar{2}0$)- and the substrate bcc (001)-surfaces are in fact similar, the former being different from the latter by no more than a small relative shift of the Co atoms in-plane (i.e. parallel to the surface) and by a contraction of about 10% out-of-plane. Notwithstanding this similarity, techniques that have some depth sensitivity allow one to detect whether the atoms of the film below the $c(2 \times 2)$ -ordered surface monolayer occupy hcp- or bcc- lattice sites. Such diffraction techniques are, for example, LEED-IV analysis, X-ray and transmission-RHEED. As the latter is, by definition, depth sensitive it can clearly distinguish between a hcp ($11\bar{2}0$)- and a surface-reconstructed bcc (001)-lattice, as demonstrated in Fig.5.40.

The $c(2 \times 2)$ LEED patterns one observes with Co-films [88] have been studied by the former Clausthal-group of Bauer and associates [11, 88] and shown to be consistent with the centered transmission RHEED patterns that occur after the films develop protrusions that are penetrated by the incident beam (fig.5.40d.) These RHEED patterns could only be correlated with an hcp ($11\bar{2}0$)-phase. That is, the centred RHEED transmission pattern of fig.5.40d is definitely at variance with a bcc (001)- or bct (001)-structure, as has already been discussed in the previous section.

Co films deposited on Mo(001) buffer layers show the same centered RHEED transmission pattern [89]. If one performs X-ray diffraction (XRD) experiments on these films, probing again the bulk structure, the results confirm the existence of a hcp ($11\bar{2}0$)-phase [89].

There is quite a number of further studies focused on the structure of Co-films deposited on W [88, 81] and Cr [90, 91, 92, 89]. Donner et al. [90] point out that the observed centered RHEED streaks (which appear in addition to the (1×1) pattern and thus form, in a more general sense, a

centered pattern) cannot be correlated with any surface reconstruction as these patterns are also observed in X-ray scattering at grazing incidence which ensures a sampling of the entire film. X-ray diffraction studies on these Co films leave no doubt that one is dealing with an hcp ($11\bar{2}0$) - structure [90, 91, 92, 89]. Centered RHEED transmission patterns were also observed with Co films deposited on GaAs(001) [95]. Wu et al. [95] performed transmission electron diffraction (TED) on these films and demonstrated that even with a non-metallic substrate the hcp ($11\bar{2}0$)- orientation prevails in accordance with previous TED results of Gu et al. [96].

Co films on Au(001) and their centered RHEED transmission patterns were studied by Oikawa et al. [82]. A TED analysis of these films by [83] and atom resolved electron microscopy by Bayle-Guillemaud and J. Thibault [83] confirmed again the robustness of the hcp ($11\bar{2}0$)-growth on a substrate that displays a square mesh structure provided that the misfit is sufficiently low.

Recently Wieldraaijer et al. [97] have reported LEED-IV results on Co films deposited on Fe(001). Their energy loss spectra show that once the $c(2 \times 2)$ LEED pattern appears the out-of-plane lattice constant matches that of a hcp-lattice in the $[11\bar{2}0]$ -direction rather than that of a bcc-lattice in the $[001]$ -direction. This important result—which will be analyzed more closely in the ensuing section—shows that the appearance of the $c(2 \times 2)$ LEED-pattern is indicative of the formation of close-packed (0001)-layers perpendicular to the surface rather than of layers that belong to a bcc lattice. A similar LEED study and strain analysis [98] and further experiments that pertain to (001)FeAl-substrates [99] lead to the same conclusion. This applies as well to Cu-films on W(001) which also prove to form a hcp ($11\bar{2}0$)-structure [100].

One can summarize the experimental material by stating:

all depth sensitive diffraction techniques bear evidence that the observed $c(2 \times 2)$ pattern in LEED (or RHEED) for close-packed (hcp- or fcc-) films on (001)-substrates are associated with an hcp ($11\bar{2}0$)-structure of the films. The experimental diffraction data can definitely not be explained by surface reconstruction of a conceivable bcc or bct (001)-film.

5.4 XPD

Virtues and shortcomings of the XPD-technique have already been discussed in Section 4.2. We wish to highlight here on some aspects that also elucidate the pros and cons of this technique. As stated in Section 4.2 the XPD results can also be explained by assuming the hexagonal ($11\bar{2}0$) orientation. Similar to the results for the fcc(110) orientation, one expects that the XPS rocking curves - measured in the plane spanned by the surface normal of Nb(001) and the $[110]$ direction - should also be dominated by forward scattering in the close-packed hexagonal (0001)-layers. The close-packed atomic chains line up along polar angles $\theta = 0^\circ$ and at $\theta = 60^\circ$ (see Fig.4.27 and Fig.5.41). The atomic plane $(1\bar{1}00)$, which is also scanned along $[110]_{\text{Nb}}$, has a close-packed atomic chain running at a polar angle $\theta = 0^\circ$ and a less densely packed atomic row at $\theta = 58.5^\circ$ (see Fig.5.41d). The latter row will cause the effective forward focusing to move from 60° to a slightly smaller angle, so that the resulting peak will lie between 59° and 60° . This is exactly what XPD-measurements on our samples yield and this is fully in accordance with results on forward scattering in ($11\bar{2}0$) oriented hcp Co films [75]. Due to the epitaxial relation of the competing fcc(110) orientation, the XPD polar scans along the $[110]$ -direction of the Nb(001)-surface would for a fcc(110)-orientation yield an effective peak that results from a superposition of the forward focusing from the (111)-planes (fig.5.41a) and the $(1\bar{1}\bar{2})$ -plane (fig.5.41b). Hence, an fcc-stacking would lead to a superposition of the peaks at $\theta = 60^\circ$ and $\theta = 67.8^\circ$ which gives rise to an effective peak moved slightly toward polar angles larger than 60° . However, as mentioned in the Section 4.2, the difference in XPD for a ($11\bar{2}0$) oriented hcp or a (110) oriented fcc phase of the film is too small to be detectable. As shown in the previous subsections it is LEED and RHEED by means of which one can clearly demonstrate, that the stacking of the close-packed planes in the films is hexagonal (hcp or dhcp) which may be generalized by stating that naturally stable fcc-materials form a ($11\bar{2}0$) oriented hexagonal phase

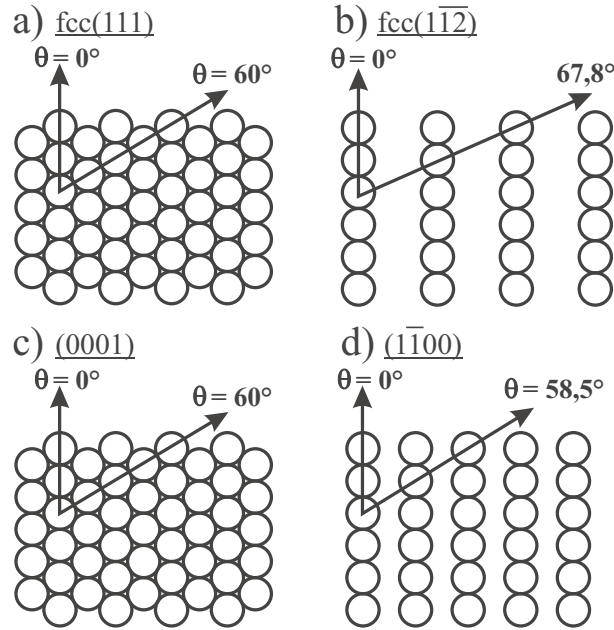


Figure 5.41: Cut through the atomic centers of two close-packed lattices.
 fcc-lattice: (a) along a (111)-plane, (b) along a $(1\bar{1}\bar{2})$ -plane
 hcp-lattice: (c) along the (0001)-plane, (d) along the $(1\bar{1}00)$ -plane.

when they are grown as films on a suitable cubic (001)-substrate of a transition metal.

5.5 UPS

UPS is not a crystal structure determination technique, but from ARUPS one can obtain information about the k -dependence of the occupied part of the electronic states of the ultraviolet-radiated sample. By means of UPS one can determine the k -periodicity (more precisely the k_{\parallel} -periodicity) of the valence band states (see section 2.2.3). The k -periodicity of valence band states is related to the film structure periodicity in real space. Hence one can determine the film crystal structure by studying the k -periodicity in the UPS emission. UPS-studies on Au films deposited on Nb(001) are an example which will briefly be discussed in the next subsection. Since the band structure (the set of k_{\parallel} -dispersive electronic states) is strongly connected with the symmetry of the respective crystal, we shall also discuss UPS-emission from Pd-films deposited on Nb(001) and W(001) substrates.

Au films on Nb(001)

Au films deposited on Nb(001) at low temperatures (low as 150K) show a poor long-range order. As a consequence RHEED, which requires long-range order, cannot provide any information about the short-range crystalline structure of the films. But even a technique that does not depend on long-range order, viz. XPD, could not give a decision about the crystalline phase of the film.

In a recent article [17] we presented an example of how QSE can be applied to determine the crystal structure of thin films. We showed that pronounced QSE in UPS from thin Au films deposited on Nb(100) occur only when the deposition is made at low temperatures, because only then the films consists of a relatively well defined number of monolayers, i.e. are smoother. A thickness fluctuation would lead to a superposition of the emission coming from QWS originating in areas of

different layer thickness and thus give rise to weak and diffuse peaks. Unfortunately, at low temperature (e.g. 150 K) the long-range order of the frozen Au surface is quite poor and RHEED does not provide any information about the film structure. XPD, which requires only short-range order, also gives only incomplete information about the structure, namely that the close-packed hexagonal layers lie perpendicular to the surface, but the stacking mode of the Au films and, consequently, their crystal structure lies outside its detection capabilities. Thus a different route had to be followed to determine the stacking mode. We applied ARUPS to analyze the electronic energy in the reciprocal space, by comparing the bulk band structure obtained from a self-consistent DFT calculation including spin-orbit interaction with analogous information obtained from ARUPS. We used an ARUPS spectrometer (an electron energy analyser) to determine the kinetic energy of the electrons relative to the Fermi level. This energy difference gives the binding energy of the emitted electrons alas, not for all k vectors, since in photo-electron emission only the in-plane momentum (k_{\parallel}) is conserved, whereas the momentum normal to the surface (k_{\perp}) remains unknown. It is exactly here where the QSE of the film can be utilised as a momentum spectrometer for the electron momentum normal to the film, because only their k_{\perp} vectors have to satisfy the boundary condition (i.e. nodes on the film-surfaces [14, 15, 16, 17]). This allowed us to determine the full periodicity of the film states in the k -space, and, subsequently, the film structure, which turned out to be hexagonal close-packed (hcp and/or dhcp) and not natural fcc.

Pd films on W(001)

With ARUPS we measured the $E(k_{\parallel})$ -dependence of a 15 ML thick Pd film deposited on W(001) which in RHEED shows the centred pattern discussed in this and previous section. The measured $E(k_{\parallel})$ -dependence reveals a flat band situated just under the Fermi-energy. In [13] we compared the measured $E(k_{\parallel})$ -dependence with those calculated for a $(11\bar{2}0)$ oriented hcp, fcc and dhcp structure of Pd. Only the bands calculated for the hcp and dhcp structures of Pd show good agreement with the experiments, thereby giving support to our conjecture that the dhcp and hcp structure constitute the origin of the centred RHEED-patterns.

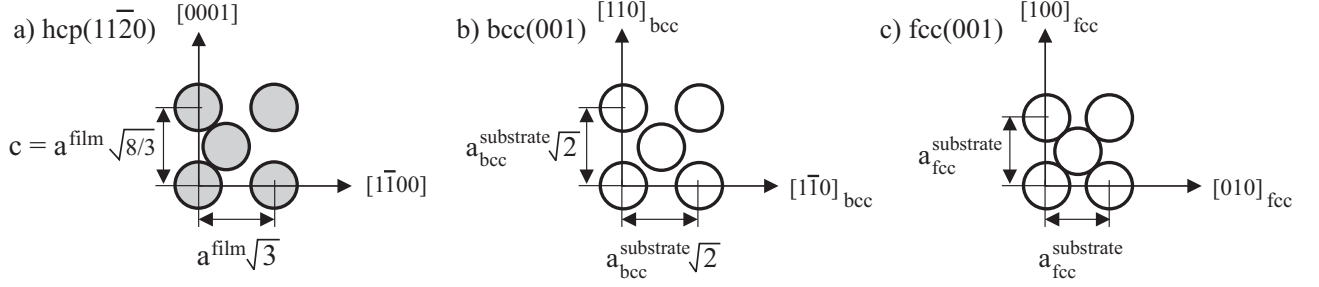


Figure 6.42: The unit cell of the hcp($11\bar{2}0$) atomic plane (panel (a)), the centred non-primitive cell of the bcc(001) and fcc(001) atomic plane (panels b,c) and the inter-atomic distances in the $[0001]$, $\langle 1\bar{1}00 \rangle$, $\langle 110 \rangle_{bcc}$, $[100]_{fcc}$ and $[010]_{fcc}$ directions. ' $a^{film} = a$ ' is the nearest neighbour distance in the close-packed material. For panel (c) we have: $a_{fcc}^{substrate} = a \cdot \sqrt{2}$.

6 Films grown in the hcp, dhcp and bct phase modification by epitaxy on (001) substrates.

6.1 Lattice misfit

The objective of the following considerations is to understand the role of the geometric in-plane fit of epitaxial film/substrate systems where the film grows by forming a hexagonal phase succeeding a primary pseudomorphic bct phase.

How can one define an appropriate measure for the inevitable misfit of the two lattices along the common plane with the substrate surface? One should bear in mind that the $(11\bar{2}0)$ oriented hcp-film grows with its stacking axis parallel to the (001) oriented substrate surface. If one cuts an hcp-crystal along the $(11\bar{2}0)$ plane which contains the stacking axis, one recognizes chains of atoms whose intra-chain distance equals $a^{film}\sqrt{3}$ (see Fig.4.27 and Fig.6.42). Here a^{film} denotes the nearest neighbor distance in an hcp- or fcc-lattice. The chains are parallel to the $[1\bar{1}00]$ -direction. Their distance parallel to the $[0001]$ -axis is equal to $c = a^{film}\sqrt{8/3}$, that is by $\approx 6\%$ smaller than the intra-chain distance. Because of the previously discussed epitaxy relations the orthogonal in-plane directions $[0001]$ and $[1\bar{1}00]$ correlate with the directions $[110]$ and $[1\bar{1}0]$ of the bcc(001) substrate. In both directions the substrate also displays chains of atoms, whose intra-chain distance is equal in the two directions and may temporarily be expressed by $a_{bcc}^{substrate}\sqrt{2}$ where $a_{bcc}^{substrate}$ denotes the bulk bcc-lattice constant (see Fig.4.27 and Fig.6.42).

One is now in the position to introduce “linear misfits” along these directions by defining

$$\Delta_{[1\bar{1}00]}^{ideal} = \left(\frac{a^{film}\sqrt{3}}{a_{bcc}^{substrate}\sqrt{2}} - 1 \right) \cdot 100\% = \left(\frac{\sqrt{3}}{2} \cdot \frac{a_{fcc}^{film}}{a_{bcc}^{substrate}} - 1 \right) \cdot 100\%$$

$$\Delta_{[0001]}^{ideal} = \left(\frac{a^{film}\sqrt{\frac{8}{3}}}{a_{bcc}^{substrate}\sqrt{2}} - 1 \right) \cdot 100\% = \left(\sqrt{\frac{2}{3}} \cdot \frac{a_{fcc}^{film}}{a_{bcc}^{substrate}} - 1 \right) \cdot 100\%$$

We have alternatively used a_{fcc}^{film} in place of a^{film} where the former quantity denotes just the fcc-lattice constant which is identical with the side length of the unit cube, that is $a_{fcc}^{film} = a^{film}\sqrt{2}$. Clearly, if the substrate structure were fcc-type and would exhibit a (001)-surface, $a_{bcc}^{substrate}\sqrt{2}$ has to be replaced by $a_{fcc}^{substrate}$ in the above equations (see also Fig.6.42).

The superscript “ideal” of the misfit Δ has been introduced to indicate that the ratio $c/a = \sqrt{8/3} \simeq 1.63$ refers to an ideal hcp-lattice of which hcp Co-films prove to be a very good example. The

Table 6.6: Calculated lattice constants of the non-equilibrium bcc-phase of late transition metals and noble metals. The calculation is based on the assumption that the atomic volume is conserved when the metals are forced into a non-equilibrium bcc-phase. This assumption is corroborated by self-consistent ab-initio electronic structure calculations on the respective metals. The total energy minimum was always attained at the same atomic volume irrespective of the fixed fcc- or bcc-lattice symmetry. Clearly, the minimum value of the total energy is higher for the non-equilibrium phase.

metal	Co	Ni	Cu	Rh	Pd	Ag	Ir	Pt	Au
$a_{bcc}/\text{\AA}$	2.817	2.793	2.865	3.015	3.087	3.246	3.047	3.111	3.238

experimental c/a -ratio comes out close to 1.62. However, hcp-films whose natural lattice structure is fcc have an slightly enlarged c/a -ratio of up to 1.67. This has already been discussed in Section 4. As a result of the conservation of the atomic volume the lattice constant of the “unnatural” hcp-films reduces by 0.77% and hence a^{film} has to be replaced by $0.9923a^{film}$. The above equations may now be rewritten for the realistic misfits:

$$\Delta_{[1\bar{1}00]}^{real} = \left(\frac{0.9923a^{film}\sqrt{3}}{a_{bcc}^{substrate}\sqrt{2}} - 1 \right) \cdot 100\% = \left(\frac{\sqrt{3}}{2} \cdot \frac{0.9923a_{fcc}^{film}}{a_{bcc}^{substrate}} - 1 \right) \cdot 100\%$$

$$\Delta_{[0001]}^{real} = \left(\frac{0.9923a^{film} \cdot 1.67}{a_{bcc}^{substrate}\sqrt{2}} - 1 \right) \cdot 100\% = \left(\frac{1.67}{2} \cdot \frac{0.9923a_{fcc}^{film}}{a_{bcc}^{substrate}} - 1 \right) \cdot 100\% .$$

If the film would grow not by forming an hcp-lattice but rather by creating a (001)-oriented bcc-lattice, the corresponding misfits were identical in both directions and simply given by

$$\Delta_{bcc} = \left(\frac{a_{bcc}^{film}}{a_{bcc}^{substrate}} - 1 \right) \cdot 100\% .$$

If the film is naturally fcc-type but has been forced into a bcc-modification, the above argument on the conservation of atomic volume applies as well. The atomic volume of an fcc-lattice containing 4 atoms per unit cube, is given by $a_{fcc}^3/4$. The unit cube of a bcc-lattice comprises only 2 atoms so that one obtains $a_{bcc}^3/2$ for the atomic volume in this case. The lattice constant of the bcc film phase was calculated from the fcc lattice under the assumption that the atomic volume is conserved, that is by setting $a_{bcc}^3/2 = a_{fcc}^3/4$. The resulting bcc lattice constants for late transition metals and noble metals are given in table 6.6. Hence we have $a_{fcc}^{film}/a_{bcc}^{substrate} = 2^{1/3} = 1.26$. The above equation for Δ_{bcc} may hence alternatively be written

$$\Delta_{bcc} = \left(\frac{a_{bcc}^{film}}{a_{bcc}^{substrate}} - 1 \right) \cdot 100\% = \left(2^{-\frac{1}{3}} \cdot \frac{a_{fcc}^{film}}{a_{bcc}^{substrate}} - 1 \right) \cdot 100\%$$

Clearly, Δ_{bcc} vanishes if $a_{fcc}^{film}/a_{bcc}^{substrate} = 1.26$ indicating an ideal fit of the adsorbate onto the substrate. If the substrate possesses fcc-structure one has to replace $a_{bcc}^{substrate}\sqrt{2}$ by $a_{fcc}^{substrate}$ as in the analogous case above.

The quantities $\Delta_{[1\bar{1}00]}^{real}$, $\Delta_{[0001]}^{real}$ and the above misfit are plotted in Fig.6.43 as a function of the ratio $a_{fcc}^{film}/a_{bcc}^{substrate}$.

In the following we shall analyze which of the two misfit, i.e. a low misfit in the $[1\bar{1}00]$ -direction or a low misfit along the stacking direction ($[0001]$), is more important to the occurrence of the $(11\bar{2}0)$ oriented hexagonal phase.

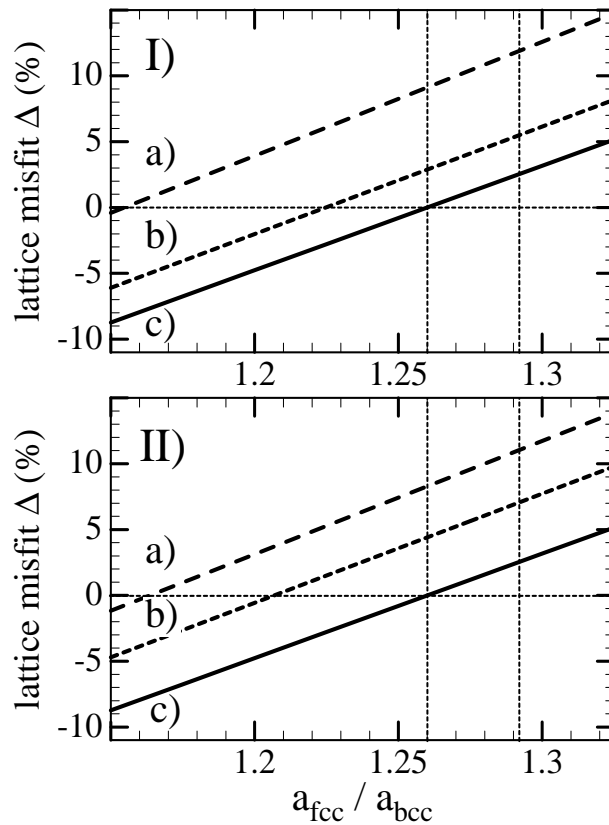


Figure 6.43: The relative discrepancy (Δ) in percent of fcc-metals on bcc(001) if they grow in hcp($11\bar{2}0$) epitaxy. Δ is plotted along the two high symmetry directions discussed in the text: (a) along $[1\bar{1}00]$ (b) along $[0001]$. The cases shown in the upper and lower panel (I) and (II), respectively) refer to c/a -ratios of 1.63 (theoretical value) and 1.67 (experimental value), respectively. The solid curve (c) pertains to the relative misfit Δ for a bcc(001) orientation. The misfits are plotted as functions of the ratio a_{fcc}/a_{bcc} where $a_{fcc} = a/\sqrt{2}$ and a denotes the side length of the fcc-unit cube and a_{bcc} stands for the side length of the primitive mesh of the bcc(001)-surface.

6.2 Effect of the lattice misfit: Examples

In Tables 6.7, 6.8, 6.9, 6.10, 6.11, and 6.12 we have listed epitaxial systems of late transition and noble metal films whose diffraction patterns can be associated with a , respectively, hcp ($11\bar{2}0$)-phase, a dhcp phase (Tables 6.11, 6.12) or with a bcc (or bct) (001)-phase (Tables 6.7, 6.8, 6.9, 6.10).

It can be seen from these tables that pseudomorphic growth (i.e. the growth of a bct (001)-phase) occurs in all systems up to a critical coverage. Thereafter the films transform either into a ($11\bar{2}0$) oriented hexagonal or (001) oriented fcc phase. When the misfit of the hexagonal ($11\bar{2}0$)-phase in the $[1\bar{1}00]$ -direction is small, the pseudomorphic-growth persists up to 2 monolayers (ML's). However, when the misfit of the hexagonal phase modification is small in the $[0001]$ -direction the pseudomorphic-growth range expands up to 10 or more ML's. That means, at a small $\Delta_{[1\bar{1}00]}$ the hexagonal ($11\bar{2}0$)-phase appears already after two pseudomorphic ML's, whereas, if $\Delta_{[0001]}$ is small, that phase forms only after some 10 pseudomorphic ML's. Thus, a good fit in the $[1\bar{1}00]$ -direction favors a sooner appearance of the hexagonal phase rendering a good fit in the $[0001]$ -stacking direction less important.

This applies as well to the two epitaxial systems Cu/Nb(001) and Au/W(001) where the experimentally estimated limits for the growth of the hexagonal ($11\bar{2}0$)-phase clearly demonstrate the crucial

Table 6.7: Range of pseudomorphic growth (i.e. growth of a bct (001)-phase) of cobalt on bcc (001)-substrates. The epitaxial systems are listed in the first column. The second column shows the ratio ρ defined as the side length of the unit square of the fcc (001)-film surface divided by the side length of the unit square of the bcc (001)-substrate surface. The relative misfit of an assumed bcc (001)-phase of the film with respect to the bcc (001)-substrate surface is listed in the third column. Lattice constants of the bcc-phase modifications are presented in Tab.6.6. The misfits are calculated as in Fig.6.43. The fourth column refers to the ratio c/a of the tetragonal pseudomorphic bct(001) lattice. This ratio is calculated as explained in Section 6.1. The fifth column pertains to the limits of the observed pseudomorphic growth given in monolayers.

epitaxial system film/substrate	ρ $a_{\text{film}}/a_{\text{sub}}$	bcc(001) Δ_{bcc}	ratio c/a of pseudomorphic bct	pseudomorphic growth up to
Co/W(001)	1.1233	-10.8%	0.708	2 ML
Co/Cr(001)	1.2326	-2.0%	0.942	3 ML
Co/Au(001)	1.2320	-2.0%	0.942	4 ML
Co/Fe(001)	1.2319	-2.0%	0.944	10 ML
Co/Fe(001)	— —	— —	— —	— —
Co/strFe(001) ^b	1.2582	-0.0%	1.007	10 ML
Co/Pd(001)	1.2909	+2.5%	1.074	30 ML
Co/Si(001)	1.3022	+3.3%	1.116	10 ML
Co/Rh(001)	1.3114	+4.3%	1.148	10 ML

^bStrained Fe(001) buffer layers with an in-plane lattice constant of 2.81 Å obtained by pseudomorphical growth on GaAs(001) or Ge(001) [97].

importance of a good fit in the $[1\bar{1}00]$ -direction rather than in the $[0001]$ -stacking direction. Hence, not surprisingly, Cu grows on Nb(001) already after two pseudomorphic ML's in the hcp-phase despite a large misfit of -9.4% in the $[0001]$ -stacking direction, and this is because of a smaller misfit of -6.0% in the $[1\bar{1}00]$ -direction.

Au on W(001) displays similarly large misfits but in a reversed order: the largest misfit (-10.9%) occurs in the $[1\bar{1}00]$ direction and the smaller one (-7.0%) in the $[0001]$ -direction. Although these misfits are similar in magnitude as for Cu on Nb(001), the Au-films do not develop any hcp growth. But since the Au-misfit in the crucial $[1\bar{1}00]$ -direction is by a factor of ≈ 2 larger than the respective Cu-misfit, there is no hcp-growth, corroborating the above empirical rule extracted from the tabulated material on the epitaxial systems.

Table 6.8: Continuation of Table 6.7. The second column reports the techniques by means of which the pseudomorphic-growth has been observed. The respective authors are quoted. The last column lists the crystal phases of the film beyond the pseudomorphic-regime. Details on these phases are presented in Tables (6.11) and (6.12).

epitaxial system film/substrate	pseudomorphic growth determined by ^c	film phase after pseudomorphic ^e
Co/W(001)	RHEED [10, 11] ^d , LEED [88, 60, 81]	hcp [10, 11] ^d
Co/Cr(001)	RHEED, XRD [90]	hcp [90, 91, 92, 89]
Co/Au(001)	HREM [83]	hcp [82, 83]
Co/Fe(001)	RHEED [101], PDME [75, 93]	hcp [101, 75, 102, 98]
Co/Fe(001)	AED [103], XPD [94], LEED [98]-IV [98]	— —
Co/GaAs(001)	XPD [104], RHEED [95]	hcp [104, 96, 95]
Co/strFe(001) ^f	LEED [97]-IV [97] ^g	hcp [97] ^g
Co/Pd(001)	XPD [105]	—
Co/Si(001)	XPD [106]	—
Co/Rh(001)	LEED [107]	—

^cList of abbreviations:

RHEED (reflection high energy diffraction (pattern)),
 LEED (low energy electron diffraction (pattern)),
 LEED-IV (spot intensity (I) versus primary electron energy (potential)),
 XRD (X-ray diffraction),
 HREM ((atomic-resolved) high resolution electron microscopy),
 PDME (primary-beam diffraction modulated electron emission),
 AED (Auger electron diffraction),
 XPD (X-ray photo-electron diffraction),
 STM (scanning tunneling microscopy with atomic resolution),
 XANES (X-ray absorption near-edge structure),
 EXAFS (extended X-ray-absorption fine structure),
 FEM (field emission microscopy).

^dExperimental data obtained in the current work.

^eMore details on the growth beyond the pseudomorphic-regime are reported in the ensuing subsection.

^fStrained Fe(001) buffer layers with a in-plane lattice constant of 2.81 Å obtained by pseudomorphic growth on GaAs(001) or Ge(001) [97].

^gDetails are presented in the next sections.

Table 6.9: The same as in Table 6.7 (range of pseudomorphic-growth), but now for the remaining late transition metals and for the noble metals.

epitaxial system film/substrate	ρ $a_{\text{film}}/a_{\text{sub}}$	bcc(001) Δ_{bcc}	ratio c/a of pseudomorphic bct	pseudomorphic growth up to
Ni/W(001)	1.1139	-11.5%	0.690	1 ML
Ni/Ag(001)	1.2265	-2.6%	0.911	4 ML
Ni/Au(001)	1.2265	-2.6%	0.912	4 ML
Ni/Fe(001)	1.2265	-2.6%	0.921	4 ML
Cu/Nb(001)	1.0939	-13.0%	0.654	2 ML
Cu/W(001)	1.1424	-9.3%	0.745	2 ML
Cu/V(001)	1.1668	-5.4%	0.845	2 ML
Cu/Ag(001)	1.2482	-0.8%	0.974	8 ML
Cu/Au(001)	1.2534	-0.4%	0.984	10 ML
Cu/Fe(001)	1.2578	-0.1%	0.994	9 ML
Cu/Pt(001)	1.3032	+3.4%	1.106	10 ML
Cu/Pd(001)	1.3128	+4.2%	1.130	10 ML
Rh/Nb(001)	1.1515	-8.5%	0.763	2 ML
Rh/Fe(001)	1.3224	+5.0%	1.159	3 ML
Pd/Nb(001)	1.1787	-6.4%	0.818	2 ML
Pd/W(001)	1.2310	-2.2%	0.932	2 ML
Ag/Nb(001)	1.2394	-1.6%	0.952	2 ML
Ag/W(001)	1.2310	+2.7%	1.083	4 ML
Ag/V(001)	1.349	+7.1%	1.230	10 ML
Pt/W(001)	1.240	-1.5%	0.954	2 ML
Au/Nb(001)	1.2364	-1.8%	0.945	2 ML
Au/W(001)	1.2911	+2.5%	1.075	10 ML

Table 6.10: Continuation of the previous Table 6.9

epitaxial system film/substrate	pseudomorphic growth determined by	film phase after pseudomorphic
Ni/W(001)	LEED [108], FEM [109]	hcp, dhcp [78]
Ni/Ag(001)	HREM [83]	dhcp [83, 9, 77]
Ni/Au(001)	RHEED [72], HREM [83]	hcp/dhcp [72, 9, 83]
Ni/Fe(001)	LEED [71]-IV [71], RHEED [110, 111, 72]	hcp [9] ^h
Cu/Nb(001)	RHEED ^h	hcp ^h
Cu/W(001)	RHEED [10, 112] ^h , LEED [64, 88]	hcp [10, 112, 100] ^h
Cu/V(001)	LEED [113]	–
Cu/Ag(001)	STM [114], RHEED [115], LEED [116]-IV [116]	bcc [77]
Cu/Ag(001)	XPD [117], XANES, EXAFS [118]	– –
Cu/Au(001)	STM [119, 120]	–
Cu/Fe(001)	RHEED [115, 72, 121], LEED [122]	hcp [9]
Cu/Pt(001)	STM [144]	–
Cu/Pd(001)	LEED [123, 3]-IV [123], STM [3]	fcc [123, 3]
Rh/Nb(001)	RHEED ^h	hcp/dhcp ^h
Rh/Fe(001)	XRD [124]	fct [124]
Pd/Nb(001)	RHEED [12, 13] ^h	hcp/dhcp [12, 13] ^h
Pd/W(001)	RHEED [10, 11], LEED [67]	hcp/dhcp [10, 11] ^h
Ag/Nb(001)	RHEED [19] ^h	hcp [19] ^h
Ag/W(001)	LEED [63]	fcc [63]
Ag/V(001)	LEED [125, 126]	–
Pt/W(001)	LEED [127]	–
Au/Nb(001)	RHEED [19] ^h	hcp [17, 19] ^h
Au/W(001)	RHEED [5] ^h	fcc [5] ^h

^hExperimental data obtained in the current work.

Table 6.11: Epitaxial systems that develop subsequent to the pseudomorphic-regime and whose diffraction patterns conform to the identification of the film structure of the deposited late transition metals as hcp or dhcp ($11\bar{2}0$)-phases. The ratio (ρ) is defined as in Table 6.7 and listed in the second column. The following two columns report the relative misfits Δ (in percent) of the ($11\bar{2}0$)-films along the $[1\bar{1}00]$ -direction and along the $[0001]$ -direction with respect to the substrate surface. The misfits are calculated as in Fig.6.43. The hcp ratio c/a was chosen to be 1.67, only for Co-films a ratio of 1.63 appeared to be more appropriate. The fifth column refers to the respective film structures with ($11\bar{2}0$)-surfaces that conform to the LEED and RHEED (true) reflection pattern obtained from films with atomically smooth surfaces.

epitaxial system film/substrate	ρ $a_{\text{film}}/a_{\text{sub}}$	hcp($11\bar{2}0$)		LEED/ RHEED
		$\Delta_{[1\bar{1}00]}$	$\Delta_{[0001]}$	
Co/W(001)	1.1233	-2.7%	-9.0%	hcp [10, 11, 81, 88, 60] ⁱ
Co/Mo(001)	1.1268	-2.6%	-8.9%	–
Co/Cr(001)	1.2326	+6.7%	-0.1%	hcp [90]
Co/Au(001)	1.2320	+6.7%	-0.1%	–
Co/Fe(001)	1.2319	+6.6%	0.0%	hcp [98]
Co/GaAs(001)	1.2506	+8.3%	+1.9%	–
Co/strFe(001) ^j	1.2582	+8.9%	+2.5%	hcp [97] ^k
Ni/W(001)	1.1139	-4.2%	-7.7%	–
Ni/Ag(001)	1.2266	+5.3%	+1.6%	hcp [111]
Ni/Au(001)	1.2265	+5.3%	+1.6%	–
Ni/Fe(001)	1.2264	+5.3%	+1.6%	hcp [71, 110, 111]
Cu/Nb(001)	1.0939	-6.0%	-9.4%	–
Cu/W(001)	1.1424	-1.8%	-5.3%	hcp [10, 112, 100, 88] ⁱ
Cu/Fe(001)	1.2534	+8.0%	+4.2%	hcp [115]
Rh/Nb(001)	1.1515	-1.0%	-4.5%	–
Rh/W(001)	1.2025	+3.3%	-0.3%	–
Rh/Mo(001)	1.2063	+3.6%	-0.0%	–
Pd/Nb(001)	1.1787	+1.3%	-2.3%	hcp,dhcp [12, 13, 19] ⁱ
Pd/W(001)	1.2310	+5.7%	+2.0%	hcp,dhcp [67, 10, 11] ⁱ
Pd/Mo(001)	1.2349	+6.1%	+2.3%	–
Ag/Nb(001)	1.2394	+6.5%	+2.6%	hcp [19] ⁱ
Ir/W(001)	1.2152	+4.4%	+0.6%	–
Ir/Mo(001)	1.2190	+4.7%	+1.0%	–
Pt/W(001)	1.2405	+6.6%	+2.7%	–
Pt/Mo(001)	1.2444	+6.9%	+3.1%	–
Au/Nb(001)	1.2364	+6.2%	+2.4%	hcp,dhcp [17] ⁱ

ⁱDiffraction pattern obtained in the current work.

^jStrained Fe(001) buffer layers with a in-plane lattice constant of 2.81 Å obtained by pseudomorphic growth on GaAs(001) or Ge(001) [97].

^kDetails are given in the next sections.

Table 6.12: Continuation of Table 6.11. Identification of the post-pseudomorphic growth as yielding hcp or dhcp (11 $\bar{2}$ 0)-films : scrutinizing consistency of the results obtained from various diffraction techniques, i.e. transmission RHEED, TED and other methods. The second, third and fourth column refer to the respective technique that led to the listed structure identification.

epitaxial system film/substrate	RHEED transmission	TED	from other techniques
Co/W(001)	hcp [10, 11] ^l	–	–
Co/Mo(001)	hcp [89]	–	hcp (XRD [89])
Co/Cr(001)	hcp [92, 89]	–	hcp (XRD [90, 91])
Co/Au(001)	hcp [82]	hcp [83]	hcp (XRD [82], HREM [83])
Co/Fe(001)	hcp [102]	–	hcp (XRD [101], PDME [75])
Co/GaAs(001)	hcp [95]	hcp [96, 95]	–
Co/strFe(001) ^m	–	–	hcp (LEED-IV [97] ⁿ)
Ni/W(001)	–	hcp,dhcp [78]	–
Ni/Ag(001)	–	hcp,dhcp [83, 77]	dhcp (HREM [83])
Ni/Au(001)	hcp,dhcp [72]	hcp/dhcp [83]	dhcp (HREM [83])
Ni/Fe(001)	hcp [72]	–	hcp,dhcp (XRD [128])
Cu/Nb(001)	hcp [9, 19] ^l	–	–
Cu/W(001)	hcp [10] ^l	hcp [78]	hcp (LEED-IV [100])
Cu/Fe(001)	hcp [72]	–	–
Rh/Nb(001)	hcp,dhcp ^l	–	–
Rh/W(001)	–	hcp,dhcp [79]	–
Rh/Mo(001)	–	hcp,dhcp [79]	–
Pd/Nb(001)	hcp,dhcp [12, 13] ^l	–	–
Pd/W(001)	hcp,dhcp [10, 11] ^l	hcp,dhcp [79]	–
Pd/Mo(001)	–	hcp,dhcp [79]	–
Ag/Nb(001)	hcp [9, 19] ^l	–	–
Ir/W(001)	–	hcp,dhcp [79]	–
Ir/Mo(001)	–	hcp,dhcp [79]	–
Pt/W(001)	–	hcp,dhcp [79]	–
Pt/Mo(001)	–	hcp,dhcp [79]	–
Au/Nb(001)	hcp [17] ^l	–	–

^lExperimental data obtained in the current work.

^mStrained Fe(001) buffer layers with a in-plane lattice constant of 2.81 Å obtained by pseudomorphic growth on GaAs(001) or Ge(001) [97].

ⁿDetails are given in the next sections.

7 Stability of the hexagonal close-packed phase modification. Epitaxy in the light of the crystal phase transformation.

Except manganese metal, which is conspicuous by a more complex lattice, all elemental metals possess a close-packed (fcc, hcp or dhcp) or body centered cubic (bcc) crystal structure. A distinct property of these lattices is that every atom lies in a hollow site of the next atomic plane. The predominance of close-packed (fcc- or hcp-) structures suggests that these lattices come about by minimization of the total energy of the respective system that seems to lack directional bonds and whose atoms behave like elastic spheres attracting each other through two-body forces. But the fact that an fcc-metal grows by exactly maintaining an ABCABC-stacking clearly proves that there is also a directional portion in the interatomic bonding otherwise the metal would switch at random from fcc-stacking to hcp-stacking. In the case of bcc-metals which are not close-packed the presence of directional bonds is even more obvious. But despite the limitations of an overly simplified model of interatomic bonds in metals, one can understand quite a variety of stability-related phenomena of metal/metal epitaxy by simply resorting to the “hollow-site model” based on the above observation.

7.1 The pseudomorphic bct (001)-phase in transition to hexagonal close-packed structures.

In the preceding section we have compiled the experimental evidence for this particular phenomenon: when the film starts building a hcp ($11\bar{2}0$)-oriented lattice, a small misfit in the $[1\bar{1}00]$ -direction is more important than a good fit in the stacking direction $[0001]$. In addition, it can be seen from the figures and the tables on the epitaxial systems investigated that there is a correlation between small misfits in the $[1\bar{1}00]$ -direction and values $c/a < 1$ of the pseudomorphic-film in its forced bct (001)-phase. Conversely, if $\Delta_{[1\bar{1}00]}$ is large but $\Delta_{[0001]}$ small, one has $c/a > 1$. We shall demonstrate that the tetragonal ratio c/a is of absolutely crucial importance to the appearance of the ($11\bar{2}0$) oriented hcp modification.

At the first stage of epitaxial growth the hollow sites for the atoms of the first adsorbate ML are the hollow sites of the substrate surface. If the adsorbate/substrate bond outweighs the interatomic bond strength in the first adlayer the latter is forced into the hollow sites of the substrate surface which causes the build-up of a pseudomorphic ML. If the bond is sufficiently strong a second pseudomorphic ML develops. This situation prevails with metals deposited on open (001)-oriented surfaces as in the case of Pd on Nb(001).

The strong bond of Pd to Nb(001) causes a growth of two pseudomorphic ML's of Pd. The strength of the Pd/Nb-interaction outweighs the energy cost for the necessary in-plane stretch of the two Pd-ML's to achieve a pseudomorphic fit. As the Pd metal tends to conserve its atomic volume, the second Pd-layer is shifted toward the substrate, thereby forming a bct (001)-film with a tetragonal ratio of $c/a = 0.82$.

The geometric consequences of this tetragonal distortion are illustrated in Fig.7.44, Fig.7.45 and Fig.7.46. Where the substrate first ceases to directly influence the film growth, namely perpendicular to the surface, the adsorbate starts building its natural close-packed hexagonal atomic planes, still controlled by in-plane-pseudomorphism. Clearly, the overall energy balance favors this departure from pure pseudomorphic growth. That means: perpendicular to the surface the pieces of rectangular bct(110) planes transform into pieces of close-packed hexagonal planes. These hexagonal planes will be called 'hexagons' in the following. As the pseudomorphic growth continues, it is strongly influenced by the appearance of these hexagons because they change the distribution of the hollow-sites in the direction out-of-plane. For a bcc (110)-plane the hollow-sites are adjacent to 4 atoms (see

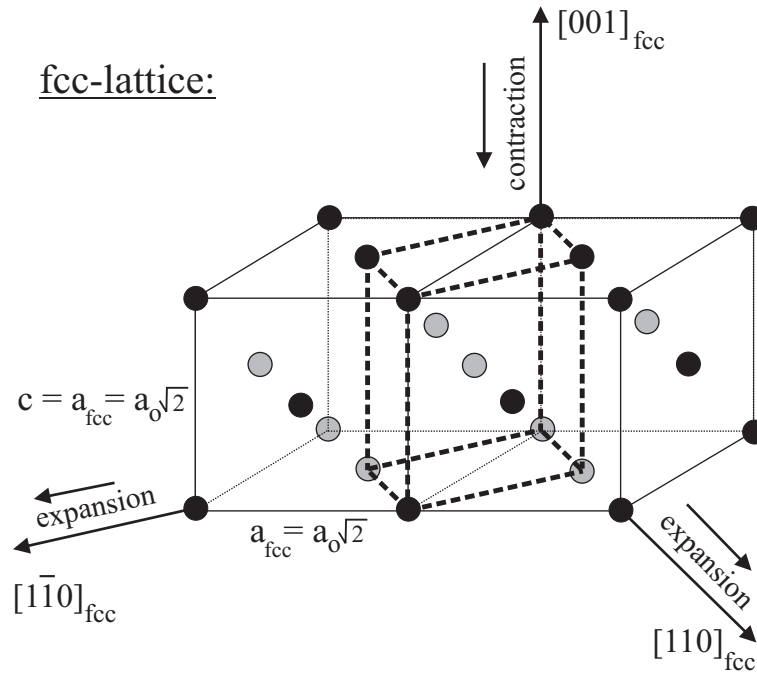


Figure 7.44: Two units of the fcc-lattice. The body-centred tetragonal unit cell of the fcc-lattice is drawn in heavy dashed lines. The arrow indicates the direction of contraction that occurs on stretching the lattice parallel to the (001)-substrate surface. This contraction/expansion correlation is governed by the tendency of the lattice to retain the atomic volume of its natural phase.

panel (a) of Fig.7.46) whereas the hollow sites of the bct(110) plane with $c/a=0.82$ (the hexagons, see panel (b) of Fig.7.46) move into the middle of equilateral triangles (see panel (c) of Fig.7.46). As a consequence, the bct (110)-planes with $c/a=0.82$ (the hexagons) have to shift from the four-fold sites of the nearest bcc(110)-planes (see panel (b) of Fig.7.46) to the three-fold hollow sites of the hexagons (see panel (c) of Fig.7.46). Mishin et al. [129] have demonstrated by atomistic (*ab-initio*) simulations using an embedded-atom method potential (EAM1) and molecular dynamic calculations that this relative displacements of bct(110)-sublattices in the $[110]_{\text{bct}}$ direction parallel to the substrate cannot energetically be counteracted by the substrate. Once the hexagons appear they start shifting automatically to the three-fold hollow sites of the nearest hexagons.

There are two possible ways of sharing the hollow sites of the already existing hexagons by the following hexagons (see Fig.7.46). One can either shift the hexagons into hcp- or fcc-positions connected with ABAB... and ABCABC... stacking, respectively. The shifts required for the latter case are not only larger, but, moreover, fcc-stacking will place more atoms of the hexagons into unfavorable sites of the underlying atomic layer (i.e. into bridge and on-top positions). Hence, the film keeps growing by hcp-stacking, and this is exactly what is confirmed by the observed centered reflection and transmission patterns.

As can be concluded from the above considerations, the important criterion for hcp-growth to occur on top of the pseudomorphic bct (001)-layers does not consist in requiring the c/a -ratio to be close to 0.82 but rather that this ratio has to be generally smaller than unity. The bct-phase constitutes a lattice of lower symmetry and is therefore unstable with respect to changes that increase the symmetry. As already stated above, films of bct-structure relax in the direction of the surface normal where the influence of the substrate quickly weakens. That means that the bct (110)-planes relax into the close-packed hexagonal planes which are the most stable planes of close-packed materials. The relaxation into the close-packed phase can easily be achieved by shifting the hexagons shown in Fig.(7.46) into the three-fold hollow sites which, however, are available only after completion of the 3rd ML. This

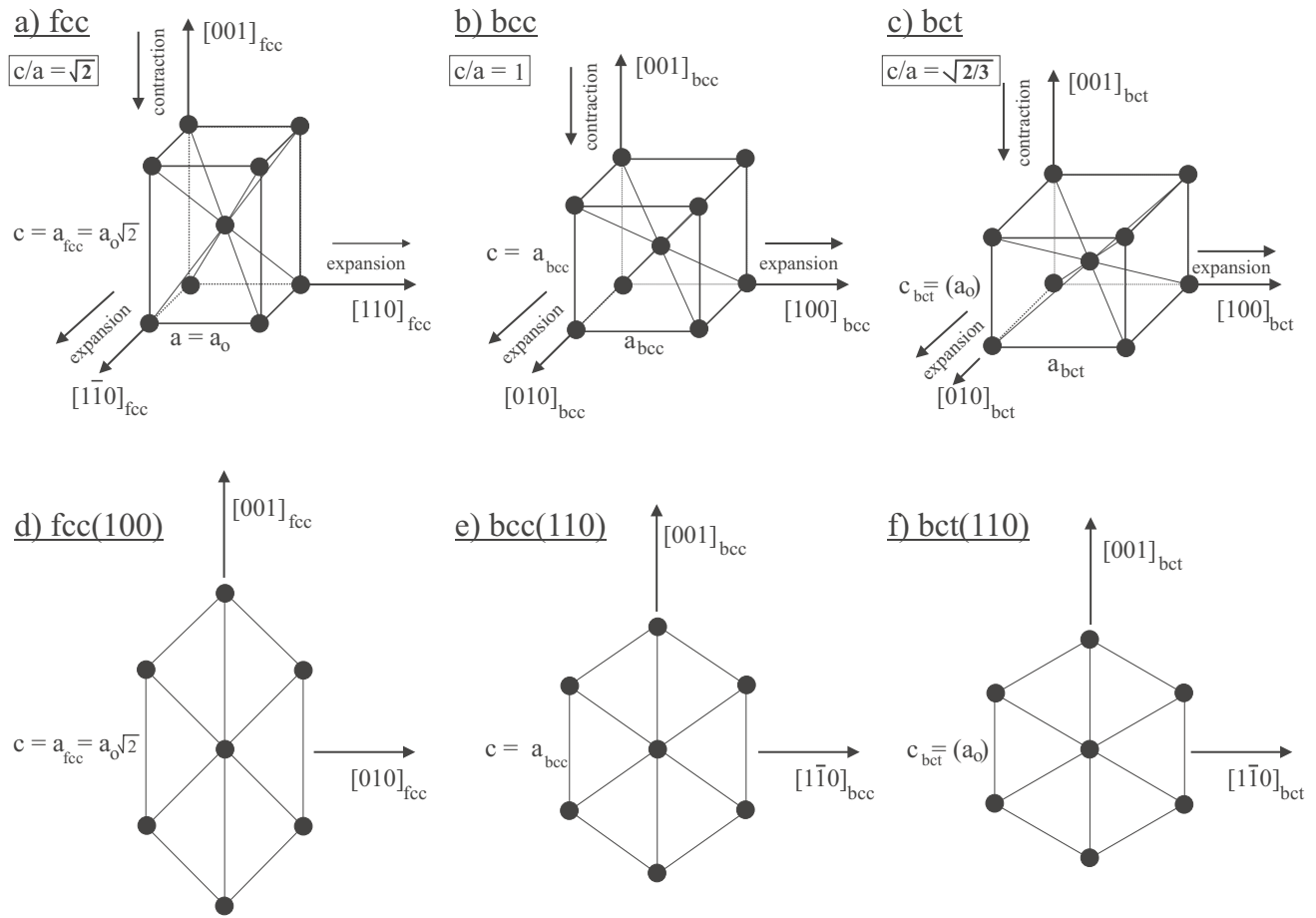


Figure 7.45: Body centered unit cells for various c/a -ratios

a) Body-centered tetragonal cell of the fcc-lattice ($c/a=\sqrt{2}$)

b) Body-centered lattice ($c/a=1$).

c) Body-centered tetragonal cell ($c/a=\sqrt{2/3} \sim 0.82$)

By compressing the lattice along the $[001]$ -direction at constant atomic volume the fcc (100) -plane (panel (d)) transforms into the bcc (110) -plane (e), and into perfect hexagons (f) for $c/a=\sqrt{2/3}$ (i.e. into the close-packed hexagonal (0001) -plane which is equivalent to the fcc (111) -plane).

explains why for $c/a < 1$ only two pseudomorphic-MLs are stable. (See the corresponding Table of the last section).

7.2 Experimental data on the stability of films grown in a $(11\bar{2}0)$ oriented hcp phase modification

The occurrence of non-fcc stacking in our epitaxial systems seems to be most plausibly explained by the improved lattice fit gained by a hexagonal (hcp,dhcp) stacking in forming the close-packed planes of the adsorbate on top of the (001) oriented substrate as compared to what would result from an fcc stacking. Conventionally, the analysis of epitaxial growth is based on discussing the quality of the geometrical fit of the two lattices that are involved. The interplay between pseudomorphic-growth and geometrical fit reflects, of course, the tendency of the respective system to minimize its total energy. But there are certain cases where that minimum is primarily inaccessible, which means, its access would require a considerable activation energy. Hence the primarily formed non-equilibrium phase is thermodynamically hindered and persists even

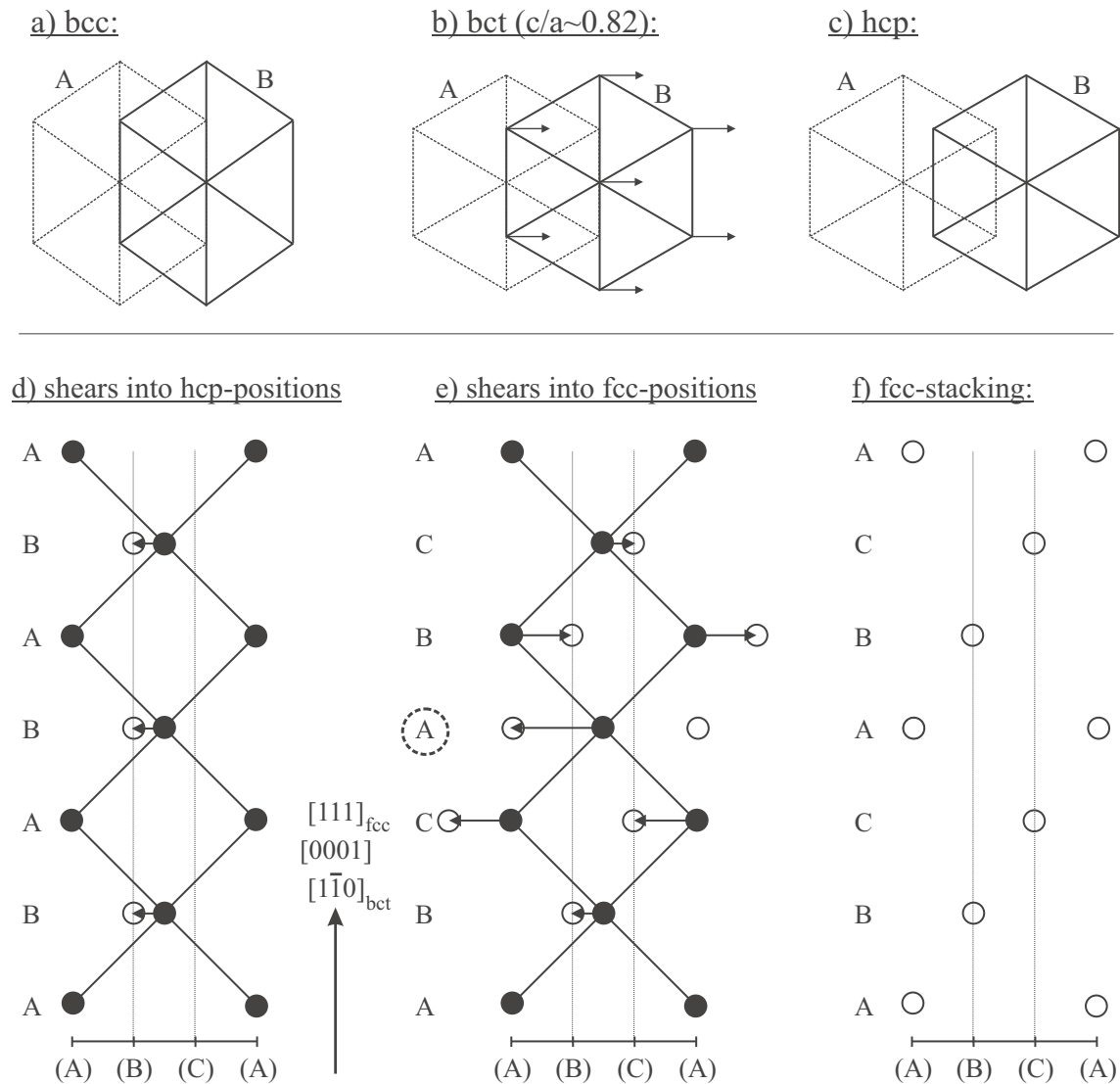


Figure 7.46: Transforming the bcc (110)-planes into hcp (0001)-planes. The shifts of the bct (110)-plane (B) from bridge to hollow sites are indicated by arrows. In order to transform bcc into hcp an internal shift along $[1\bar{1}0]$ is required moving every second layer into hcp-positions (panel (b,c)). In addition, one needs a uniform strain (contraction at constant atomic volume) along $[001]$ which leads to perfect hexagons (see fig.7.45a,b). Any close-packed structure arises from a particular stacking of these hexagonal lattice planes. At each step of the stacking the atoms of a given plane have to be placed above triangular interstitials of the plane below the positions of which will further be referred to as triangular hollow sites. This rule defines three possible stacking positions, commonly denoted A, B, and C.

a,b) The bct stacking sequence (ABAB...) of bct (110)-planes. For $c/a < 1$ atoms begin to overlap. As a consequence, the hexagons slide into hollow sites of the triangles formed by the three nearest neighbor atoms of a hexagon (see panel (c)). Sliding into hcp-positions takes obviously shorter shifts which constitutes one strong reason of preference. In addition, the alternative shift of film-atoms into fcc-positions (fcc-stacking) places many of them near energetically unfavorable on-top and bridge-sites of the underlying substrate-surface (square-mesh), thereby preventing the growth of the natural fcc-phase (see also Fig.4.27).

- when the film is annealed or
- when the epitaxial growth control of the substrate on the film fades off (as with top layers of thick films) or even
- the respective film is stripped-off the the substrate, thereby removing any interaction with the originally phase inducing source.

In the following we have compiled some experimental facts that bear evidence of the actual occurrence of these cases, where films do **not** convert into their natural fcc-stacking once their formation started in the hcp-stacking mode.

In some cases (as for Cu films deposited on Nb(001)) the hcp($11\bar{2}0$) films eventually convert into the natural fcc-structure of the bulk, but this does not come about in that the close-packed planes switch from their hcp-stacking growth mode to fcc-stacking whereby a $(11\bar{2}0)$ oriented hcp film would transform into the (110) oriented fcc structure. In actual fact the phase transition proves to be more complex involving a tetragonal distortion that provides a link in building up the (001) oriented fcc structure by forming an intermediate bcc(001) phase.

At this point it should be recalled that the close-packed layers grow perpendicular to the plane of the film. Obviously the build-up of the native fcc phase amounts to shifting the hexagons in a fcc-stacking mode associated with a (110) oriented fcc structure (see Fig.7.46). In other words, one would expect a displacive transformation. Surprisingly, this is not observed. The experimental data provide unambiguous evidence that there is something in the way of this transformation. To find a rationale for this unexpected phenomenon we first discuss what happens when adjacent close-packed planes are shifted relative to each other. It is instructive to start with a glance at the following list which reviews the mentioned data on the stability of the hexagonal phase modification in films grown on (001) oriented cubic substrates.

1. Facts illustrating the thickness limit of non-equilibrium hcp-films grown on (001) oriented substrates
 - (a) RHEED-transmission images of Ag and Au films deposited on Nb(001) and having a thickness of 100 ML still display the hcp-transmission pattern without any fcc-related traces [19]. Similarly, TED-experiments on Ni, Rh, Pd, Ir and Pt films of about 50 ML thickness grown on W(001) and Mo(001) by Bruce and Jaeger [79, 78] yield patterns that can only be associated with $(11\bar{2}0)$ oriented hcp-structure.
 - (b) Ni films on Fe(001) grow evidently in a hcp-stacking mode up to thicknesses of 200 MLs. By contrast, Ni on Au(001) develops a $(11\bar{2}0)$ -oriented dhcp-structure that appears already at 5 MLs and persists up 100 MLs [9].
 - (c) As is evidenced by RHEED- and XPD-studies, Cu films of 100 ML thickness deposited on Nb(001) display a (001) oriented fcc structure, rather than the expected fcc (110) orientation. This applies as well to similarly thick Pd films grown on Nb(001). However, different from the results on the Cu films the respective RHEED pattern contains also portions of rings embedded in a high background intensity suggesting the partial presence of polycrystalline structure.
2. Influence of annealing on the stability of the non-equilibrium hcp-phase:
 - (a) The non-equilibrium hcp-structure of Cu and Ag films is not affected by annealing.
 - (b) Annealing Pd-films thicker than 6 MLs to temperatures higher than 400K induces a change of the crystal structure from hcp to dhcp without a change of the film orientation. More precisely, the film converts from a $(11\bar{2}0)$ -oriented hcp structure the $(11\bar{2}0)$ -oriented dhcp structure. In Pd- films of a thickness equal to or larger than 20 MLs the

dhcp phase was also observed when they were grown at 300K. Au films show a similar effect, but because of the high background in the RHEED images the experimental evidence is sizably impaired.

- (c) TED-studies support the absence of a hcp-dhcp phase changeover in films of Ni, Rh, Pd, Ir and Pt deposited on W(001) and Mo(001) at any annealing temperature. The hcp-associated transmission patterns clearly persist in these films.

- 3. Ni, Rh, Pd, Ir and Pt-films retain their $(11\bar{2}0)$ -oriented hcp structure when they are stripped off the substrate. This is also evidenced by TED-studies.

In order to gain access to the thermodynamical barrier preventing the mentioned systems from leaving their non-equilibrium state, we shall analyse the implications of the film morphology, in particular the special epitaxial relation that controls the $\text{hcp}(11\bar{2}0)$ – $\text{fcc}(110)$ phase transformation path. We shall demonstrate that the persistence of the $\text{hcp}(11\bar{2}0)$ structure is tied to the special epitaxial growth of the films in two orthogonal rectangular domains which is connected with the four-fold symmetry of the (001) oriented substrate. These two orthogonal domains lock the respective film to the $\text{hcp}(11\bar{2}0)$ structure due to a high-energy barrier in the reaction path of the $\text{hcp}(11\bar{2}0)$ – $\text{fcc}(110)$ transformation. The occurrence of this transformation would destroy that domain-topology. To show this we shall first focus on the variation of the total energy when a hexagonal close-packed layer slides across the adjacent layers in a close-packed metal.

7.3 Sliding a close-packed atomic layer across an adjacent layer to change the stacking sequence

Hexagonal atomic layers can stack in two modes because of the the three-fold hollow sites of the adjacent hexagonal layers. One mode is specific to the fcc phase which consists of an ABCABC...array of close-packed layers A, B and C stacked on top of each other, B and C with smallest, but different relative in-plane translations with respect to the A-layer. The alternative ABAB...stacking is specific to the hcp phase (see e.g. Fig.1.2). Other stacking sequences are necessarily a combination of these two stacking modes. Consequently, if one wants to change the stacking sequence one has to displace hexagonal close-packed layers e.g. in the $\langle 211 \rangle_{\text{fcc}}$ ($[1\bar{1}00]$) direction from the three-fold hollow sites to the “wrong” three-fold hollow site characteristic of the other stacking sequence. This shift can be done in two ways. One can either shift the atoms of a close-packed layer across a “bridge” position in the (adjacent) layer (see Fig. 7.47a,b,c,d,e,f), or across an “on-top” position of that layer (Fig. 7.47g,h,i,j,k,l). In the latter case a large atomic overlap occurs compared to the first choice (compare e.g. Fig. 7.47h,k with Fig. 7.47b,e). It is therefore to be expected that a displacement requiring the crossing of an on-top position would be accompanied by a considerably larger increase of the total energy than a shift across a bridge position. The latter situation is depicted in panel (b) of Fig. 7.48. In the following we attempt to obtain an estimate of the relative strength of these two energy barriers.

Obviously, when the close-packed planes lie in the hollow-sites of the adjacent atomic planes the total energy of the system attains its minimum. When the atoms of all close-packed planes coincide with bridge (bonding) positions of the adjacent layers the lattice possesses a bct symmetry with a tetragonal ratio of $c/a \sim 0.82$. This bct-structure is tenfold coordinated and is also known as the bct_{10} lattice [130]. In the following we shall call this structure the bct_{10} lattice. The position of the close-packed planes in the bct_{10} structure (Fig.7.47b,e) is also known as the ‘non-stable stacking sequence’. The stacking sequence is ABAB... as in the hcp-structure, but the positions of the atoms are not the three-fold hollow sites of the hexagons but the energetically higher bridge positions of the next hexagon. The lattice tends to reduce its energy by shifting the close-packed planes from the bct-position (Fig.7.47b,e) into the three-fold hollow sites of the hexagons (Fig.7.47c,f). Sob and coworkers have shown this by DFT-calculations performed for transition and noble metals [131, 132, 133]. The total energy of the non-stable bct stacking mode is for late transition and noble metals quite close to that of the bcc-phase. The total energy of that bct was recently compiled by Mehl and Papaconstantopolous [130].

Clearly, a stacking mode where the atoms of consecutive close-packed planes lie in ‘on-top’ positions of the next hexagons yields also an unstable stacking of layers. In this case the lattice has a simple hexagonal symmetry. Each close-packed plane is stacked directly on-top of the adjacent layer (yielding, for example, AAA... stacking). Results of total energy calculations on the simple hexagonal phase are not available as yet, but there are some on the simple cubic phase. Wang and Sob calculated the total energy of the simple cubic phase for copper and for transition metals [131]. They found the total energy difference between the simple cubic phase and the fcc-phase to be at least 12 times larger than the difference that results if the simple cubic phase is replaced by the bct phase with $c/a=0.82$ (bct_{10}). In the simple cubic phase the atoms of a layer lie on-top of the atoms of the adjacent layer, exactly as the atoms in the simple hexagonal phase. One can therefore expect the analogous energy difference between the simple-hexagonal (sh-)phase and the fcc-phase to be also about 12 times larger than the difference obtained on replacing the sh-phase by the bct_{10} -phase. Hence, the energy barrier to overcome in changing the stacking sequence by a shift of close-packed planes into ‘on-top’ rather than into bridge positions will correspondingly be about 12-times higher.

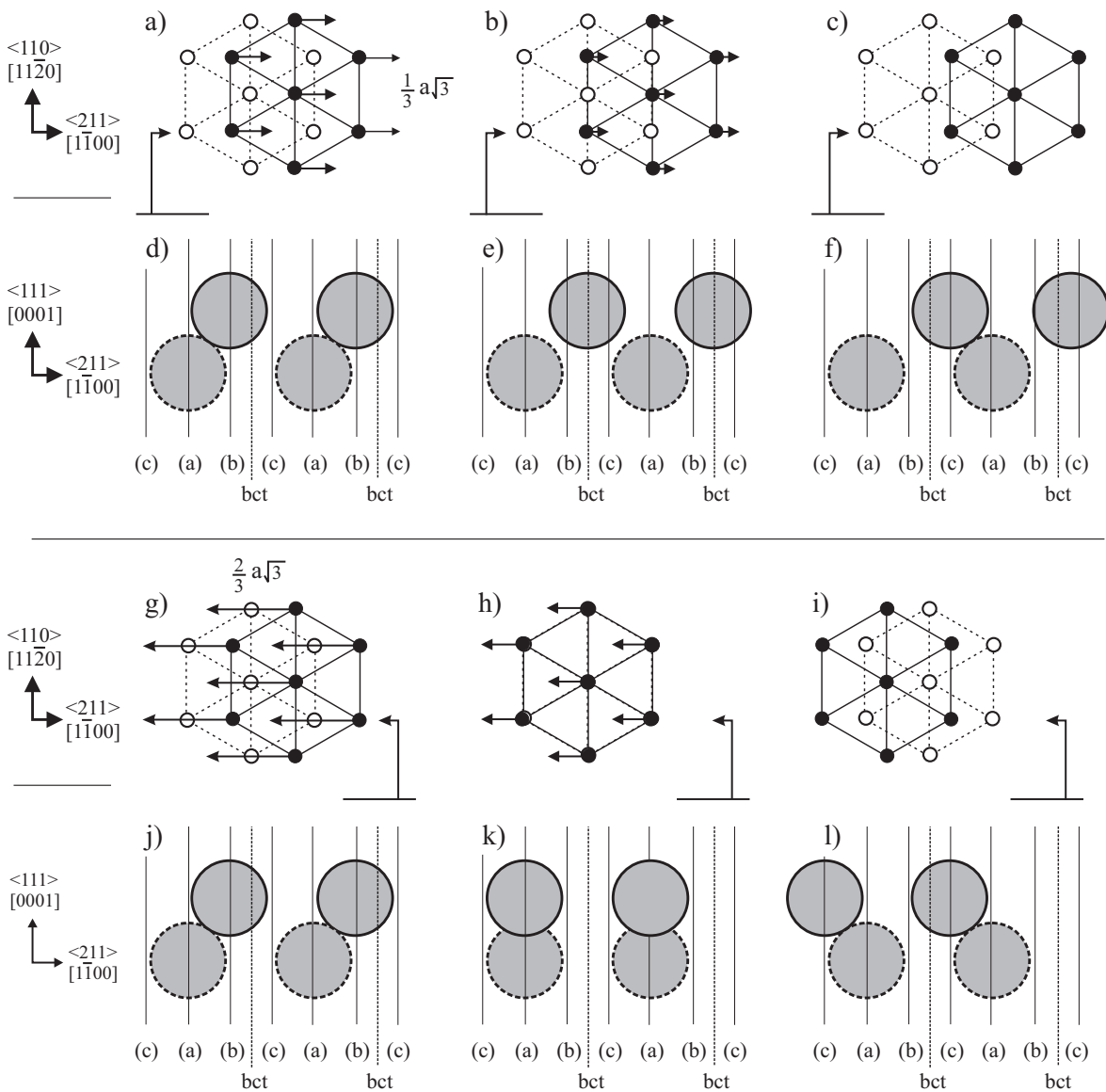


Figure 7.47: Two ways of sliding close-packed planes from a three-fold hollow site to another equivalent site. We depict two close-packed planes ((111) and (0001) , s. panels a,b,c,g,h,i) and the corresponding atoms in the $(11\bar{2}0)$ planes (d,e,f,j,k,l). The $(11\bar{2}0)$ plane lies perpendicular to the close-packed planes. The hooked arrows indicate the place of the $(11\bar{2}0)$ cut through the close-packed planes. Due to the six-fold symmetry of the close-packed planes there are two possibilities, called stacking positions, to occupy its three fold hollow sites by atoms of an adjacent close-packed plane. There are two ways of moving the adjacent plane from one stacking position to the other one.

One way (a,b,c,d,e,f) consists in moving the close-packed planes over a distance of $(1/3)a\sqrt{3}$ in the $\langle 211 \rangle$ direction. The initial stacking sequence is (a)(b). The stacking sequence changes from (a)(b) (panels a,d) to (a)(c) (panels c,f) where a bridge position is passed (a)(bct) (panels b,e). In that position the interatomic distances are smallest along this path. There (b,e) the structure is bct. Hence, in changing the stacking sequence that way the interface goes through a bct-array associated with a tetragonal ratio of $c/a=0.82$.

g,h,i,j,k,l) The stacking position can also be changed by a shift that is two times larger (i.e. by a shift of $(2/3)a\sqrt{3}$). Here the stacking sequence changes from (a)(b) (panels g,j) to (c)(a) (panels i,l), and one goes across an on-top position (a)(a) (panels h,k) where the atoms have the smallest nearest-neighbour distance and the crystal structure is simple-hexagonal.

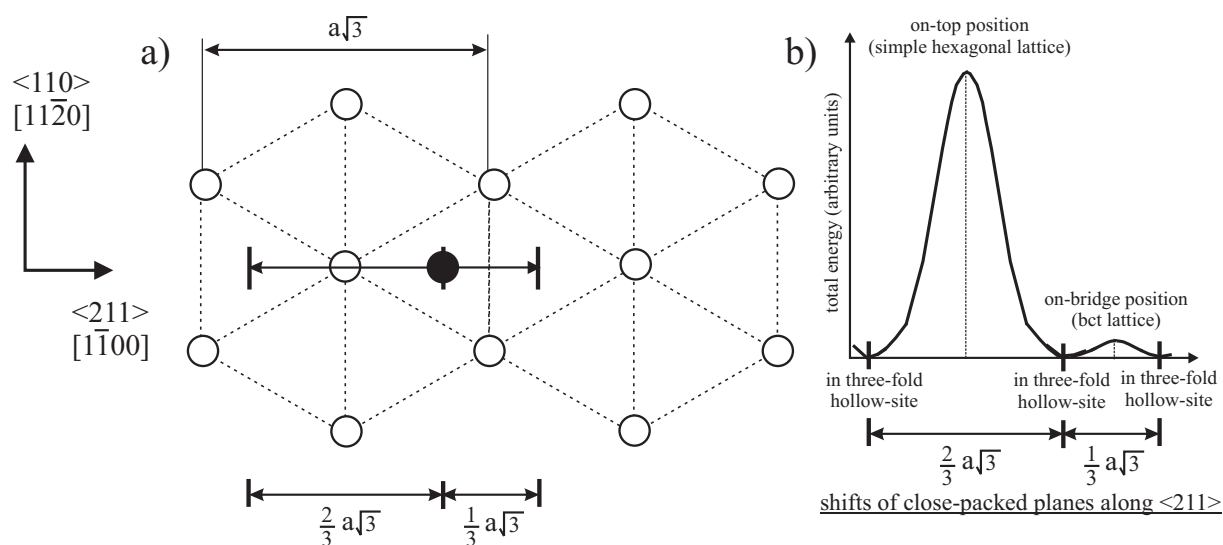


Figure 7.48: a) Sketch of two paths of changing the position of the atom marked in black from a three-fold hollow site to an equivalent site. The path across the on-top position is marked by a left arrow, the other path across the bridge position by a right arrow.

b) Associated energy barriers. As the atom shifts to another position the energy rises and attains its maximum when the atom passes the on-top or bridge position where the interatomic overlaps are largest. Because the on-top position and the bridge position belong, respectively, to a simple hexagonal lattice (sh) and bct_{10} lattice, the increase of the total energy in going from fcc to sh and from fcc to bct_{10} will definitely correlate with the energy barriers governing the stability of the non-equilibrium hcp-structures of metallic films. Tests and discussions of this interrelation are given in the text.

7.4 Models of changing the stacking sequence.

In a recent article we have elucidated how the stability of bulk transition metals can be predicted by merely exploiting electronic structure information [22]. Using Rh as an example, we found that the bcc crystal phase of bulk transition metals with native fcc structure is unstable, whereas their hcp or dhcp phase modification is meta-stable. One is hence led to conclude that there exists at least one bcc to fcc phase transition path with a very low energy barrier. This is contrasted by all conceivable hcp to fcc transition paths that definitely contain a notable energy barrier preventing the system in its build-up of layers from switching the stacking mode such that it could change from a non-equilibrium hcp-structure to an equilibrium fcc-lattice. Still, the activation energy connected with this barrier could be low enough to allow a hcp-fcc transition even below room temperature. In the following we shall try to find estimates of these energy barriers.

7.4.1 Transition from hcp- to the dhcp-stacking

A distinctive feature of hcp-to-fcc phase transitions is that this change of structure only requires a shift of one of four close-packed layers in the $[1\bar{1}00]$ direction along a distance of $b = (a\sqrt{3})/3$ and only across bridge positions. This transformation path which we shall label “path-4” is referred to in the panels l,m of Fig. 7.49. The energy-barrier that appears along this transformation path is half the difference between the energy of the bct-phase where all atoms lie in bridge position of adjacent layers (the bct_{10} structure) and the the respective energy of the hcp-structure. The total energy per atom in the hcp-phase of transition metals and noble metals should be only slightly higher compared to the respective energy in the fcc-phase as the two lattices differ only in the stacking of their close-packed atomic planes. (We mention only in passing that all energies discussed here and in the ensuing considerations are referenced to a representative atom of the material under study, except mentioned otherwise.)

Summarizing the above consideration we arrive at:

$$E_{bar}^{hcp-dhcp} = \frac{1}{2} (E_{bct_{10}} - E_{hcp}) \simeq \frac{1}{2} (E_{bct_{10}} - E_{fcc}). \quad (7.12)$$

In order to estimate the transition temperature T we apply the standard approximation also used, for example, by Wentzcovitch and Krakauer [134], which consists in simply equating the energy-barrier to $k_B T$ where k_B denotes the Boltzmann constant. Unfortunately, this transition temperature is occasionally also referred to as ‘activation energy’ [134] of the phase transition. These ‘activation energies’ and the associated energy barriers for all noble-metals and their transition metal neighbors are listed in the sixth and seventh column of table 7.13.

7.4.2 Transition from hcp- to fcc-stacking

As we have mentioned just a few sentences earlier, the hcp- and fcc-structure differ only in different stackings of close-packed planes. It is hence obvious that the transition path with lowest energy barrier from hcp to fcc will be such that the close-packed planes are conserved and it takes only a small relative in-plane shift to change the stacking from hcp- to fcc-type. The difference in the stacking becomes particularly well visible in the $(11\bar{2}0)$ plane (see Fig.1.2.4.27) where hcp-stacking shows up as a zig-zag array of nearest-neighbor atoms. By contrast, the distinctive feature of fcc-stacking is dramatically reflected in the linear array of nearest-neighbor atoms in the fcc(110)-plane. Hence, in a hcp→fcc transition the zig-zag pattern will eventually fade into a linear array. There are three possibilities to make this occur which is illustrated in panels (a) to (k) of Fig.7.49.

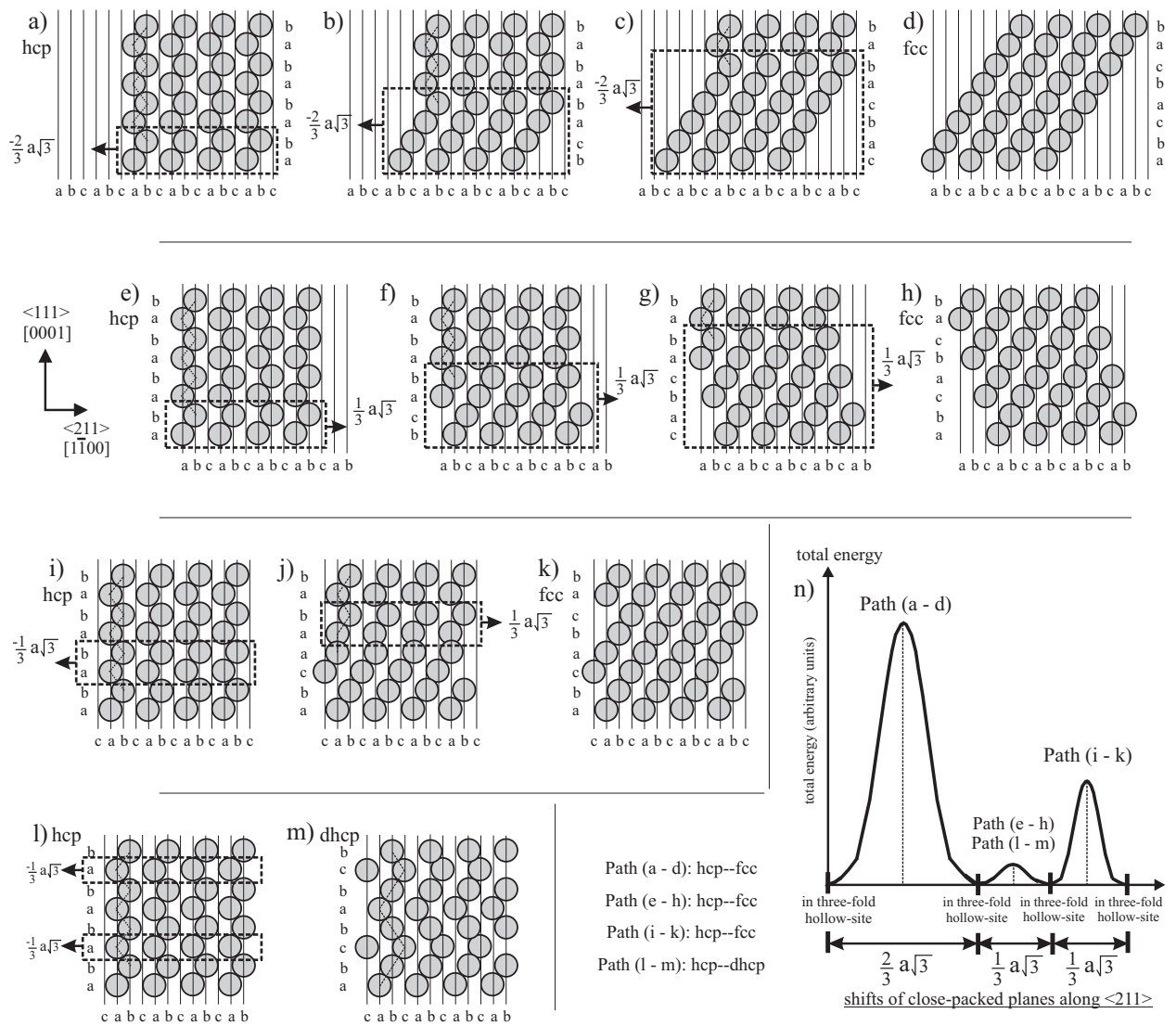


Figure 7.49: Change of the stacking sequence in going from hcp to fcc (panels (a) to (k)) and from hcp to dhcp (l,m) by shifts of close-packed planes. The images show the (11 $\bar{2}$ 0) atomic planes with respect to which the close-packed planes lie perpendicular. To depict the hcp-phase (a,e,i,l) we have chosen the c-positions to be unoccupied. The nearest-neighbour (nn) atoms form a zig-zag array. If one shifts close-packed planes as illustrated in the panels one obtains for dhcp a partial and for fcc a complete linear array of nn atoms. Note that for hcp→fcc transitions packets of close-packed planes have to be shifted. In the case of fcc-stacking (d,h,k) the a,b,c stacking positions are consecutively occupied.

Panel (n) refers to the predicted energy barriers along the sketched transformation paths. On interfaces of close-packed planes where the planes slide on top of each over a distance of $(2/3)a\sqrt{3}$, the atoms shift across on-top positions (see Figs. 7.47, 7.48). Panel (j) depicts a situation where the atoms of adjacent close-packed planes lie on on-top positions. In those cases, which appear along the paths a-d and i-k, the resulting energy barriers are much higher than along the paths e-h and l-m where shifts across on-top positions do not appear. Path a-d refers to the case where atoms are shifted across on-top positions in every second interface, which gives rise to a high energy barrier. The paths e-h and e-m refer to an analogous shift where the atoms move in every second interface across bridge positions. Hence, the associated energy barrier is significantly lower. Path i-k describes a situation where the atoms of every two of six interfaces shift across atomic bridge positions, whereas those in one of six interfaces move across on-top positions, the latter giving rise to an increase of the energy barrier compared to the barrier along the path e-h.

In the $(11\bar{2}0)$ plane of the hcp-structure one observes that the hcp-stacking leads to a 'linear' array only over a distance of two nearest-neighbor atoms. Hence, in order to achieve a complete linear array of the fcc(110) plane one has to shift packets of two nearest-neighbor atoms in the $[1\bar{1}00]$ -direction. That means in 3 dimensions that packets of two close-packed planes have to be shifted in the $\langle 211 \rangle_{fcc}$ ($[1\bar{1}00]$) direction.

Figure 7.49 illustrates three possibilities of changing over from hcp- to fcc-stacking (or vice versa). The first two paths (labeled Path-1 and Path-2) displace the close-packed planes consecutively in the same direction (Fig.7.49a,b,c,d,e,f,g,h), whereas along the third transformation path (labeled Path-3) the close-packed planes are moved alternately in opposite directions along the $\langle 211 \rangle_{fcc}$ ($[1\bar{1}00]$) direction. Obviously, in all three cases the stacking sequence is changed from hcp to fcc, but the associated transition paths differ strongly (i) in the height of the energy barriers and (ii) in the material transport. It is exactly this and the influence of the four-fold symmetry of the (001) substrates which explains the strong stability of the $(11\bar{2}0)$ oriented films. The exact details will be the subject of the following considerations

In Fig.7.49a,b,c,d we have sketched Path-1. The hcp→fcc transition happens as follows.

The first packet of two planes is shifted in the $[1\bar{1}00]$ ($\langle 211 \rangle_{fcc}$) direction by the amount of $2b = 2(a\sqrt{3})/3$. This causes four nearest-neighbor atoms to build up a linear array in the $(11\bar{2}0)$ plane (see Fig.7.49b). The packet of four hexagons is shifted in the $[1\bar{1}00]$ ($\langle 211 \rangle_{fcc}$) direction again by the same amount of $2b = (2a\sqrt{3})/3$. As a result, one obtains a linear array in the $(11\bar{2}0)$ plane containing 6 nn atoms (see Fig.7.49c). This packet of six hexagons is now shifted in the $[1\bar{1}00]$ ($\langle 211 \rangle_{fcc}$) direction, again with the amount of $2b = (2a\sqrt{3})/3$. There are now 8 atoms lined up. This linear array is moved in the $[1\bar{1}00]$ ($\langle 211 \rangle_{fcc}$) direction again with the amount of $2b = (2a\sqrt{3})/3$. This results in a linear array of 10 nearest neighbor atoms. If one continues this scheme of displacements all atoms of the $(11\bar{2}0)$ plane will eventually end up as members of the (linear) close-packed rows of the fcc(110) plane (see Fig.7.49d). The 3-dimensional lattice then displays fcc-stacking. The n 'th packet of two hexagons is shifted by the amount of $(m - n) \cdot 2b = (2a\sqrt{3})/3$ in the $[1\bar{1}00]$ ($\langle 211 \rangle_{fcc}$) direction, where m the number of double layers that have to be shifted in fcc-positions. As these packets are shifting by the amount of $2b = (2a\sqrt{3})/3$ the atoms of one close-packed plane slide across on-top positions of the atoms of the next close-packed plane (see Figs.7.47,7.48). This happens once with every second interface of the hexagons. Consequently, the energy barrier along this transformation path equals half of the total energy difference between the simple hexagonal phase and the close-packed phase:

$$E_{Path-1}^{hcp-fcc} = \frac{12}{2} \cdot (E_{bct10} - E_{hcp}) \simeq 6 \cdot (E_{bct10} - E_{fcc}) \quad (7.13)$$

The energy barriers for Path-1 obtained from this equation are listed together with the corresponding 'activation-energies' in the fourth and fifth column of table 7.13.

In Fig.7.49,e,f,g,h we have sketched Path-2 which is very similar to Path-1, the difference being only that all shifts are consistently in opposite directions and possess a reduced value of $b = (a\sqrt{3})/3$. Consequently, the hcp→fcc transition involves only displacements across bridge positions. But since the atoms only of every second interface are shifted once across bridge positions the transition requires only an energy that is half of the energy difference between the total energy of the above discussed bct_{10} -structure with $c/a = 0.82$ and that of the hcp-structure:

$$E_{Path-2}^{hcp-fcc} = \frac{1}{2} (E_{bct10} - E_{hcp}) \simeq \frac{1}{2} (E_{bct10} - E_{fcc}) \simeq E_{bar}^{hcp-dhcp} \quad (7.14)$$

Table 7.13: Energies per atom of barrier heights and 'activation-energies' (phase-transition temperatures) for noble metals and their neighboring late-transition metals. The second column gives the difference between the total energy of the bcc-phase and the fcc-native phase. The third column lists the difference between the total-energy of the bct-phase where $c/a \simeq 0.83$ (bct_{10}) and the fcc-phase. These values were calculated by Mehl, Aguayo, Boyer and de Coss [130] who used a tight-binding method. The values for Ni are results of a first-principles DFT-calculation performed by Zeleny et al [135]. The fourth, sixth and eighth column present the predicted energies per atom for the barrier heights along the hcp→fcc transition paths: Path-1, Path-2 and Path-3 calculated according to Eqs.7.13,7.14 and 7.15. The energy barrier along Path-2 is also equal to that of the hcp→dhcp displacive transition. The fifth, seventh and ninth column list the corresponding activation energies calculated from $kT = E_{\text{barrier}}$.

fcc Metal	$\Delta E_{\text{bcc-fcc}}$ (meV)	$\Delta E_{\text{bct10-fcc}}$ (meV)	$E_{\text{Path-1}}^{\text{hcp-fcc}}$	$T_{\text{Path-1}}^{\text{hcp-fcc}}$	$E_{\text{Path-2}}^{\text{hcp-fcc}}$ $E_{\text{bar}}^{\text{hcp-dhcp}}$	$T_{\text{Path-2}}^{\text{hcp-fcc}}$ $T_{\text{bar}}^{\text{hcp-dhcp}}$	$E_{\text{Path-3}}^{\text{hcp-fcc}}$	$T_{\text{Path-3}}^{\text{hcp-fcc}}$
Cu	36.7	36.4	218meV	2532K	18.2meV	211K	85meV	986K
Ag	32.7	30.5	183meV	2124K	15.3meV	177K	72meV	825K
Au	24.3	20.2	120meV	1400K	10.1meV	117K	47meV	547K
Ni	59.1	53.2	319meV	3708K	26.6meV	309K	124meV	1440K
Pd	51.0	45.6	273meV	3180K	22.8meV	265K	107meV	1235K
Pt	136	74.8	448meV	5208K	37.4meV	434K	175meV	2025K

Note that the bct_{10} -structure had the characteristic feature that all atoms of close-packed planes lie in bridge positions.

The Path-2 associated energy barriers and their corresponding 'activation-energies' that result from this equation, are listed in the sixth and seventh column of table 7.13.

Fig.7.49i,j,k depicts Path-3 where out of a set of three packets of double layers, every second and third packet of double layers is shifted in the opposite direction along the $[1\bar{1}00]$ ($<211>_{\text{fcc}}$) direction by an amount of $b = (a\sqrt{3})/3$. It should be noticed, that because of these shifts being in opposite directions, the equally shifted packets of double layers are displaced relative to each other by an amount of $2b = (2a\sqrt{3})/3$. Along the interface the atoms slide across on-top positions. Because of the three double layers there are six interfaces. In one of six interfaces the atoms move across on-top positions, and in two of six interfaces they move over bridge positions. Consequently, the energy barrier that appears along this transformation path is equal to the sum of (i) one-sixth of the total energy difference between the simple-hexagonal phase and the close-packed phase and (ii) of one-third (i.e. $2/6$) of the total energy difference between the bct_{10} structure and the close-packed phase:

$$E_{\text{Path-3}}^{\text{hcp-fcc}} = \frac{1}{6} (E_{\text{simple}} - E_{\text{hcp}}) + \frac{2}{6} (E_{\text{bct10}} - E_{\text{fcc}}) \simeq \left(\frac{12}{6} + \frac{2}{6}\right) (E_{\text{bct10}} - E_{\text{fcc}}) = \frac{7}{3} (E_{\text{bct10}} - E_{\text{fcc}}) \quad (7.15)$$

Energy barriers thus calculated and their corresponding 'activation-energies' are listed in the eighth and ninth column of table 7.13.

7.4.3 Transition from dhcp to fcc stacking

Fig. 7.50 illustrates options of transitions from dhcp- to fcc-stacking. Summarizing the differences with respect to the hcp→fcc transition we may state:

In the dhcp→fcc transition packets of three planes and one close-packed plane are consecutively

added to the shifts. Along the Paths (a-d) and (e-h) of Fig.7.50 atoms of two interfaces out of four experience shifts across, respectively, on-top positions (Path(a-d)) or bridge positions (Path(e-h)), similar to the corresponding hcp→fcc transitions. Accordingly, the energy barriers are given then by:

$$E_{Path-1}^{dhcp-fcc} = \frac{1}{2} \cdot (E_{simple} - E_{dhcp}) \simeq \frac{12}{2} \cdot (E_{bct10} - E_{dhcp}) \simeq 6 \cdot (E_{bct10} - E_{fcc}) = E_{Path-1}^{hcp-fcc} \quad (7.16)$$

$$E_{Path-2}^{dhcp-fcc} = \frac{1}{2} (E_{bct10} - E_{dhcp}) \simeq \frac{1}{2} (E_{bct10} - E_{fcc}) \simeq E_{bar}^{hcp-dhcp} = E_{Path-2}^{hcp-fcc} \quad (7.17)$$

If one goes along Path (i-l) of Fig. 7.50 atoms in one out of eight interfaces are shifted across on-top positions and in three interfaces out of eight atoms move across bridge positions. The heights of the energy-barriers hence become:

$$E_{Path-3}^{dhcp-fcc} = \frac{1}{8} \cdot (E_{simple} - E_{dhcp}) + \frac{3}{8} \cdot (E_{bct10} - E_{dhcp}) \simeq \frac{15}{8} \cdot (E_{bct10} - E_{dhcp}) \simeq 0.81 \cdot E_{Path-3}^{hcp-fcc} \quad (7.18)$$

7.5 Test of the predicted energy barriers.

As can be seen from inspection of Table 7.13 the change from hcp- to fcc-stacking (Path-2) is associated with lowest energy barriers because the transition involves only atomic shifts across bridge positions. By contrast, Path-1 is associated with shifts across on-top positions which gives rise to very high energy barriers. The situation described by Path-3 is in between. One is dealing here with a mixture of slides across on-top and bridge positions. It has to be recalled, however, that our prediction of barriers heights is based on mostly geometric considerations. The particular electronic structure of a transition metal expressed by its d-band occupancy [22] enters into our analysis only in a very reduced form, namely via the total energy difference between the bct_{10} and fcc- structure. In order to test our predictions that derive from very simple models self-consistent ab initio DFT-calculations were performed for the case of Path-3 which involves both species of slides, i.e. slides across on-top and across bridge positions as well. The results for Pd are presented in Fig.7.51. A similar curve is obtained for Ni. DFT-total energy calculations yield 118 meV for the energy barrier in Pd that has to be overcome if a transition from the hcp-phase to the fcc-phase were to occur. The corresponding barrier height for Ni amounts to 122 meV. The barrier height for Pd is only slightly larger than the predicted value of 107 meV listed in table 7.13. For Ni the agreement is even better: 122 meV vs. 124 meV obtained from our prediction based on geometric considerations. These results give strong support to the validity of our approach.

Mishin et al. [129] performed calculations on the energy change of copper metal along Path-3 and Path-2 (which is the path associated with a low energy barrier). The authors used an embedded atom model (EAM). Moreover, they referenced part of their calculation to the 9R-structure which constitutes a close-packed structure of close-packed planes that are stacked according to 'ABC'BCA'CAB' Hence, the energy barrier obtained refers to a 9R→fcc displacive deformation sketched in Fig. 7.52. This transition is completely analogous to the hcp to fcc path.

The two transitions differ only in one feature: in the 9R→fcc phase transition packets of *three* close-packed planes are shifted rather than two in the hcp→fcc transition. Hence, according to our model, the energy barrier associated with the 9R→fcc transition should be given by:

$$E^{9R-fcc} = \frac{2}{3} E^{hcp-fcc} \quad (7.19)$$

This can be verified in the following way.

For Path-3 we have:

$$E_{Path-3}^{9R-fcc} = \frac{2}{3}E_{Path-3}^{hcp-fcc} = \frac{14}{9}(E_{bct10} - E_{fcc}) \quad (7.20)$$

and for Path-2:

$$E_{Path-2}^{9R-fcc} = \frac{2}{3}E_{Path-2}^{hcp-fcc} = \frac{2}{6}(E_{bct10} - E_{fcc}) \quad (7.21)$$

Employing their EAM technique Mishin et al. [129] also determined in their calculations on copper the energy difference $(E_{bct10} - E_{fcc}) = 45meV$. If one uses this value our model predicts: $E_{Path-2}^{9R-fcc} = 15meV$ and $E_{Path-3}^{9R-fcc} = 70meV$. Using EAM Mishin et al. [129] obtained $E_{Path-2}^{9R-fcc} \sim 16meV$ and $E_{Path-3}^{9R-fcc} \sim 80meV$. Especially the value for Path-2 agrees surprisingly well with our result. Our value for Path-3 is a slightly smaller, suggesting that our model does not overestimate barrier energies.

The order of the predicted energy barriers is paralleled by the transition temperatures which provide a direct insight into the temperature stability of non-equilibrium structures of films. The 'activation energies' for Path-2 are very low. Except for Pt, all the other metals listed should display a fragile hcp-structure and restructure into fcc already at room-temperature. Hence the observed hcp(11 $\bar{2}$ 0) structure of the films must be expected to convert into fcc(110) at room temperature which, however, is definitely in conflict with the observations. As will be elucidated in the ensuing section, this contradiction is only apparent and can be resolved by taking into account that the growth of the films is strongly influenced by the build-up of two orthogonal rectangular domains.

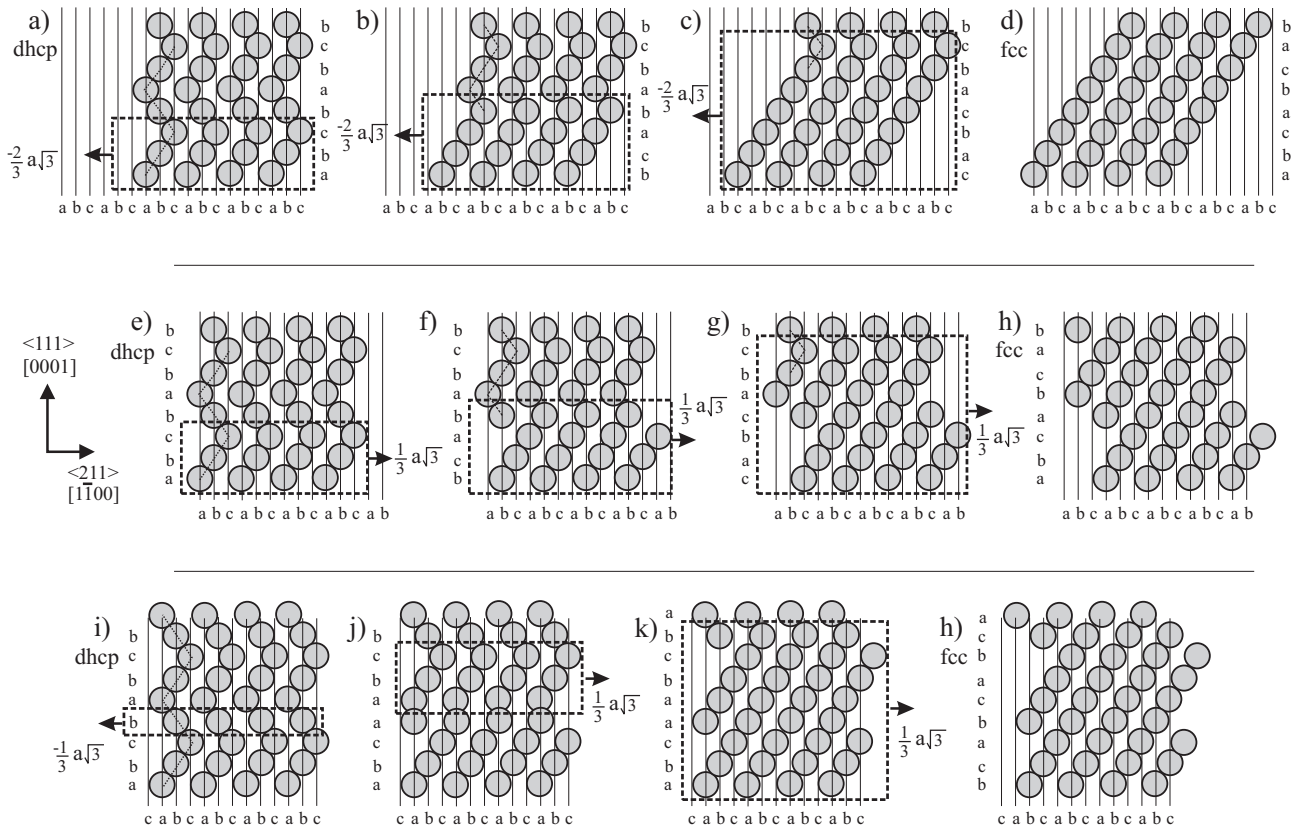


Figure 7.50: Three possibilities of changing the stacking sequence from dhcp to fcc by shifts of close-packed planes. As in Fig. 7.49 the images refer to the $(11\bar{2}0)$ atomic plane which is orthogonal to the close-packed planes. The transition paths are analogous to that of the hcp→fcc transition which Fig. 7.49 refers to. Along Path (a-d) the change in the stacking is achieved by a consecutive shift of packets of close-packed layers in one direction over a distance of $(2/3)a\sqrt{3}$. In two of four interfaces the atoms are displaced across on-top positions giving rise to a large energy barrier. Path (e-h) is similar to Path (a-d), the only difference being that the change in the stacking is accomplished by shorter shifts of $(1/3)a\sqrt{3}$. Moreover, the atoms move only across bridge positions causing a low-energy barrier along this path. As for Path (i-l), one observes that in its first section (i,j) packets of three layers and one close-packed layers are displaced over a short distance, i.e. by the amount of $(1/3)a\sqrt{3}$. But the displacements occur in opposite directions thereby crossing on-top positions. This takes place in one of 8 interfaces. To eventually arrive at fcc-stacking, one has to move packets of 8 planes across bridge positions (k) only in one direction. This is in analogy to the Paths (a-d) and (e-h). Here the shape of a rectangular domain changes systematically over to a more distorted geometry. The height of the associated energy barrier that occurs along Path (i-l) lies in between that of Path (a-d) and (e-h).

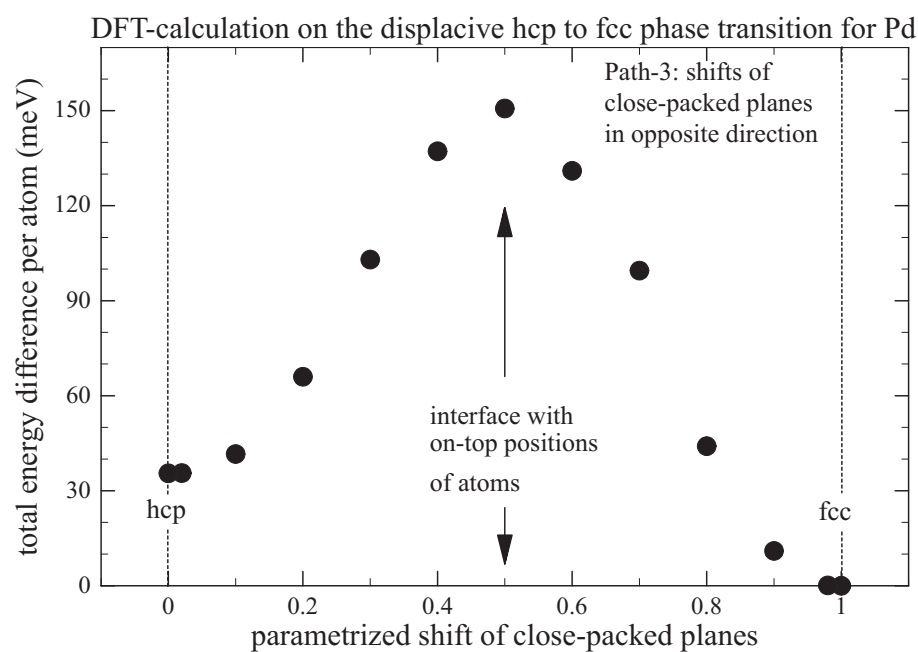


Figure 7.51: Variation of the total energy of Pd metal referenced to the total energy of its fcc phase as the hcp→fcc transition proceeds via Path-3 (see Fig.7.49). Total energies obtained from ab initio self-consistent DFT-calculations ([133]).

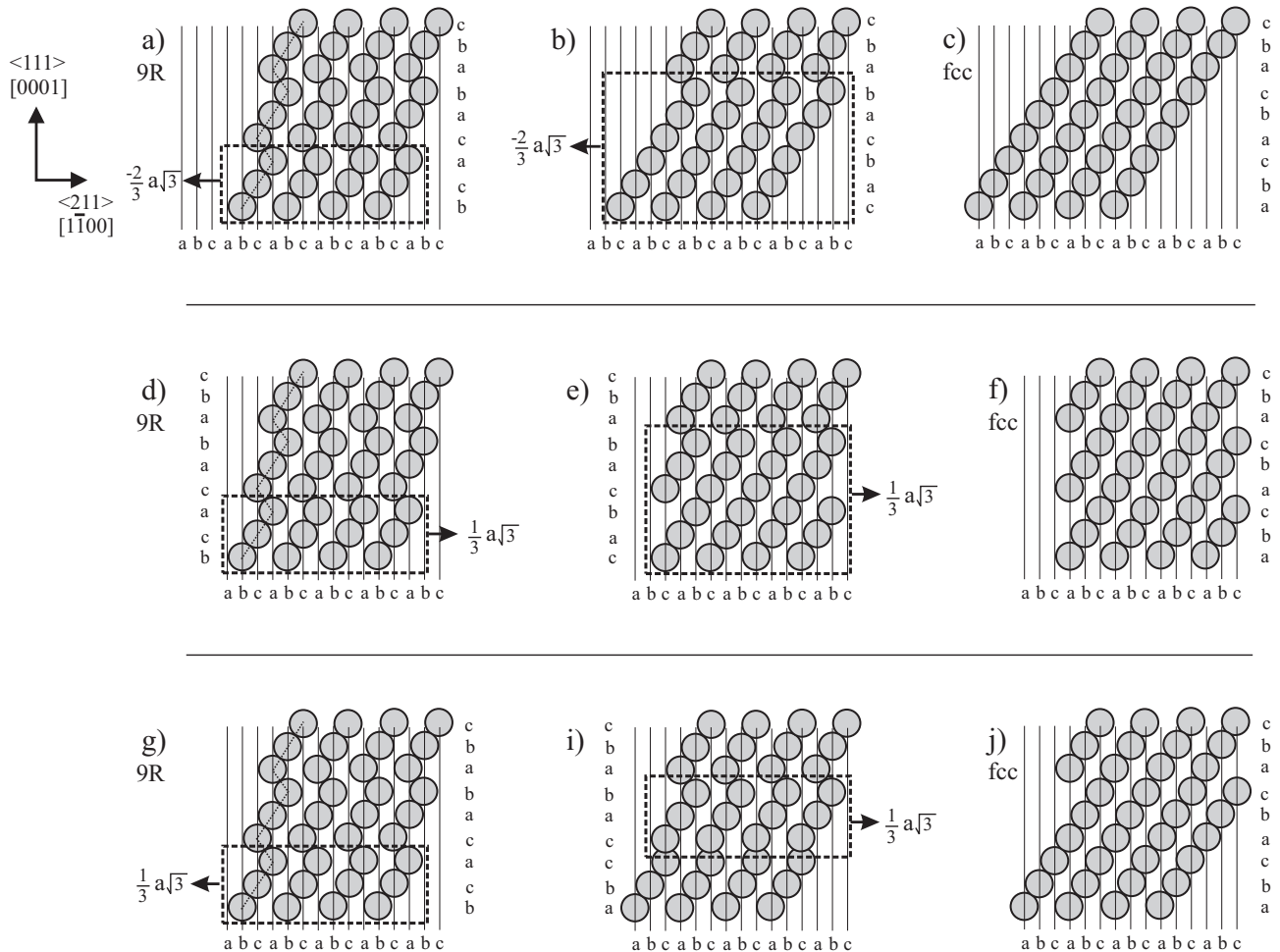


Figure 7.52: Three ways to change the stacking sequence from that of the 9R structure to that of the fcc one by shifts of close-packed planes. Depicted are the $(11\bar{2}0)$ atomic planes. The close-packed planes lies perpendicular to the represented atomic plane. The phase transformation paths are analog to that of the hcp to fcc phase transition represented in Fig. 7.49. In Path (a-c) the change in the stacking sequence is arrived by a consecutive shift of packets of close-packed layers in one and the same direction over a distance of $(2/3)a\sqrt{3}$. On each third interface the atoms are displaced over on-top atomic positions. Hence, an large energy barrier appears in the transition path (a-c). The Path (d-f) is similar to path (a-c). The difference is that the change of the stacking sequence is made by shorter shifts, i.e. over distances of $(1/3)a\sqrt{3}$. There the atoms are displaced only over on-bridge and not over on-top atomic positions. Hence the transformation path (d-e) build up a low energy barrier. Path (g-i) moves consecutively packets of three close-packed layers over the low distance of $(1/3)a\sqrt{3}$, but in opposite directions, leading also to atomic displacement over atomic on-top positions. This appears in one of 9 interfaces. The strength of the energy barrier developed in Path (g-i) is in between that of Path (a-c) and (d-f).

7.6 Influence of the domain-topology on the phase-transition.

7.6.1 Material transport in the hcp to fcc phase transition

Although the energy-barrier for the hcp→fcc transition Path-2 is low (also for Path-1), there is a drastic influence on the shape of a domain. This is illustrated in panel (a) and (b) of Fig.7.53. The shape of a previously rectangular domain transforms to an oblique-angled parallelogram. This requires a material transport over large distances. The first double-layer remains unshifted but the other ones experience displacements that increase layer by layer. The n 'th double layer moves over a distance of $(n-1) \cdot b = (n-1)a\sqrt{3}/3$, which is $(n-1)/3$ times larger than the periodicity interval in the $[1\bar{1}00]$ -direction where the planes are shifted. In Path-1 the n -th double layer moves by an amount of $2(n-1) \cdot b = 2(n-1)a\sqrt{3}/3$, which is by the factor $2(n-1)/3$ longer than the lattice period in the $[1\bar{1}00]$ -direction where the planes experience shifts. For a (110)oriented film this displacement requires the shift of the n 'th close-packed plane by a factor $(n-1)/3$ of the associated lattice period (for Path-2). For Path-1 (involving on-top atomic positions of the substrate) the corresponding factor is $2(n-1)/3$. As this would require an enormous amount of activation energy such a hcp→fcc phase transition can safely be excluded. And clearly, although this energy-barrier is primarily caused by the interaction of the first film layers with the substrate, it is independent of the film thickness. Nevertheless, from general experience one would expect that thick hcp films convert more easily into the native hcp-phase by exploiting this displacive transformation path. But the experimental facts prove that thick films can be stable up to 100 MLs. Another reason for the unexpected high stability of the hcp-phase can be traced back to the four-fold-symmetry of the (001) cubic plane that has already often been alluded to. This four-fold symmetry induces a film-growth in rectangular orthogonal hcp-domains. One can visualize the hcp-films as consisting of flat nano-crystals of the same hcp(11 $\bar{2}$ 0) orientation which keep their internal orthogonal directions [0001] and $[1\bar{1}00]$ parallel to each other (see e.g. panel (a) of Fig.7.56). Such a domain topology gives rise to a macroscopic four-fold symmetry which is just reflecting the four-fold symmetry of the (001) oriented cubic substrate. It should clearly be recognized that all hcp-films are composed of this type of densely packed, rectangular and perpendicularly aligned hcp(11 $\bar{2}$ 0) oriented micro-crystals [83]. Evidently, there is no free space between those micro-crystals. That means that the close-packed planes of the films that stay in the (11 $\bar{2}$ 0) orientation perpendicular to the film-surface, are locked inside of rectangular domains. Since the domains are orthogonal to each other with respect to their longer sides the crystal structure of the film can only be changed if the domain topology and (because of their interdependence) also the rectangular shape of the domains is conserved. Hence, shifts of the close-packed planes can only take place if the the rectangular domain shape is maintained. This is ensured with Path-3 and Path-4 (see Fig.7.51c,d). In fact, Path-4 (the hcp→dhcp transition) was experimentally observed by us, in contrast to Path-3 (hcp→fcc) in accordance with its prohibitive high energy-barrier (see table 7.13). Up to Au, the transition temperatures typical of Path-3 exceed the desorption temperatures of the metals. For that reason the films remain in there form of hcp(11 $\bar{2}$ 0) oriented micro-crystals.

We summarize this section by stating that transitions along Path-1 and Path-3 do not occur because of their high energy barriers. Their activation energies (temperature) are higher than the film desorption temperature. More surprisingly, the hcp→fcc transition path that is associated with a very low energy barrier (Path-2) does not occur as well. This phenomenon is connected with the fact that the film-topology defined by the orthogonal array of rectangular domains would be destroyed along Path-2 (see Fig.7.51g,h), and this process involves a large amount of energy. This follows from inspection of Fig.7.51e,f,g,h). Path-2 would require a rearrangement of the rectangular domains such that they overlap. This is not the case with Path-3 which conserves the domain-topology, but it is associated with too high an energy barrier. Consequently, films that display a hcp(11 $\bar{2}$ 0) oriented orthogonal rectangular-shaped domain-topology cannot change their structure by one of the (in principle conceivable) hcp→fcc transitions. The hcp(11 $\bar{2}$ 0) oriented micro-crystals are locked into the orthogonal

Table 7.14: Stacking fault energy (from Hirth and Lothe [136]) for late transition metals and noble metals listed according to the magnitude of energy.

metal	Ag	Au	Cu	Ni	Pd	Ir	Pt	Rh
γ [mJ/m^2]	16	32	45	125	180	300	322	750

pattern of rectangular nano-domains. As is evidenced by our measurements, a structural transition of films can only take place along a transition path which does not involve a material transport and for that reason avoids a change of the domain-topology. This is a film-structure transformations from the hcp(11 $\bar{2}$ 0) orientation to dhcp(11 $\bar{2}$ 0) or fcc(001) represent examples of this kind. This will briefly be analyzed in the ensuing section.

7.6.2 The hcp/dhcp phase transition

As one anneals thin Pd- or Au-films of hcp(11 $\bar{2}$ 0) up to 400 K they attain a dhcp(11 $\bar{2}$ 0) structure, whereas films of large thickness undergo this structural change already at room temperature. Pt films grown on W(001) display a structural change on annealing that is also indicative of a transition from hcp- to non-fcc-stacking. This applies similarly to Ni films grown on Ag(001) which are driven into a predominantly dhcp-stacking. This behavior follows consistently from a model that will be explained below. The hcp/dhcp phase transition is characteristic of a very low activation energy (see table 7.13) and does not require a material transport (Fig.7.51c,d). As a consequence of the latter, the domain topology is not changed. Although a hcp/dhcp phase transition of Cu- and Au-films would also require only low activation energy, one never observes the dhcp phase because the stacking-fault energy is lowest in these two metals. One should bear in mind that dhcp-stacking may be viewed as a systematic mixture of fcc and hcp-stacking, that is to say, it results from fcc-stacking where one has introduced stacking faults in a systematic way. If one were to insert the possible maximum number of stacking faults into an fcc-lattice one would generate a faultless hcp-lattice. At half this maximum number of inserted stacking faults one obtains the dhcp-lattice. Hence, if one forces an fcc-lattice of a metal into an hcp-stacking, its lattice energy increases by the number of stacking fault-energies. Compared to that, the energy of the dhcp modification is lower by a factor of two. This increase in the energy compared to a native fcc-lattice is smallest for the noble metals as can be seen from table 7.14. Insertion of a stacking-fault in the fcc-type portion of the dhcp-stacking results in a systematic hcp-stacking over 6 close-packed layers. A low stacking-fault energy in metals of native fcc-structure is tantamount to a low threshold energy for starting a local hcp stacking. Hence, because of their low stacking-fault energies Cu and Ag films turn to hcp-stacking in large portions of the film when they are annealed beyond the hcp/dhcp transition temperature. By contrast, the stacking-fault energies of gold metal and of the late transition metals are much higher. If films of these metals are annealed beyond the hcp/dhcp phase transition temperature, their stacking changes properly from hcp to dhcp, without the tendency of the films to develop portions with hcp-stacking.

7.6.3 The hcp(11 $\bar{2}$ 0)/fcc(001) phase transition.

As can be seen from Table 7.13 Cu and Ag stand out not only for low stacking fault energies, but also by smallest total energy differences between the respective bct₁₀- and the bcc-phase. Consequently, when the close-packed planes slide on top of each other into on-bridge positions (bct₁₀) there is practically no energy barrier to stop the metals from attaining the bcc-structure. As the bcc-phase is unstable [22] it can easily further transform into the fcc-phase by the so-called Bain (tetragonal) structural phase transformation. This transformation along the “Bain-path” (see Fig.7.45a,b,d,e) consists in a tetragonal transformation that conserves the atomic volume. Going along this path one

transforms a film of bcc(001)-structure smoothly into a fcc(001)-film or vice-versa.

In light of the foregoing considerations the occurrence of the fcc(001) phase in Cu films of 200 ML thickness (deposited at 300K on Nb(001)) can easily be understood.

The deposition temperature of 300K is higher than the temperature that corresponds to the activation energy required along the hcp/dhcp transition path. During the transition that takes place as a result of this situation, two of four interfaces in the set of close-packed planes are shifted across on-bridge positions. In the affected region the (11 $\bar{2}$ 0) oriented close-packed film displays, in fact, a (001) oriented bct₁₀ structure. The total energy of the bct₁₀ phase of Cu equals that of the bcc phase, and hence the (001) oriented bct₁₀ portions of the film can easily attain a bcc(001) structure. But since the bcc phase is unstable, these bcc(001) portions change over to fcc(001) along a transformation path that may be characterized by:

$$\text{hcp}(11\bar{2}0)[1\bar{1}00] \parallel \text{bct}(001)[110]_{\text{bct}} \parallel \text{bcc}(001)[110]_{\text{bcc}} \parallel \text{fcc}(001)[100]_{\text{fcc}}$$

The portion that interconnects bct₁₀(001) and bcc(001) and ends up with fcc(001) can be seen in Fig.7.45 starting from panel (c), moving to (b) and then further to (a). For a better visualization this transformation path is illustrated in Fig.7.54.

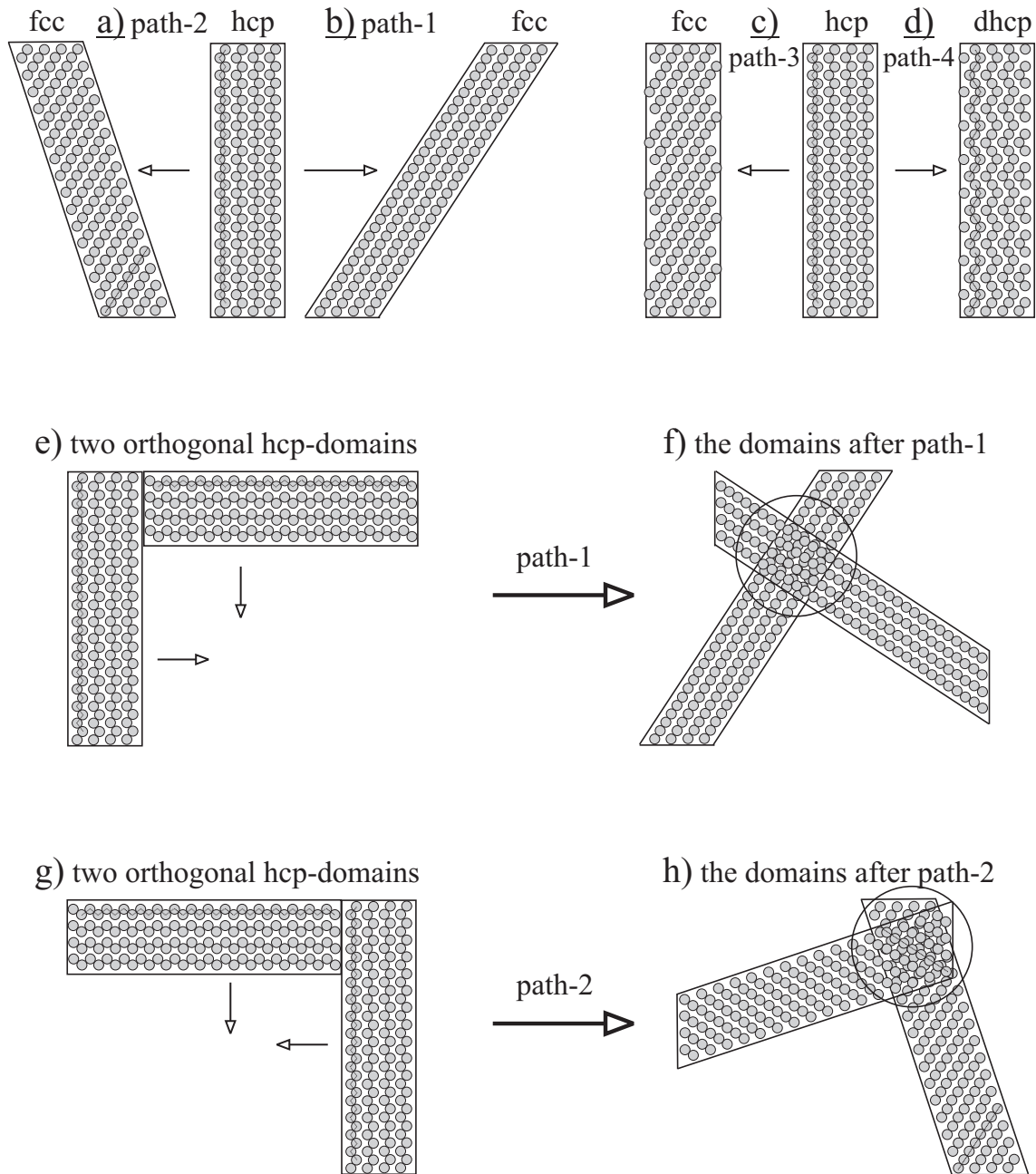
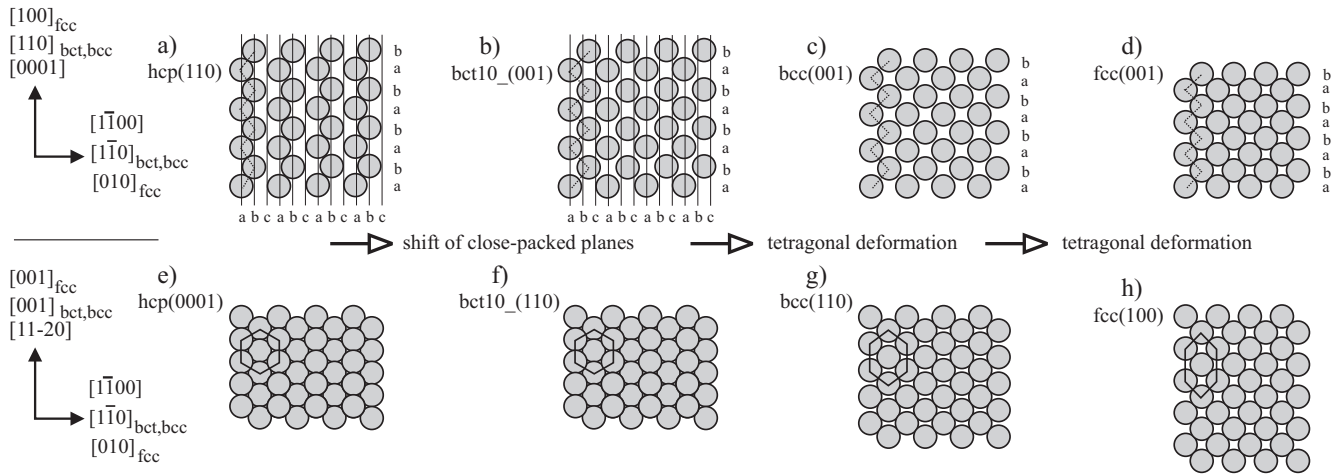


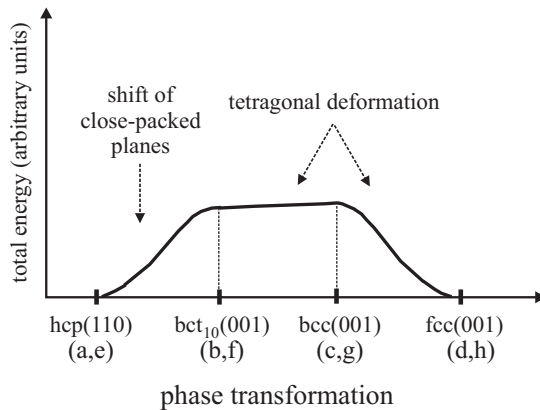
Figure 7.53: The effect on the domain shape of the transition paths presented in Fig.7.49. Path-2 (panel a) and Path-1 (panel b) are associated with a large mass transport (change of the domain shape), whereas in Path-3 (panel c) and in Path-4 (panel d) the mass transport is minute.

The particular structure of $(11\bar{2}0)$ oriented films displaying an orthogonal pattern of elongated rectangular domains has been observed by electron diffraction, electron microscopy and scanning tunneling microscopy. This structure persists even when the films are stripped off their substrates which has also been verified by experiments.

phase transformation $\text{hcp}(11\bar{2}0) \rightarrow \text{bct}_0(001) \rightarrow \text{bcc}(001) \rightarrow \text{fcc}(001)$; $\text{hcp}[0001] \parallel \text{bct}[110] \parallel \text{bcc}[110] \parallel \text{fcc}[100]$



i) Energy barriers in the crystal phase transformation from hcp(110) over bcc(001) into fcc(001) films



j) Influence of the substrate on the energy behavior in the hcp(110) || bcc(001) || fcc(001) phase transformation

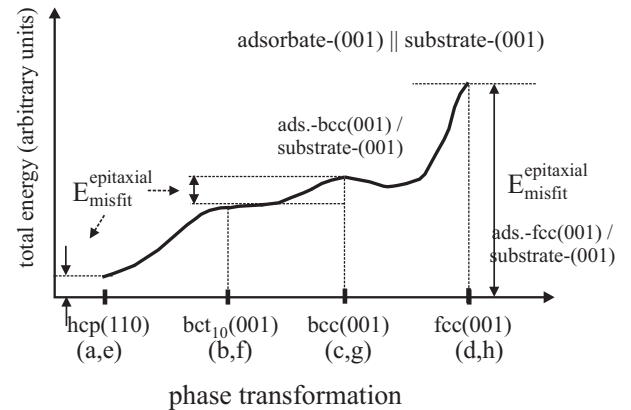


Figure 7.54: Schematic representation of the phase transition from $(11\bar{2}0)$ oriented hcp films (a,e) into (001) oriented fcc films (d,h) via the $\text{bct}_{10}(001)$ (b,f) and $\text{bcc}(001)$ (c,g) phases. The $\text{hcp}(0001)$, $\text{bct}_{10}(110)$, $\text{bcc}(110)$ and $\text{fcc}(100)$ atomic planes (panels e,f,g,h) lie perpendicular to the $\text{hcp}(11\bar{2}0)$, $\text{bct}_{10}(001)$, $\text{bcc}(001)$ and $\text{fcc}(001)$ atomic planes, respectively.

In panel (i) we have sketched the energy dependence along the transition path. In the $\text{hcp}(110)$ to $\text{bct}_{10}(001)$ phase transition, every second close-packed plane is shifted from its hcp-stacking array (see panel (a)) to a bct-stacking order (see panel (b)). In the course of this shift the total energy increases continuously from its hcp-value to that of the bct₁₀-structure. The bct₁₀ lattice (panels (b,f)) is further expanded then in the $[001]$ -direction (i.e. perpendicular to the (001) atomic plane) to form the $\text{bcc}(001)$ structure (panels (c,g)). Continuing the expansion while keeping the atomic volume constant one arrives at the $\text{fcc}(001)$ structure (panels (d,h)). This latter portion of the path constitutes a tetragonal deformation. Along the transformation path the atomic density in the (001) plane (b,c,d) increases as opposed to the (110) planes (f,g,h) where the atomic density decreases. In the course of the tetragonal deformation from bct₁₀ to the bcc, the energy increases only slightly, whereas in the tetragonal deformation from bcc to fcc the energy decreases continuously.

Panel (j) refers to the case of supported films. Here the substrate gives rise to an additional energy caused by the atomic misfit in the interface between the adsorbate and the substrate surface.

We emphasize again that the structural transformation discussed do not require a change of the domain-topology. The experimental data confirm that the observed fcc(001) phase of Cu is indeed aligned with its $[100]_{\text{fcc}}$ direction parallel to the $[1\bar{1}00]$ direction. As can be seen from panel (i) of Fig.7.54 the energy barrier to be overcome in the process of such a phase transformation is equal to the total-energy difference between the bcc phase and the hcp phase. It should be noticed, however, that inspite of this energy barrier being much lower compared to that of a hcp/fcc displacive phase transitions along Path-1 and Path-3 and despite the concomitant preservation of domain topology, it does not occur with thin films. The (001) oriented pseudomorphic-films display bct(001) order. One would surmise that they should easily overcome the low energy barrier to attain bcc structure and then transform into (001) oriented fcc films(see panel (i) of Fig.7.54). The experiments demonstrate that the occurrence of (001)order in the films is not the rule, but the exception. The latter could only be observed in thick Cu and Pd films deposited on W(001). The rational for this overall behavior has to be seen in the bad fit of the (001)fcc structure to the substrate surface. A bad adsorbate/substrate fit correlates with unfavorable on-top adsorption sites which cause the total energy of the epitaxial system to rise. It induces an additional epitaxial energy called ' $E_{\text{misfit}}^{\text{epitaxial}}$ ', in panel (j) of Fig.7.54 which becomes a non-neglegible part of the total energy of substrate-supported hcp(110), bcc(001) and fcc(001) films. Clearly, that energy increases as the misfit becomes larger. In the case of pseudomorphic bct films there is no additional epitaxial energy. For fcc(001)films the energy increase is largest because the atomic array involves more ad-atoms on-top of substrate atoms compared to films of hcp(110) or bcc(001) orientation. Also for hcp($11\bar{2}0$) films there is a small increase of the total energy caused by the misfit of the hcp($11\bar{2}0$) adsorbate plane to the substrate. The film reduces this energy by breaking up into rectangular islands. The rectangular domains are long in the direction of good fit direction and short in the direction where the fit is less good.

7.7 Explanation of the occurrence and the stability of the hexagonal phase modification in films grown on (001) oriented substrates.

We are now in the position to explain the development of ($11\bar{2}0$) oriented hexagonal phases in the films and, moreover, the experimental finding that films that started growing in the ($11\bar{2}0$)hcp phase modification do not build up their natural fcc lattice or fall back to this structure even when they are stripped-off their substrates.

7.7.1 The occurrence of the ($11\bar{2}0$) oriented lattice.

Because of the particular geometrical and energetical conditions causing pseudomorphic growth, our discussed epitaxial systems develop a (001) oriented bct structure where the atomic bct(110) planes lie perpendicular to the surface and are contracted in the direction of the surface normal. As has already been mentioned various times, the pseudomorphic growth prevails only up to the second ML and is followed then by a reordering of the primary bct(110) structure into a set of (hexagonal) close-packed atomic planes. This happens by merely shifting the atoms in the planes of close-packed symmetry from their on-bridge bct-array to a structure that is now characterized by hcp stacking. Since the required shifts are minute bct stacking and hcp-stacking may be considered very similar and quite different from fcc stacking. This will be discussed in more detail below, and we shall, in addition, point out that the adsorbate/substrate misfit will also have a crucial influence on the persistence of the hcp stacking.

As stated above, the pseudomorphic bct(001) film may be viewed as already consisting of a set of atomic planes in a ABAB... stacking mode that characterizes the hcp-phase (see panels (a,b) of Fig.7.55). Hence, a transition from the pseudomorphic bct(001) phase to the ($11\bar{2}0$) hcp phase does not require a change of the stacking mode of the atomic planes displaying close-packed symmetry.

One merely has to slide every second close-packed plane of the bct lattice, where certain atomic overlaps occur, into hcp-positions where atomic overlaps of this kind are absent. The required shift in the bct-[110] direction is given by $\frac{1}{2} \cdot b = \frac{1}{6}a\sqrt{3}$ (see Fig.7.46b,c,d, Fig.7.47b,c,e,f and Fig.7.55a,b). As one performs this shift the total energy drops continuously from its bct-value to that of the hcp-structure. This drop is plotted in the right part of panels (d,e) of Fig.7.55. It has in detail been determined by the group of Šob [131] whose calculations are based on ab initio Density Functional Theory (DFT).

If one wants to transform the pseudomorphic bct(001)structure into an atomic (110)fcc array by a shift of close-packed planes, one has to end up with a different stacking sequence. The transition can be viewed as a shift of close-packed planes from atomic on-bridge positions of the pseudomorphic bct-array to the three-fold positions of the atomic hcp-array (see e.g. panels (b,e) and (c,f) of Fig.7.47) which has to be followed then by an alteration of the stacking mode from hcp to fcc. This can be achieved by going along the three paths discussed in Fig.7.49. Each of these paths is associated with an energy barrier. Plots of the respective energy dependencies with the estimated barrier heights are given in the left part of panel (d) of Fig.7.55. The energy barrier along the Path-2 is small, much more smaller than the total-energy of the pseudomorphic bct phase. One would therefore expect that a displacive pseudomorphic-bct/fcc transformation along Path-2 should occur already at room temperature, as opposed to the experimental findings. This apparent contradiction is connected with the complete neglect of the substrate/adsorbate interface effects. A phase transformation in the film that requires a sizable material transport involves inevitably shifts of ad-atoms across on-top positions of the substrate surface which is associated with additional energy barriers in Path-1 and Path-2. (See panel (e) of Fig.7.55.) The overall barrier described by $E_{\text{substrate}}^{\text{barrier}}$ is higher than the total energy of the bct-phase (see panel (e) of Fig.7.55). Hence, on continuous deposition the originally occurring pseudomorphic (001) oriented bct films do not change over to their native fcc-structure but rather convert to (11 $\bar{2}$ 0) oriented hcp films with their close-packed planes lying perpendicular to the substrate-surface. The epitaxial relationship can be described as (11 $\bar{2}$ 0)_{film}, [0001] || (001)_{substrate}[110]_{bcc}. The additional energy $E_{\text{substrate}}^{\text{barrier}}$ is independent of the film thickness and the associated bonding mechanism is definitely short-range. As the adsorbate film becomes thicker this mechanism fades out and loses its influence on the film growth. One would expect then that films of this thickness now convert to their natural fcc-phase along the displacive phase transition Path-2, which, again, is not observed, even when these films are stripped off their substrates. The transition is strongly inhibited by the formation of rectangular domains imposed on the film by the (001) oriented substrate surface at the early stage of the film growth. The array of these domains displays the four-fold symmetry of the substrate.

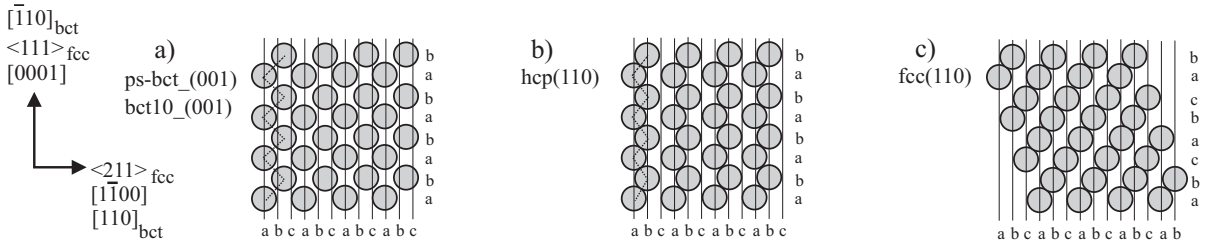
7.7.2 The stability of the (11 $\bar{2}$ 0) oriented hexagonal phase.

As the deposition proceeds the film thickens by simply enlarging the close-packed planes perpendicular to the substrate surface and keeping them solidly hcp-stacked parallel to the surface. More precisely, the stacking axis [0001] remains fixed parallel to the <110>-directions of the bcc(001) substrate surface. The set of close-packed planes displays a two-fold symmetry with respect to the surface normal as opposed to the substrate whose symmetry is four-fold. As a consequence, the misfit of the hcp-ordered atoms with respect to bct-ordered atoms in a plane parallel to the surface is on average smaller parallel to <110> than perpendicular to this direction. The film minimizes the associated misfit energy at an initial stage by breaking up into rectangular domains whose linear dimensions parallel to <110> are larger than in the perpendicular direction. Since the substrate surface exhibits two orthogonal, physically equivalent axes, the adsorbate forms two equivalent orthogonal sets of domains. The resulting domain topology is sketched in panel (a) of Fig.7.56. Its existence

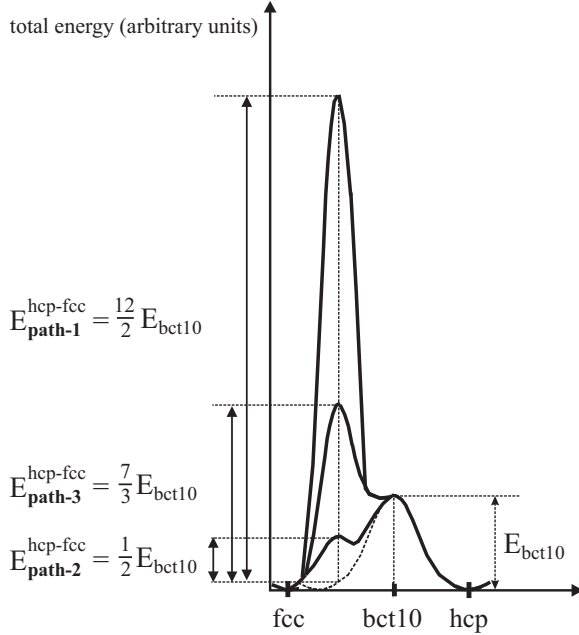
is clearly reflected in our RHEED-experiments and also in electron microscopy such as Reflection Electron Microscopy (REM) [78, 79], LEEM [137] and STM [81].

This domain-topology is the key to the understanding of the high stability of hcp-stacked films whose native structure is fcc. If the hcp-phase were to convert to the equilibrium fcc-structure along a transition path with the lowest energy-barrier described as Path-2, it would involve a large shift of the close-packed planes that would destroy the domain-topology of the $(11\bar{2}0)$ film. The importance of the orthogonal domain topology on the energy barriers in the displacive transition from hpc- to fcc-stacking is illustrated in panel (b) of Fig.7.56. The hcp/fcc phase transition that would preserve the domain-topology (Path-3) does not occur because it requires an energy barrier to be overcome that is higher than the film desorption energy.

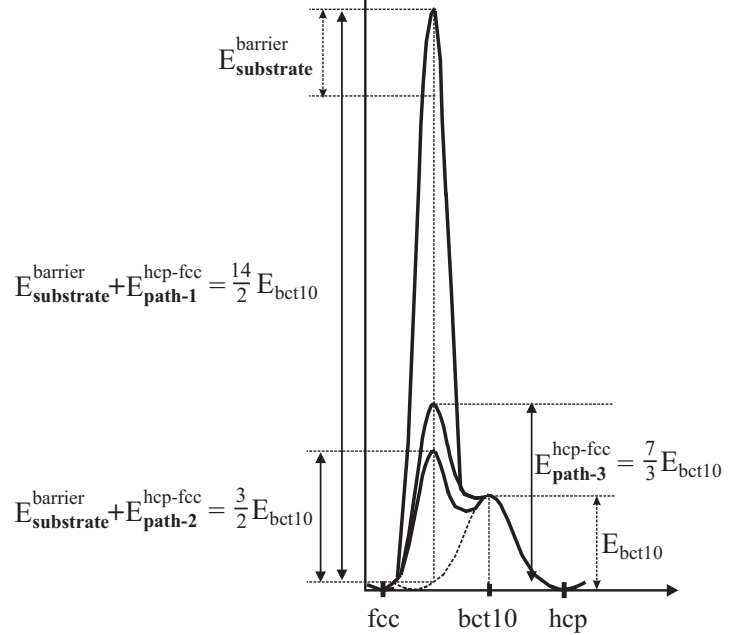
phase transformation fcc(111) || bct(110) || hcp(0001) by displacement of close-packed planes along fcc-<211> (bct-[110])



d) Energy barriers in the displacive phase transformation of free standing films



e) Influence of the substrate on the energy barriers in the displacive phase transformation of substrate supported films



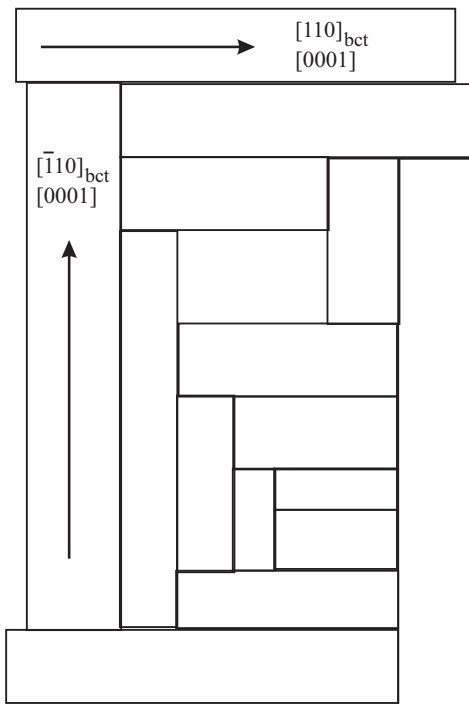
displacive phase transformation fcc(111) || bct(110) || hcp(0001) by shifts of close-packed planes along fcc-<211>

Figure 7.55: a) The (001) atomic plane of the bct₁₀(001) structure. The close-packed planes lie perpendicular to the surface. A small shift by $\frac{1}{2} \cdot b = \frac{1}{6}a\sqrt{3}$ in the bct-[110] direction of every second close-packed plane produces the (11 $\bar{2}$ 0) oriented hcp structure (panel (b)). By shifts of close-packed planes (as sketched in Fig.7.49) the hcp-atomic array can be transformed into the fcc structure (panel (c)). Hence, the displacive phase transformation from the (001) oriented (pseudomorphic) bct₁₀(001) film into the (110) oriented fcc structure can always be viewed as a displacive phase transformation from the bct₁₀(001) structure into an hcp-type atomic array, followed by a transformation into the fcc phase.

d,e) Predicted energy dependence along the displacive phase transition from the pseudomorphic bct(001) structure to an atomic hcp(11 $\bar{2}$ 0) array (right part of the panels) and from an atomic pseudomorphic bct-array to the fcc(110)structure (left part of the panels) for unsupported films (panel (d)) and for substrate supported films (e).

Energy barriers appear only with structural transitions that lead to fcc order. Without the influence of the substrate/adsorbate interface effect, i.e. for unsupported films (d), the energy barriers reflect the peculiarities of the transition from hcp- to fcc-stacking which occurs as one goes along Path-1, Path-2 and Path-3 (see Fig.7.49). With substrate supported films (e) the energy barriers along Path-1 and Path-3 are higher because the large shift of close-packed planes that is characteristic of Path-1 and Path-3 (see Fig.7.49 and Fig.7.53a,b) implies a shift of adsorbate atoms across atomic on-top positions of the substrate surface. As a result, the transition from the pseudomorphic-bct(001)structure to an atomic fcc(110) array by shifts of close-packed planes (panel (e)) is strongly inhibited.

a) rectangular-shaped orthogonal domains



b) Influence of the orthogonal domains on the energy barriers in free standing close-packed films

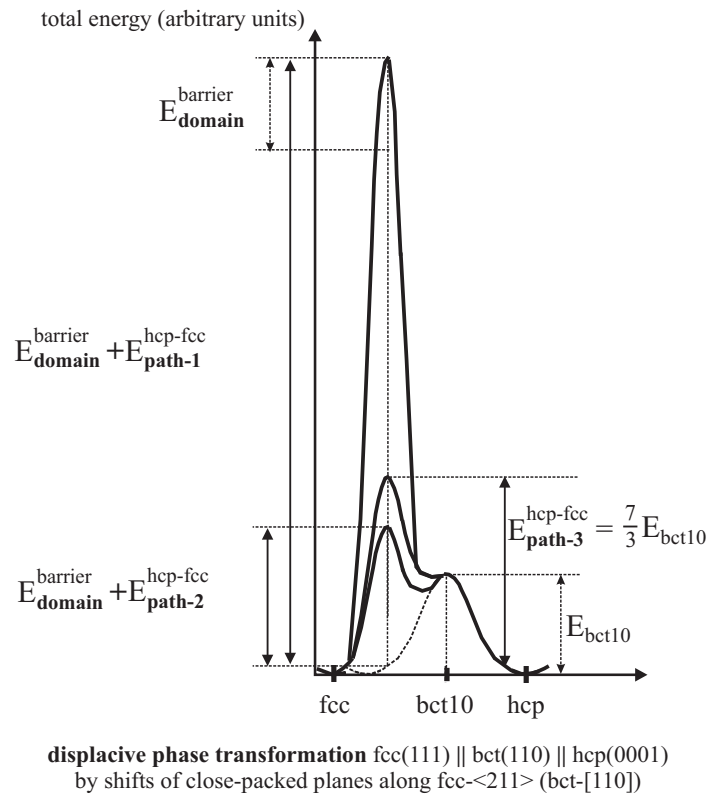


Figure 7.56: a) Two orthogonal sets of rectangular-shaped domains as they appear in the growth of hcp(11 $\bar{2}$ 0) films grown on cubic (001) substrates. The orthogonal sets of rectangular-shaped domains are associated with an additional energy barrier (see panel (b)) in the displacive phase transformations that do not preserve domain topology. This is the case of Path-1 and Path-2 because they are accompanied by a large material transport (see Fig.7.49 and Fig.7.53a,b). Path-1 possess already a large energy barrier. The concomitant energy barrier associated with Path-2 (which is the path of lowest energy barrier, see e.g. panel (d) of Fig.7.55) is so high that the displacive phase transformation does not occur even not in unsupported films. The hcp/fcc phase transition that would preserve the domain-topology (Path-3) do not occur because it requires to overcome a energy barrier that is higher than the film desorption energy.

7.8 The pseudomorphic-bct/fcc-transition

If the lattice parameter of the adsorbate is larger than that of the substrate, i.e. if $c/a \geq 1$, the growth behavior becomes qualitatively different from the situations discussed so far. In forming the bct-lattice the (110)-planes now undergo an expansion which means that the atoms of these planes are not compressed into hexagons any more. Perpendicular to the film the four-fold hollow sites are preserved. Shifts into three-fold hollow sites do not occur any more because the equilateral triangles are now missing. As a result, the pseudomorphic-growth continues until the strain energy in the bct (001)-film outweighs the energy gain that controls and causes epitaxial growth on a substrate.

In general, a pseudomorphic bct (001)-film grows up to 10 ML's before it starts forming its natural lattice. Because a ratio $c/a > 1$ correlates with an expansion of the bct (110)-planes compared to those of the natural bcc lattice, they further expand into the more densely packed fcc(100) planes as the growth proceeds. (See panels (a,b,d,e) of Fig.7.45). The films adopt an fcc (001)-structure if this constitutes the natural phase of the respective metal. An example of this kind is Au deposited on W(001) where one has $c/a=1.07$. We observed that after 10 pseudomorphic ML's Au forms its natural fcc (001)-phase. In the case of films whose generic lattice is hcp one expects, of course, hcp-growth beyond the pseudomorphic-regime even when $c/a \geq 1$. Films of Co metal represent an illustrative example that has well been studied by Wieldraaijer et al.[97] who deposited Co on Fe(001) buffer layers. It should be observed, however, that for $c/a \geq 1$, the in-plane packing of the developing Co ($11\bar{2}0$)-phase is less dense than that of the expanded bct (001)-plane of the pseudomorphic-phase.

7.9 Influence of the substrate lattice structure

Results on the stability of hexagonal films grown on bcc or fcc (001)-substrates, respectively, are compiled in Tables (6.11, 6.12). Ni on Fe(001) and Ni on Ag(001) have the same lattice misfit, but Ni on Fe(001) grows in an hcp-stacking mode as distinct from Ni on Ag(001) which leads to the formation of dhcp-films whose structure is closer to the natural fcc-structure of Ni. Cu on Fe(001) and Cu on Au(001) and on Ag(001) are also characterized by similar lattice misfits. But only Cu on Fe(001) develops an atomic hcp($11\bar{2}0$)-order rather than a dhcp($11\bar{2}0$)-structure [9]. This invites the conclusion that bcc (001)-substrates ensure a sound stabilization of hcp-growth with ($11\bar{2}0$)-orientation as distinct from fcc (001)-substrates, provided one is dealing with approximately the same lattice misfits. This difference in epitaxial behavior is mainly linked to stronger corrugation and reactivity of the bcc (001)-substrate surface compared to the respective surface of the fcc-lattice [18].

7.10 Effect of the electronic structure of the substrate surface

As already mentioned earlier, the initialization of a bcc- or hexagonal growth of fcc-type metals requires critically that the four-fold symmetric hollow sites of the bcc (001)-surface (see fig.4.27) are undamaged and unoccupied by impurities. We observed that even minute amounts of oxygen, carbon or sulphur on W(001) or Nb(001) prevent the growth of fcc-metals in a bcc- or hexagonal mode despite the fact that the contaminated Nb (001-)surface possesses an overwhelming number of uncontaminated adsorption sites with an unperturbed array of Nb-atoms. Obviously the change of the electronic structure of the surface around an impurity is far from being local but rather affects large portions of the non-contaminated surface [12, 19].

8 Doubling the pseudomorphic-range by imposing epitaxial constraints on both interfaces of substrate supported films

The substrate induced formation of a non-equilibrium pseudomorphic lattice possesses the largest potential of modifying the physical properties of the pertinent film metal, examples of which we have discussed in the preceding sections. With this experience in mind one feels tempted to think of ways to enlarge the thickness range where pseudomorphic-growth prevails. The ensuing sections will be devoted to this topic.

8.1 Deposition of an additional metal

There is a very interesting STM-study by Wieldraaijer et al. [96] on the epitaxy of Co on Fe(001) from which one may conclude that an enlargement of the primarily formed pseudomorphic-structure of a film by a partial re-crystallization of later grown material as the deposition proceeds, is very unlikely. And this may apply quite generally.

As previously explained, the hcp-lattice of Co on Fe(001) is formed with the $[1\bar{1}00]$ - and $[0001]$ -direction parallel to the, respectively, $[110]$ - and $[1\bar{1}0]$ -direction of the (001)-oriented substrate. The latter directions are physically equivalent as opposed to the two directions of the film. As a result, the film breaks up into islands that are long in the direction where the misfit to the substrate lattice is smaller on the average compared to the misfit in the perpendicular direction where the linear extension of the islands is correspondingly smaller. As indicated by the LEED-pattern, the formation of the hcp-structure starts at about 10 ML's which corresponds to a thickness of 1.4 nm. Below that thickness the Co-film is continuous. Once the islands have formed further deposition causes them to grow thicker, but also to enlarge their lateral extension thereby reducing the space between the islands. That space was primarily left open to reduce the misfit energy of the pseudomorphic-bct/hcp-interface. One might be led to conclude then that it would be energetically favorable to make the pseudomorphic-bct-film bottom thicker and thereby compensate for the increased misfit energy connected with the enlarged interface. However, since a thicker pseudomorphic-bct-film bottom does not benefit any more from the short-range substrate/adsorbate bond forces, the energy balance tips the re-crystallization in the other direction: the formerly grown pseudomorphic-Co-ML's adopt the $(11\bar{2}0)$ -structure. This has experimentally been demonstrated by Gazzadi et al. [74].

Nevertheless, there are only two principal possibilities for the enlargement of the pseudomorphic-range:

- 1) Suppression of the hcp($11\bar{2}0$)-growth
- 2) Conversion of already formed hcp-layers into pseudomorphic-layers by an additional epitaxial constraint.

8.2 Suppression of $(11\bar{2}0)$ -growth

Suppression of $(11\bar{2}0)$ -growth occurs in the presence of oxygen. Kim et al. [97] have demonstrated that a submonolayer coverage of oxygen can double the pseudomorphic-range of a Co-film growing on Fe(001). This has been substantiated by later studies [137, 138] which showed that oxygen obviously delays the onset of the bct/hcp-transition. It appears that the oxygen atoms impede the shift of the hexagon-type compressed bct(110)-planes into hcp-positions thereby preserving the pseudomorphic growth.

8.3 Conversion of already formed hcp-layers into pseudomorphic-layers

Though the conversion of already formed hcp-layers is unlikely, as discussed above, it actually occurs in multilayers where one deposits, for example, a bcc- or fcc(001)-film on top of an already grown hcp-film. Again, the Fe(001)/Co-system represents a well studied reference case. The strong Fe/Co bond force causes Co on an Fe(001) substrate to assume a pseudomorphic-bct-structure up to 10 ML's. Dekoster et al. [101] could show that an Fe-layer deposited on top of a thicker Co-film, that has already developed an hcp-structure, effects, surprisingly, an hcp/pseudomorphic-bct re-crystallization of the film up to 10 atomic layers. This could be evidenced by ex-situ nuclear magnetic resonance (NMR)-studies on Co/Fe-multilayers. In subsequent experiments [100] in which these sandwich-systems were prepared at temperatures higher than 500 K, the results could consistently be interpreted only by assuming that there is a partial diffusion of Fe into the Co-film thereby forming a Fe/Co-alloy that can obviously coexist with chemically pure pseudomorphic-bct Co. In similar studies by Wieldraaijer et al. [96] where the Co-film was alternatively capped by Fe, Cu or Al₂O₃ this interdiffusion could be avoided to a large extent. In the following we shall discuss the results of these authors along the lines of our analysis in the preceding sections.

8.3.1 The Fe/Co/Fe(001)-system

As has been shown by Valeri et al. [139, 140], Fe grows on top of hcp(11 $\bar{2}$ 0) Co in the (001) bcc-orientation with a small out-of-plane contraction of 3% after deposition of 3 ML's. This is not surprising if one applies arguments that are familiar from previous considerations:

If Fe were to grow pseudomorphically on Co(11 $\bar{2}$ 0), the Fe-atoms would be forced into a (11 $\bar{2}$ 0) in-plane array. Moreover, the Fe-atoms in planes perpendicular to this surface would occupy the three-fold hollow sites of the next equivalent hcp(0001)plane. However, since the native structure of Fe is bcc, it naturally tends to form bcc(110)-planes in this direction of growth because these most densely packed planes are also the most stable ones and the out-of-plane influence of the topmost Co-plane is shortrange. Hence, as the growth proceeds the Fe-atoms occupy the rhombic hollow sites of the bcc(110)-planes rather than the mentioned three-fold sites of a continued pseudomorphic-hcp lattice where the in-plane array of atoms would form a c(2x2) superstructure with respect to a bcc(001)-surface. Because of the departure from pseudomorphic-hcp growth the in-plane symmetry is now fourfold. If the thickness of the Fe-film is large enough (> 18 ML's) it attains the properties of a macroscopic material (as the Co-film substrate) and may now, in turn, cause the topmost layers of the Co-film to re-crystallize into a pseudomorphic-bct structure whose lateral atomic array is dictated by the Fe bcc(001)-surface. There is one feature of this process that deserves additional consideration. The original density of Co-atoms in the hcp(11 $\bar{2}$ 0)-plane is by 6.6% lower than that of pseudomorphic Co-films on Fe(001) (s. Table 6.7 for Co/Fe(001)). Hence, as one caps the originally open hcp(11 $\bar{2}$ 0)-surface of a Co-film with a thick Fe-film, the lateral Co-lattice is forced to shrink. As the near-surface portion of the Co-film tends to conserve its atomic volume, the out-of-plane lattice expands from the close-packed hcp-planes to form the rectangular bcc(t)(110)- planes that are associated with a tetragonal c/a ratio of 0.944 (s. Table 6.7 for Co/Fe(001)). As a consequence, the three-fold hollow sites of the hexagons move into the rhombic hollow sites of the bcc(110)-planes, which means that the Co-atoms attain the pseudomorphic-positions of the bcc(001)-lattice.

8.3.2 The Cu/Co/Fe(001)-system

As opposed to the previous case, NMR-studies on the effect of capping hcp(11 $\bar{2}$ 0) Co/Fe(001)-films with Cu do not indicate an influence on the film's pseudomorphic-range on a scale of interest. To the best of our knowledge, the structure of those Cu-films has not been determined as yet. To make an educated guess on their structure and orientation we shall resort to material from well studied

epitaxial Cu-systems.

The mesh length of the square lattice displayed by an fcc(001)Cu-surface is 2.55 \AA . This is identical with the distance of next-nearest neighbors in the bulk, and it is only by 2% larger than the next-nearest neighbor distance in Co metal. One would expect then that Co-films grown on Cu(001) attain a pseudomorphic-fcc(t)(001)-structure which is, in fact, substantiated by numerous detailed studies [141]. Metallic bond and geometric misfit considerations give additional support to this growth behavior of Co on Cu(001) [141, 7], and it should also apply to Ni as a substrate [142]. Based on this experience, one would surmise that the topmost layers of a Co/Fe(001)-film should tend to attain an fcc-structure on exposure to a sufficiently thick capping fcc(001)Cu-film. The reason for this not going to happen is very likely connected with the fact that the near-interface portions of the Cu-film are not fcc-ordered but rather have bct(001)- or hcp($11\bar{2}0$)-structure, as we shall explain below.

We first consider a sufficiently thin Co-film on Fe(001), still displaying a bct(001)- structure. The length of the unit cell of the top layer is about 2.83 \AA [96] which represents a rather open surface with respect to an fcc(001)Cu-surface where the corresponding mesh length is 2.55 \AA . Therefore, on capping the bct(001)Co-surface by a Cu-blanket, the latter film would very likely not grow an fcc(001)-lattice but rather form a pseudomorphic-bct(001)-structure. This may be concluded from numerous experimental results, including surface analysis by atom-resolved STM [113, 118, 143, 3], referring to the deposition of Cu on (001)-surfaces with mesh lengths of 2.89 \AA , 2.88 \AA , 2.87 \AA , 2.77 \AA and 2.75 \AA which correspond to the surfaces of Ag [76, 113], Au [118], Fe [8, 120], Pd [3] and Pt [143], respectively. Supposedly, the presence of a bct(001)Cu-blanket will not affect the stability of the underlying bct(001)Co-film as long as the thickness of the latter is sizably larger.

When Cu is deposited on Fe(001) or on W(001) the Cu-film develops after initial bct(001) growth a ($11\bar{2}0$)-oriented hcp-phase. As the misfit of the latter with respect to a hcp($11\bar{2}0$)Co-surface is much less compared to that of a Fe(001)-surface, one is justified in assuming that Cu will grow on Co($11\bar{2}0$) by forming a ($11\bar{2}0$)-oriented hcp-phase. It appears to be likely, therefore, that a Cu-blanket of this structure will not significantly affect the lattice stability of the ($11\bar{2}0$)-structured portion of the Co-film grown on Fe(001). One might expect that the stability of a bct(001)Co-film of x \AA thickness covered by, for example, a 30 \AA thick bct(001)Cu-film should be similar to the stability of a bct(001)Co-film of $x+30$ \AA thickness. Hence, capping a Co-film by Cu will likely reduce the extent of its pseudomorphic-bct(001)-constituent. This seems to be confirmed by NMR-results on Co-films of about 10 ML's which should exhibit a bct(001)-structure. Once they are capped by a thick Cu-film of 30 \AA , the observed broadening of the NMR-peak may be attributed to the additional occurrence of hcp-ordered Co [96]. In conclusion it can be stated that the effect of a Cu-overlayer is profoundly different from that of an Fe-overlayer.

8.3.3 The Alumina/Co/Fe(001)-system

Covering a Co/Fe(001)-film of 20 \AA thickness with alumina (Al_2O_3) gives rise to a surprising NMR-spectrum shown in Fig.5 of the very exhaustive study by Wieldraaijer et al. [96]. The system stands out by a bcc Co NMR-line of unsurpassed clarity, merely accompanied by an irreducible intensity of 10 to 15% integral contribution caused by the two interfaces. The spectral feature of this contribution to the NMR-signal is characterized by its independence of aging processes and of the film thickness (up to 20 \AA). To understand the peculiarity of this system one has to analyze the formation of the Al_2O_3 -layer in more detail.

The alumina coverage was obtained by first depositing Al by sputtering. This technique creates Al atoms with a considerably higher kinetic energy compared to those effusing from an evaporator. One would expect that the Al-atoms retain a sizable fraction of that energy after deposition and are therefore sufficiently mobile to form their native fcc-lattice. This is, in fact, what happens. As

follows from inspection of the lattice parameters and the geometry, the fcc(001)-plane of Al matches perfectly the respective properties of the Co/Fe(001)-surface. As a result, a thick fcc(001)-film of Al acts on the top of the Co-layers much like the Fe(001)-substrate and causes a pseudomorphic bct-restructuring of the topmost Co-layers. At this stage, some intermixture of Co and Al is likely to occur [144]. However, as Egelhoff Jr. et al. [144] have demonstrated, oxidation of the Al/Co-sample offers a possibility to reduce this mutual penetration. Due to the higher affinity of oxygen to Al compared to that of Co [145], the oxygen forms bonds to Al rather than to Co whereby an alumina layer is built up on top of Co with the latter remaining chemically pure. The process is carried out by plasma oxidation which ensures the presence of atomic oxygen at the early stage of the Al₂O₃-formation. This, in turn, ensures the persistence of the bct-structure of the topmost Co-layers as oxygen effects decatalyzation rather than promotion of the bcc/hcp-transformation. This has already pointed out earlier.

The remarkable property of Al₂O₃ as a blanket material that stabilizes the non-equilibrium bcc-structure of Co becomes also conspicuous with Co nano-particles that have been encapsulated by a thin amorphous film of Al₂O₃. Alumina wrapping of nano-particles that exist in a bcc-structure only up to a diameter of 220 Å can lead to an increase of this diameter up to 1000 Å [146, 147].

We may summarize this section by stating that the linear dimensions of bcc-Co as a film or a spheroid can be sizably enlarged by an alumina overlayer.

8.4 Phase stability diagrams

As to whether or not a doubling of the pseudomorphic-range occurs on covering a Co/substrate-system depends on the balance of the pseudomorphic-formation energy vs. the gain in interface binding energy between the Co metal and overlayer metal. This has been studied by Dregia, Banerjee and Fraser [148, 149, 150, 151, 152, 153] in terms of thermodynamic principles on the basis of phase stability diagrams. Let ΔG stand for the volumetric free energy difference between the pseudomorphic and the bulk phase of the film, $\Delta\gamma$ denote the corresponding reduction of interfacial energy in the two states and t_{cov} stand for the thickness of the film, the thickness limit of pseudomorphic-growth in alternating (multi-) layers is given by $\Delta G \cdot t_{cov} + 2\Delta\gamma = 0$. One can easily extend this equation to uncovered films: $\Delta G \cdot t_{non-cov} + \Delta\gamma = 0$ where $t_{non-cov}$ is the thickness of the uncovered film. Obviously, the two equations yield: $t_{cov} = 2 \cdot t_{non-cov}$. Results obtained on Co/Cu(111) [154], Co/Cr(001) [89, 90, 155] and Co/Au(001) [82] multilayers which also show an enlarged pseudomorphic-range compared to uncovered Co-films, conform to the above considerations.

The examples discussed so far bear evidence of the fact that in films of transition metals the thickness range of their non-equilibrium structure will likely be doubled (or at least be enlarged) if they form a periodic array intercalated by films of appropriately chosen other materials.

An interesting counter-example are pseudomorphic-fct(001) Co-films grown on Cu(001). If one caps these films by Au-layers, the thickness of the pseudomorphic-range is reduced. This can be traced back to the fcc(111)- growth of the Au-overlayer which have a large misfit to the fct(001) top-layers of Co. As a consequence, the overlayer causes these Co-layers to adopt their structure accordingly. This has been shown by Heinrich [157].

9 Conclusion

The current work is devoted to the growth of late transition metals and noble metals as they are vapor deposited on cubic (001)substrates. Many adsorbate films develop a centered electron diffraction pattern after the first pseudomorphic monolayers. We could explain this centered pattern as arising from a $(11\bar{2}0)$ oriented hexagonal close-packed film structure. That means that the close-packed layers of the film stand perpendicular to the surface with their stacking axis $[0001]$ lying in the surface plane of the substrate. The geometry of the epitaxial locking that results from minimizing the total energy (i.e. from the tendency of the epitaxial system to achieve lowest total energy) can symbolically be characterized by $(11\bar{2}0)_{film}, [0001] \parallel (001)_{substrate}, <110>_{bcc}$ when the substrate possesses bcc-symmetry and by $(11\bar{2}0)_{film}, [0001] \parallel (001)_{substrate}, <100>_{fcc}$ when one is dealing with an fcc-substrate.

Contrary to what one would expect, we found that the occurrence of the hcp($11\bar{2}0$)-film is crucially tied to an optimal interfacial fit of the film parallel to its $[1\bar{1}00]$ -direction, that is, perpendicular to the stacking axis rather than parallel to it. This growth geometry can be understood if one takes note of the fact that it implies a preceding pseudomorphic growth which strongly influences the way atoms are arranged perpendicular to the surface as the interaction with the substrate fades out.

The pseudomorphic-growth constitutes a well known phenomenon often used as a modern technique to produce metastable phases. It is characterized by the property of the ad-metal to adopt the lateral periodicity of the substrate. In general, the side length of the lateral unit cells of the ad-metal and the substrate will be different so that a forced adaptation of the adlayer unit cell introduces a strain in the adlayer plane. (We defer discussing the alternative of building up stress to the end of this section.) As the atoms of a metal tend to conserve their volume under unilateral strain or stress, the strain (or stress) parallel to the surface gives rise to forces perpendicular to it as a consequence of which the structure of a two-layer pseudomorphic-film becomes more or less tetragonal (fct or bct).

For tetragonal ratios $c/a < 1$ the pseudomorphic (001)-film is compressed perpendicular to the surface compared to a bcc(001)-film. In the centered rectangular bct(110)-planes, which are perpendicular to the substrate surface, the atomic array becomes thereby identical to that of the close-packed (hexagonal) planes of the native fcc-phase. (In an fcc-stacking mode these planes constitute the (111)-planes, in a non-fcc stacking mode the (0001)-planes.) However, as the film forms its first layers parallel to the substrate surface, the required stacking, which leads to a three-fold symmetry around the stacking axis, cannot take place because the planes are still stacked in the $<110>_{bcc}$ -direction dictated by the bct-symmetry, and hence the symmetry around this axis is four-fold. But one has to bear in mind that of the planes under discussion only a few sites are actually occupied in a film of two monolayers. As the film starts building up its third layer, half of the newly arriving atoms are no longer placed into the regular positions of the bct(110)-planes. Rather they are shifted within every second bct(110)-plane into energetically more favorable places such that they now occupy positions representing hcp-type hollow sites of the two unmodified adjacent planes. This requires only a small shift in the $<1\bar{1}0>$ -direction. In continuing the close-packing array within each plane, the film now attains a regular hcp-structure with a stacking axis in the bct $<110>$ -direction parallel to the substrate surface and parallel to the $<0001>$ -direction of a hcp-lattice. With respect to this lattice the normal direction of the substrate surface is now characterized by $<11\bar{2}0>$.

The departure from a regular bct-array of the arriving atoms within every second (110)-plane is primarily associated with an energy increase which is, however, outweighed by the energy gain in placing the shifted atoms into the favorable hollow sites of the unmodified adjacent planes. This applies similarly to the formation of a dhcp-structure. If the newly arriving atoms were to form an fcc-lattice with a stacking axis in the bct $<110>$ -direction, only one sixth of them would occupy the regular positions of the bct(110)-planes. Though the energy gain per atom by placing all new atoms

into favorable hollow site positions would be the same as in the previous case, the shift energy per atom would be about 68% higher because only every sixth plane would remain unmodified. For this reason the build-up of hcp-stacked close-packed planes at the very early stage is strongly favored over an fcc-stacking. Once the formation of the hcp-array has started, the favorable adsorption sites for a further build-up of the film that ensure a continuous close-packing in the planes perpendicular to the surface and a mutual optimal planar fit, remain to be sites of the hcp-lattice. If the lattice, at a somewhat later stage, would try to convert into an fcc-structure, it has to overcome a considerable energy barrier connected with sliding atoms over on-top positions of an already deposited layer. As a consequence, the films maintain their non-fcc-stacking over a large thickness range and even when the films are later stripped off their substrates.

The substrate surface possesses a four-fold symmetry whereas the hcp($11\bar{2}0$)-adsorbate is only two-fold symmetric with respect to the surface normal. Hence, at the common interface the adsorbate sees a small misfit on the average in one direction parallel to one of the surface symmetry axis and a large mean misfit in the direction of the surface symmetry axis perpendicular to the other. As a consequence, the adsorbate grows by forming rectangular domains, short in the direction of large mean misfit, long in the orthogonal direction. Because of the two equivalent symmetry axis of the substrate surface the adsorbate develops two sets of rectangular domains. An hcp/fcc-phase transition would change the shape of the domains considerably and would hence require atomic transport over distances that are large compared to interatomic spacings. This is tantamount to a high energy barrier strongly inhibiting this transition as long as the film thickness is below a certain value. Beyond that threshold thickness the films finally develop their native fcc-structure. This is achieved by reversing the initializing process of generating the hcp-structure on top of the pseudomorphic-bct(001)-film. Once the bct-structure has formed, the lattice can smoothly be transformed into the bcc(001)-structure and finally, by a tetragonal distortion (along the “Bain-Path”), into an fcc-lattice in which the energy per atom is lower than that in the preceding hcp-phase. The energy to be overcome along this transition path is obviously large as long as the thickness of the film remains below a certain relatively large value. As the film grows further, there will also be a growing number of lattice defects that shift the total energy of the film above its ideal structure value. By reducing the number of lattice defects which amounts to moving individual atoms, the ideal transition path barrier desintegrates into several considerably smaller barriers that can be overcome by thermal activation in the deposition process. We have observed a hcp/fcc-phase transition of this kind with Cu- and Pd-films on Nb(001).

The energy barrier for a hcp/dhcp-transition is low. In addition, it preserves the shape of the domains. Not surprisingly, hence, the transition actually occurs. Double-hcp stacking in films is observed with metals that possess a high stacking-fault energy like Rh and Pd. However, both kinds of stackings can occur with the same metal, depending on the substrate/adsorbate bond strength. Ni- represents a good example: it grows as an hcp($11\bar{2}0$)-film on Fe(001), but forms a dhcp($11\bar{2}0$)-film on Au(001) because of the weaker Ni/Au-bonds.

If $c/a > 1$, the bct(110)-planes are stretched perpendicular to the substrate surface compared to the corresponding bct(001)-planes. In this case it is no longer possible to slightly shift newly arriving atoms out of their regular positions in every second bct(110)-plane to seed positions of hcp-planes with the same stacking axis as the bct(110)-planes. Therefore the pseudomorphic-bct(001)-growth persists up to 10 monolayers in the majority of cases that have been studied in the current work. Beyond that threshold the films fall back onto growing in their equilibrium structure.

Films like those of Co whose natural lattice structure is hcp take 10 monolayers to develop their native hcp-structure with a ($11\bar{2}0$)-orientation. Other films of fcc-type metals regain their fcc-equilibrium structure in a (001)-orientation. This constitutes a direct consequence of the tetragonal ratio being larger than unity. The bct(110)-planes must only be stretched a little further (along the “Bain-Path”)

to attain the atomic array and dimensions of fcc(100)-planes whose four-fold symmetry axis is parallel to the $\langle 110 \rangle$ -direction of the bct-lattice.

The thickness-limit of pseudomorphic-films can be extended by suitable surfactants or, in superlattices, by imposing a suitable epitaxial constraint on both interfaces of a sandwiched film.

References

- [1] B. T. Jonker, J. J. Krebs, and G. A. Prinz, *Phys. Rev. B* **39** (1989) 1399
- [2] S. Andrieu, F. Lahatra Razafindramisa, E. Snoeck, H. Renevier, A. Barbara, J. M. Tonnerre, M. Brunel, and M. Piecuch, *Phys. Rev. B* **52** (1995) 9938, and references therein.
- [3] E. Hahn, E. Kampshoff, N. Wälchli, and K. Kern, *Phys. Rev. Lett.* **74** (1995) 1803, and references therein.
- [4] P. Allippi, P. M. Marcus, and M. Scheffler, *Phys. Rev. Lett.* **78** (1997) 3892, and references therein.
- [5] H. Wormeester, E. Hüger, and E. Bauer, *Phys. Rev. B* **57** (1998) 10120
- [6] E. Hüger, and K. Osuch, *Europhys. Lett.* **71** (2005) 276
- [7] E. Hüger, and K. Osuch, *Nature* **436** (2005) 606. *Research Highlights*.
- [8] E. Hüger, and K. Osuch, in preparation.
- [9] E. Hueger, H. Wormeester, and E. Bauer, *Surf. Sci.* **438** (1999) 185
- [10] H. Wormeester, E. Hüger, and E. Bauer, *Phys. Rev. Lett.* **77** (1996) 1540
- [11] H. Wormeester, E. Hüger, and E. Bauer, *Phys. Rev. B* **54** (1996) 17108
- [12] H. Wormeester, E. Hüger, and E. Bauer, *Phys. Rev. Lett.* **81** (1998) 854
- [13] E. Hüger, and K. Osuch, *Europhys. Lett.* **63** (2003) 90
- [14] E. Hüger, and K. Osuch, *Solid State Commun.* **132** (2004) 97
- [15] E. Hüger, and K. Osuch, *Phys. Rev. B* **68** (2003) 205425
- [16] E. Hüger, and K. Osuch, *Eur. Phys. J. B* **37** (2004) 149
- [17] E. Hüger, and K. Osuch, *J. Electron. Spectrosc. and Relat. Phenom.* **141** (2004) 13
- [18] E. Hüger, H. Wormeester, and K. Osuch, *Surf. Sci.* **580** (2005) 173
- [19] E. Hüger, and K. Osuch, *Thin Solid Films* **488** (2005) 291
- [20] E. Hüger, and K. Osuch, *Phys. Rev. B* **72** (2005) 085432
- [21] E. Hüger, and K. Osuch, *Solid State Commun.* **131** (2004) 175
- [22] E. Hüger, and K. Osuch, *Eur. Phys. J. B* **44** (2005) 145
- [23] V. L. Moruzzi, and P. M. Marcus, in *Handbook of Ferromagnetic Materials*, edited by K. H. J. Buschow (Elsevier, Amsterdam, 1993), Vol. 7, p. 97.
- [24] M. Černý, J. Pokluda, M. Šob, M. Friák, and P. Šandera, *Phys. Rev. B* **67** (2003) 035116
- [25] D. Hobbs, J. Hafner, and D. Spisak, *Phys. Rev. B* **68** (2003) 014407
- [26] D. Hobbs, J. Hafner, and D. Spisak, *Phys. Rev. B* **68** (2003) 014408

- [27] J. Goniakowski, and M. Podgorny, Phys. Rev. B **44** (1991) 12348; G. Cort, R. D. Taylor, J. O. Willis, J. Appl. Phys. **53** (1982) 2064
- [28] V. L. Moruzzi, P. M. Marcus, K. Schwarz, and P. Mohn, Phys. Rev. B **34** (1986) 1784; V. L. Moruzzi, Phys. Rev. Lett. **57** (1986) 2211
- [29] The calculations were performed within the framework of density functional theory (DFT), using the full potential linearised plane wave (FLAPW) method and the LSDA approximation [30, 31] as implemented in the Wien2k package [32]. First scalar relativistic calculations were carried out and subsequently spin-orbit coupling was included in a second variation step [32]. The calculations were performed at 560 k-points in the irreducible wedge of the Brillouin zone (IBZ). The optimum lattice constants of the Pd and Rh structures studied were determined by minimising the total energy as a function of the lattice constant. Convergence of the self-consistent calculations was assumed when the charge distance defined as $\int |\rho_n(r) - \rho_{n-1}(r)| d^3r$, where ρ is the electronic charge density and n is the iteration number, was smaller than $1 \times 10^{-4}e$ in three consecutive iterations.
- [30] P. Hohenberg, and W. Kohn, Phys. Rev **136** (1964) B864
- [31] W. Kohn, and L. J. Sham, Phys. Rev. **140** (1964) A1133
- [32] P. Blaha, K. Schwarz, G. K. H Madsen, D. Kvasnicka, and J. Luitz, WIEN2k, An Augmented Plane Wave + Local Orbitals Program for Calculating Crystal Properties (Karlheinz Schwarz, Techn. Universität Wien, Austria), 2001. ISBN 3-9501031-1-2
- [33] Takeuchi Noboru, C. T. Chan, and K. M. Ho, Phys. Rev. B **40** (1989) 1565
- [34] Self-consistent DFT calculations carried out without spin-orbit coupling give larger magnetic moments than those in which spin-orbit coupling is included, e.g. they give the magnetic moment of $0.34 \mu_B$ (instead of $0.16 \mu_B$) for hcp-Pd. This is qualitatively not surprising as the spin-orbit coupling causes more spin-flips from the majority spins than from the minority spins, thereby reducing the difference between up- and down-spins.
- [35] The same apparatus was described by Lilienkamp [36] and Knoppe [37] in detail (see also [38]).
- [36] G. Lilienkamp, thesis, (TU-Clausthal, 1990)
- [37] H. Knoppe, thesis, (TU-Clausthal, 1995)
- [38] ESCALAB-MKII –specification and operating manual– Vacuum Generators Scientific, (Sussex, 1984)
- [39] *Reflection High-Energy Diffraction and Reflection Electron Imaging of Surfaces*, Edt. P. K. Larson, and P. J. Dobson, NATO ASI Series B **188**, (Plenum, New York, 1988)
- [40] J. E. Mahan, K. M. Geib, G. Y. Robinson, and R. G. Long, J. Vac. Sci. Technol. A **8**, 3692 (1990)
- [41] R. Stalder, C. Schwarz, H. Sirringhaus, and H. von Känel, Surf. Sci. **271**, 355 (1992)
- [42] A. S. Arrott in *Ultrathin magnetic structures I*, Eds. J. A. C. Bland and B. Heinrich (Springer, Berlin, 1994), ISBN 3-540-57407-7

- [43] M. A. Van Hove, W. H. Weinberg, C.-M. Chan: *Experiment, Theory and Surface Structure determination*, (Springer, Berlin, 1986)
- [44] K. Heinz, *Prog. Surf. Sci.* **27** (1988) 239
- [45] C. Argile, and G. E. Rhead, *Surf. Sci. Rep.* **10** (1989) 277
- [46] S. Hüfner, *Photoelectron Spectroscopy*, (Springer, Berlin, 1995)
- [47] H. Eckardt, and L. Fritsche, *J. Phys. F* **16** (1986) 1731
- [48] L. Fritsche in: *Density Functional Theory*, E. K. U. Gross and R. M. Dreizler (eds.), Plenum Press, New York (1995), NATO ASI-Series
- [49] L. Fritsche and Y. M. Gu, *Phys. Rev. B* **48** (1993) 4250
- [50] Lilienkamp [36], Kolaczkiwicz and Bauer [51] have measured the exchange splitting of 4.5 eV between the majority-spin and minority-spin 4f-bands of Gd by using low energy electron loss spectroscopy (EELS). (The experimental data shows that this energy is associated with a transition of a majority-spin electron into the corresponding minority-spin 4f band.) Because the 4f minority-spin states of Gd are practically empty, the 4f majority-spin states cannot lie at larger binding energies than 4.5 eV below the Fermi-level, in accordance with LSD-calculations including spin-orbit coupling [52]. On the other hand, photoelectron spectroscopy (PES), in particular XPS, detects 4f-electrons at an energy of 8 eV below the Fermi-level. Thus, in the case of 4f-levels of Gd the PES-measured energy of the (occupied) 4f-level differs by 3.5 eV from the binding energy of the (spin-majority) 4f states. One has to bear in mind, however, that in XPS-experiments one creates empty local 4f states which are sizably lower in energy than 4f-band states. (This applies to empty local states in insulators and semiconductors as well.) Hence, one is dealing here with a final state effect which represents a mechanism completely different from interband transitions observed with EELS. In addition, the energy of the local empty 4f states depends on the screening which is time-dependent. Therefore, one obtains a dependence of this energy on the kinetic energy of the photo-electrons. Thus, UPS-photoelectrons would yield still another energy for this kind of local 4f-state.
- [51] E. Bauer, and J. Kolaczkiwicz, *phys. stat. sol. b* **131** (1985) 699
- [52] J. Sticht, and J. Kübler, *Solid State Commun.* **53** (1985) 529
- [53] S.A. Chambers, *Adv. Phys.* **40** (1991) 357
- [54] D. P. Woodruff, and A. M. Bradshaw, *Rep. Prog. Phys.* **57** (1994) 1029; D. P. Woodruff, *Surf. Sci.* **299/300** (1994) 183
- [55] W. F. Egelhoff, Jr., in *Ultrathin magnetic structures I*, Eds. J. A. C. Bland and B. Heinrich (Springer, Berlin, 1994), ISBN 3-540-57407-7
- [56] E. Bauer, *Surf. Sci.* **7** (1967) 351
- [57] E. Bauer, private communication
- [58] Gmelin's handbook of inorganic and organometallic chemistry, Vol. **49 B1**, (Verlag Chemie, Berlin, 1925-)
- [59] D.-A. Luh et al, *Science* **292** (2001) 113; V. Yeh et al, *Phys. Rev. Lett.* **85** (2000) 5158; J.-H. Cho et al, *Phys. Rev. Lett.* **80** (1998) 3582

- [60] Th. Duden, thesis, (TU-Clausthal, 1996); Th. Duden, R. Zdyb, M. S. Altman, and E. Bauer, *Surf. Sci.* **480** (2001) 145
- [61] The work function measurements reported by Pavlovska and Bauer [62] were performed with a cylindrical W crystal in a separate system. The axis of this cylindrical crystal was in the $[1\bar{1}0]$ direction. Thereby the surface of the cylinder displayed all planes within this zone, in particular the (110) and (001) planes. During deposition the crystal was rotated at a constant velocity while at the same time the work function difference ($\Delta\phi$) was measured with a collimated electron beam. The system was also equipped with a LEED and CMA system, so that $\Delta\phi$ could be correlated with structure and coverage.
- [62] A. Pavlovska and E. Bauer, unpublished
- [63] E. Bauer, H. Poppa, G. Todd, and P. R. Davis, *J. Appl. Phys.* **48** (1977) 3773
- [64] E. Bauer, H. Poppa, G. Todd, and F. Bonczek, *J. Appl. Phys.* **45** (1974) 5164
- [65] J. Kołaczkiwicz and E. Bauer, *Surf. Sci.* **155** (1985) 700
- [66] J. Kołaczkiwicz and E. Bauer, *Surf. Sci.* **160** (1985) 1
- [67] S. Prigge, H. Roux, and E. Bauer, *Surf. Sci.* **107** (1981) 101
- [68] In contrast to LEED, the diffraction process in RHEED is in general not a true reflection, i.e. the scattered beam does in general not leave the scatterer from the same surface at which the incident beam entered. Most surfaces are rough and the diffraction pattern is produced in transmission through the surface asperities. However, in the case of flat surfaces, the RHEED beams do leave in the scatterer from the same surface which the incoming beam impinges. Therefore, the pattern produced by such RHEED beams were called also 'true' RHEED reflection pattern. They correspond to the intersection of the Ewald (primary energy beam) sphere with the reciprocal lattice of the surface, which consists of rods perpendicular to the surface.
- [69] B. J. Hopkins, M. Leggett, and G. D. Watts, *Surf. Sci.* **28** (1971) 581
- [70] F. Dulot, P. Turban, B. Kierren, M. Alnot, and S. Andrieu, *Surf. Sci.* **473** (2001) 172
- [71] Z. Q. Wang, Y. S. Li, F. Jona, and P. M. Marcus, *Solid State Commun.* **61** (1987) 623
- [72] Y. Kamada, and M. Matsui, *J. Phys. Soc. Jpn* **66** (1997) 658
- [73] W.-S. Lo, T.-S. Chien, B.-S. Fang, C. M. Wei, and W. N. Mei, *Surf. Rev. Lett.* **5** (1998) 1035
- [74] Z.-L Han, S. Hardcastle, G. R. Harp, H. Li, X.-D. Wang, J. Zhang, and B. P. Tonner, *Surf. Sci.* **258** (1991) 313
- [75] G. C. Gazzadi, and S. Valeri, *Europhys. Lett.* **45** (1999) 501
- [76] J. X. Zheng-Johansson, O. Eriksson, and B. Johansson, *Phys. Rev. B* **59** (1999) 6131
- [77] L. A. Bruce and H. Jaeger, *Phil. Mag. A* **36** (1977) 1331
- [78] L. A. Bruce and H. Jaeger, *Phil. Mag. A* **37** (1978) 337
- [79] L. A. Bruce and H. Jaeger, *Phil. Mag. A* **40** (1979) 97
- [80] V. Y. Aristov, M. Bertolo, K. Jacobi, F. Maca and M. Scheffler, *Phys. Rev. B* **48** (1993) 5555

- [81] W. Wulfhekel, T. Gutjahr-Löser, F. Zavaliche, D. Sander, and J. Kirschner, *Phys. Rev. B* **64** (2001) 144422
- [82] S. Oikawa, T. Kanno, S. Iwata and S. Tsunashima, *J. Magn. Magn. Mat.* **14** (1996) 73
- [83] P. Bayle-Guillemaud, and J. Thibault, *Phil. Mag. A* **77** (1998) 475
- [84] J. Fassbender, Ch. Mathieu, B. Hillebrands, G. Güntherodt, R. Jungblut, and M. T. Johnson, *J. of Magn. Magn. Mat.* **148**, 156 (1995), and references therein.
- [85] P. M. Oppeneer, T. Kraft, and H. Eschrig, *J. of Magn. Magn. Mat.* **148**, 298 (1995), and references therein.
- [86] For example see: M. K. Debe, and D. A. King, *Phys. Rev. Lett.* **39** (1977) 708; *Surf. Sci.* **81** (1979) 193
- [87] E. Hüger, and E. Bauer, TU-Clausthal, unpublished
- [88] J. Ociepa and E. Bauer, TU-Clausthal, unpublished
- [89] Y. Liou, J. C. A. Huang, Y. D. Yao, C. H. Lee, K. T. Wu, C. L. Lu, S. Y. Liao, Y. Y. Chen, N. T. Liang, W. T. Yang, C. Y. Chen, and B. C. Hu, *J. Appl. Phys.* **76** (1994) 6516
- [90] W. Donner, N. Metoki, A. Abromeit and H. Zabel, *Phys. Rev. B* **48** (1993) 14745
- [91] N. Metoki, W. Donner, and H. Zabel, *Phys. Rev. B* **49** (1994) 17351
- [92] J. C. A. Huang, Y. Liou, H. L. Liu and Y. J. Wu, *J. Crystal Growth* **139** (1994) 363
- [93] A. Borghi, A. di Bona, D. Bisero, and S. Valeri, *Appl. Surf. Sci.* **150** (1999) 13
- [94] J. Zhang, Z.-L. Han, S. Varma, and B. P. Tonner, *Surf. Sci.* **298** (1993) 351
- [95] Y. Z. Wu, H. F. Ding, C. Jing, D. Wu, G. L. Liu, V. Gordon, G. S. Dong, X. F. Jin, S. Zhu, and K. Sun, *Phys. Rev. B* **57** (1998) 11935
- [96] E. Gu, M. Gester, R. J. Hicken, C. Daboo, M. Tselepi, S. J. Gray, J. A. C. Bland, L. M. Brown, T. Thomson, and P. C. Riedi, *Phys. Rev. B* **52** (1995) 14704
- [97] H. Wieldraaijer, J. T. Kohlhepp, P. LeClair, K. Ha, and W. J. M. de Jonge, *Phys. Rev. B* **67** (2003) 224430
- [98] S. K. Kim, C. Petersen, F. Jona and P. M. Marcus, *Phys. Rev. B* **54** (1996) 2184
- [99] C. P. Wang, S. C. Wu, F. Jona and P. M. Marcus, *Phys. Rev. B* **49** (1994) 17391
- [100] F. Jona, X. Z. Ji, and P. M. Marcus, *Phys. Rev. B* **68** (2003) 075421
- [101] J. P. Jay, E. Jêdryka, M. Wójcik, J. Dekoster, G. Langouche, and P. Panissod, *Z. Phys. B* **101** (1996) 329
- [102] J. Dekoster, E. Jêdryka, C. Mény, and G. Langouche, *Europhys. Lett.* **22** (1993) 433
- [103] H. Li, and B. P. Tonner, *Phys. Rev. B* **40** (1989) 10241
- [104] F. Xu, J. J. Joyce, M. W. Ruckman, H.-W. chen, F. Boscherini, D. M. Hill, S. A. Chambers, and J. H. Weaver, *Phys. Rev. B* **35** (1987) 2375

- [105] H. Giordano, A. Atrei, M. Torrini, U. Bardi, M. Gleeson, and C. Barnes, *Phys. Rev. B* **54** (1996) 11762
- [106] P. Wetzel, P. Bertoncini, D. Berling, A. Mehdaoui, B. Loegel, D. Belmont, G. Gewinner, C. Ulhaq-ouillet, and V. Pierron-Bohnes, *Surf. Sci.* **499** (2002) 210
- [107] A. M. Begley, S. K. Kim, F. Jona, and P. M. Marcus, *J. Phys. Condens Matter* **5** (1993) 7307
- [108] P. J. Berlowitz, and D. W. Goodman, *Surf. Sci.* **187** (1987) 463
- [109] M. Blaszcyszynova et al., *Surf. Sci.* **304** (1994) 325
- [110] B. Heinrich, A. S. Arrot, J. F. Cochran, C. Liu, and K. Myrtle, *J. Vac. Sci. Technol. A* **4** (1986) 1376
- [111] B. Heinrich, S. T. Purcell, J. R. Dutcher, K. B. Urquhart, J. F. Cochran, and A. S. Arrot, *Phys. Rev. B* **38** (1988) 12879
- [112] H. Wormeester, E. Hüger, and E. Bauer, *Surf. Sci.* **377-379** (1997) 988
- [113] T. Valla, P. Pervan, M. Milun, and K. Wandelt, *Surf. Sci.* **374** (1997) 51
- [114] M. Dietterle, T. Will, and D. M. Kolb, *Surf. Sci.* **396** (1998) 189
- [115] B. Heinrich, Z. Celinski, J. F. Cochran, W. B. Muir, J. Rudd, Q. M. Zhong, A. S. Arrot, K. Myrtle, and J. Kirschner, *Phys. Rev. Lett.* **64** (1990) 673
- [116] H. Li, D. Tian, J. Quinn, Y. S. Li, F. Jona, and P. M. Marcus, *Phys. Rev. B* **43** (1991) 6342
- [117] W. F. Egelhoff, Jr., I. Jacob, J. M. Rudd, J. F. Cochran, and B. Heinrich, *J. Vac. Sci. Technol. A* **8** (1990) 1582
- [118] D. T. Jiang, E. D. Crozier, and B. Heinrich, *Phys. Rev. B* **44** (1991) 6401
- [119] B. M. Ocko, J. K. Robinson, M. Weinert, R. J. Randler, and D. M. Kolb, *Phys. Rev. Lett.* **83** (1999) 780
- [120] R. J. Randler, D. M. Kolb, B. M. Ocko, and J. K. Robinson, *Surf. Sci.* **447** (2000) 187
- [121] Y. Kamada, and M. Matsui, *J. Phys. Soc. Jpn* **66** (1997) 466
- [122] Z. Q. Wang, S. H. Lu, Y. S. Li, F. Jona, and P. M. Marcus, *Phys. Rev. B* **35** (1987) 9322
- [123] H. Li, S. C. Wu, D. Tian, J. Quinn, Y. S. Li, F. Jona, and P. M. Marcus, *Phys. Rev. B* **40** (1989) 5841
- [124] M. A. Tomaz, D. C. Ingram, G. R. Harp, D. Lederman, E. Mayo, and W. L. O'Brien, *Phys. Rev. B* **56** (1997) 5474
- [125] T. Valla, and M. Milun, *Surf. Sci.* **315** (1994) 81
- [126] M. Milun, P. Pervan, B. Gumhalter, and D. P. Woodruff, *Phys. Rev. B* **59** (1999) 5170
- [127] R. W. Judd, M. A. Reichelt, E. G. Scott, and R. M. Lambert, *Surf. Sci.* **185** (1987) 529

- [128] The observation based on X-ray diffraction [72] that the structure of Ni films deposited on Fe(001) changes with increasing thickness from bct to (110)-oriented fcc can also readily be explained by a transition to a (11 $\bar{2}$ 0)-oriented hcp or dhcp phase because the fcc- d_{220} lattice spacing is equal to the hcp or dhcp $d_{11\bar{2}0}$ lattice spacing.
- [129] Y. Mishin, M. J. Mehl, D. A. Papaconstantopoulos, A. F. Voter, and J. D. Kress, *Phys. Rev. B* **63** (2001) 224106
- [130] M. J. Mehl, A. Aguayo, L. L. Boyer, and R. de Coss, *Phys. Rev. B* **70** (2004) 014105
- [131] L. G. Wang, M. Šob, and Zhenyu Zhang, *J. of Physics and Chemistry of Solids* **64** (2003) 863
- [132] V. Paidar, L. G. Wang, M. Šob, and V. Vitek, *Modelling Simul. Mater. Sci. Eng.* **7** (1999) 369
- [133] E. Hüger, T. Kana, K. Osuch, and M. Šob, in preparation.
- [134] R. M. Wentzcovitch, and H. Krakauer, *Phys. Rev. B* **42** (1990) 4563
- [135] M. Zeleny, E. Hüger, T. Kana, K. Osuch, and M. Šob, in preparation.
- [136] J. P. Hirth, and J. Lothe, *Theory of dislocations*, second edition, (Wiley, New-York, 1982, ISBN 0-471-09125-1)
- [137] Th. Duden, thesis, (TU-Clausthal, 1996); Th. Duden, R. Zdyb, M. S. Altman, and E. Bauer, *Surf. Sci.* **480** (2001) 145
- [138] L. Duo, R. Bertacco, G. Isella, F. Ciccacci, and M. Richter, *Phys. Rev. B* **61** (2000) 15294
- [139] R. Bertacco, G. Isella, L. Duo, F. Ciccacci, A. di Bona, P. Luches, and S. Valeri, *Surf. Sci.* **454-456** (2000) 671
- [140] S. Valeri, C. Giovanardi, A. Borghi, A. di Bona, and P. Luches, *Appl. Surf. Sci.* **175-176** (2001) 123
- [141] A. Borghi, A. di Bona, P. Luches, and S. Valeri, *Surf. Sci.* **466** (2000) 30
- [142] M. T. Kief, and W. F. Egelhoff, Jr., *Phys. Rev. B* **47** (1993) 10785, and references therein.
- [143] S. A. Chambers, S. B. Anderson, H.-W. Chen, and J. H. Weaver, *Phys. Rev. B* **35** (1987) 2592
- [144] A. M. Bittner, J. Wintterlin, and G. Ertl, *Surf. Sci.* **376** (1997) 267
- [145] W. F. Egelhoff, Jr., P. J. Chen, R. D. McMichael, C. J. Powell, R. D. Deslattes, F. G. Serpa, and R. D. Gomez, *J. Appl. Phys.* **89** (2001) 5208
- [146] P. H. Schmidt, J. M. Rowell, and W. L. Feldmann, *Appl. Phys. Lett* **39** (1981) 177
- [147] S. Ram, *Acta Materialia* **49** (2001) 2297
- [148] S. Ram, D. Gosh, S. K. Roy, *J. Material Science* **36** (2001) 3745
- [149] R. Banerjee, private communication.
- [150] S. A. Dregia, R. Banerjee, and H. L. Fraser, *Scripta Mater.* **29**, 217 (1998) 217
- [151] R. Banerjee, S. A. Dregia, and H. L. Fraser, *Acta Mater.* **47** (1999) 4225

-
- [152] G. B. Thompson, R. Banerjee, S. A. Dregia, and H. L. Fraser, *Acta Mater.* **51** (2003) 5285
- [153] G. B. Thompson, R. Banerjee, and H. L. Fraser, *Appl. Phys. Lett.* **83** (2003) 3471
- [154] G. B. Thompson, R. Banerjee, and H. L. Fraser, *Appl. Phys. Lett.* **84** (2004) 1082
- [155] C. Rath, J.E. Prieto, S. Muller, R. Miranda, and K. Heinz, *Phys. Rev. B* **55** (1997) 10791
- [156] P. Boher, F. Giron, P. Houdy, P. Beauvillain, C. Chappert, and P. Veillet, *J. Appl. Phys.* **70** (1991) 5507
- [157] B. Heinrich, J. F. Cochran, M. Kowalewski, J. Kirschner, Z. Chelinski, A. S. Arrot, and K. Myrtle, *Phys. Rev. B* **44**, 9348 (1991); B. Heinrich, Z. Chelinski, J. F. Cochran, A. S. Arrot, and K. Myrtle, *J. Appl. Phys.* **70** (1991) 5769

Acknowledgements

This thesis has been carried out at the Institute of Physics and Physical Technology of the Technical University Clausthal, and would not been possible without the generous support of this great laboratory.

The subject of this thesis has grown out of my diploma thesis that had been suggested and supervised by Professor E. Bauer.

I wish to express my sincere gratitude to Professor W. Daum and to Professor L. Fritsche for their unceasing encouragement and for supporting and supervising my work. In particular, I want to thank Prof. L. Fritsche for his kind willingness to share his knowledge, which has very much contributed to my understanding of surfaces and solids.

I would also like to sincerely thank Professor V. Kempter for co-assessing this thesis.

I am deeply indebted to Professor K. Osuch who have contributed significantly not only to my research effort but also helped me to better endure worries. I also thank him for his encouragement and persistence that were important for the enjoyment and success of my work.

I wish to thank Dr. H. Knoppe for introducing me into the experimental techniques. I thank Dr. H. Wormeester for his help in mounting the ion gun and repairing the electron gun.

I gratefully acknowledge the assistance of members of electronic and mechanical work shops, especially B. Wittenberg, without whose co-operation it would be not possible to change and to maintain some components of the experimental set-up.

For the friendly working atmosphere I want to thank all the present and former members of the Institute of Physics and Physical Technology.

My very special thanks are more numerous –than stars exist in the universe– to my wife, Daniela and son, Edwin, for their immense emotional support given to me. I dedicate my work to them.

Lebenslauf

Persönliche Daten

Geburtsdatum und -ort	01.04.1969 in Lugosch (Transylvanien, Rumänien)
Familienstand	verheiratet, 1 Sohn (16 Jahre alt)
Staatsangehörigkeit	deutsch

Schulbildung

15.09.1975 - 15.06.1983	Deutsche Abteilung der Grundschule Nr. 6 in Lugosch
15.07.1983 - 15.07.1987	Lyzeum (Gymnasium) 'Coriolan Brediceanu' in Lugosch
15.07.1987 - 20.04.1991	Studium der Physik an der West-Universität Timisoara
21.04.1991	Ausreise nach Deutschland
01.10.1991 - 17.04.1996	Studium der Physik an der Technischen Universität Clausthal in Clausthal-Zellerfeld
21.04.1996	Datum des Diplomzeugnisses

Berufstätigkeit

08.08.1996 -30.06.2002	Angestellter am Institut für Physik und Physikalischen Technologien der TU-Clausthal
30.06.2002 -14.02.2005	Arbeiten an der Auswertung und der Veröffentlichung eines grossen Teils der Ergebnisse die am Institut für Physik und Physikalischen Technologien der TU-Clausthal erzielt wurden. Die Liste der Publikationen ist diesem Lebenslauf beigelegt.
15.02.2005 -	Angestellter im Fachbereich Biowerkstoffe am Institut für Bioprocess- und Analysenmesstechnik e.V., Rosenhof 37308 Heilbad Heiligenstadt

Clausthal, im August 2005

Erwin Hüger

Liste der Publikationen

- *Born into nobility*
E. Hüger, and K. Osuch
Nature **436** (2005) 606; *Research Highlights*
- *Pd bonded to Nb(001): Dependence of noble metal and ferromagnetic characteristics on film thickness*
E. Hüger, and K. Osuch
Physical Review B **72** (2005) 085432
- *Pd bonded to Nb(001): Dependence of noble metal and ferromagnetic characteristics on film thickness*
E. Hüger, and K. Osuch
Selected for the August 29, 2005 issue of Virtual Journal of Nanoscale Science and Technology which is an edited compilation of articles covering a focused area of frontier research.
- *Making a noble metal of Pd*
E. Hüger, and K. Osuch
Europhysics Letters **71** (2005) 276
- *The growth of noble metals in (11 $\bar{2}$ 0)-oriented hexagonal close-packed nano-films by epitaxy on Nb(001)*
E. Hüger, and K. Osuch
Thin Solid Films **488** (2005) 291
- *Alloying of Pd thin films with Nb(001)*
E. Hüger, H. Wormeester, and K. Osuch
Journal of Electron Spectroscopy and Related Phenomena **148** (2005) 79
- *First principle studies of the dependence of magnetism on the crystal phase in 4d and 5d late transition metals*
E. Hüger, and K. Osuch
European Physical Journal B **44** (2005) 145
- *Subsurface miscibility of metal overlayers with V, Nb, and Ta surfaces*
E. Hüger, H. Wormeester, and K. Osuch
Surface Science **580** (2005) 173
- *Quantum well states of $d_{3z^2+r^2}$ and $d_{xz,yz}$ orbital character in Pd nanofilms*
E. Hüger, and K. Osuch
Solid State Communications **132** (2004) 97
- *Quantum well states and film structure*
E. Hüger, and K. Osuch
Journal of Electron Spectroscopy and Related Phenomena **141** (2004) 13
- *Ferromagnetism in body centred cubic Rh*
E. Hüger, and K. Osuch
Solid State Communications **131** (2004) 175

- *Quantum well states and k-space symmetry*
E. Hüger, and K. Osuch
European Physical Journal B **37** (2004) 149
- *Quantum well states in (11 $\bar{2}$ 0) oriented hcp Au films*
E. Hüger, and K. Osuch
Physical Review B **68** (2003) 205425
- *Quantum well states in (11 $\bar{2}$ 0) oriented hcp Au films*
E. Hüger, and K. Osuch
Selected for the December 8, 2003 issue of Virtual Journal of Nanoscale Science and Technology which is an edited compilation of articles covering a focused area of frontier research.
- *Ferromagnetism in hexagonal close packed Pd*
E. Hüger, and K. Osuch
Europhysics Letters **63** (2003) 90
- *Evidence for strong Auger electron diffraction in thin metallic films*
E. Hüger, and K. Osuch
Europhysics Letters **62** (2003) 278
- *Hexagonal metal modification and thin film ferromagnetism*
E. Hüger, H. Wormeester, and E. Bauer
Surface Science **438** (1999) 185
- *Importance of the surface electronic structure in heteroepitaxie*
H. Wormeester, E. Hüger, and E. Bauer
Physical Review Letters **81** (1998) 854
- *Au on W(001): change in structure and orientation*
H. Wormeester, E. Hüger, and E. Bauer
Physical Review B **57** (1998) 10120
- *Growth of hcp Cu on W(100)*
H. Wormeester, E. Hüger, and E. Bauer
Surface Science **377-379** (1997) 988
- *Growth and electronic structure of thin epitaxial Pd and Co films on W(100)*
H. Wormeester, E. Hüger, and E. Bauer
Physical Review B **54** (1996) 17108
- *Growth of hcp and bcc Cu and Pd films*
H. Wormeester, E. Hüger, and E. Bauer
Physical Review Letters **77** (1996) 1540